

AN ABSTRACT OF THE THESIS OF

Hassan Ahmad M. Albarqi for the degree of Doctor of Philosophy in Pharmaceutical Sciences presented on June 12, 2019

Title: Systemically Delivered Magnetic Hyperthermia for Cancer Treatment

Abstract approved:

Oleh Taratula

Despite advances in treatment, cancer remains among the leading causes of death in the world. Progress in the treatment of metastatic cancers was seen with chemotherapy and radiotherapy, however, the major drawbacks of conventional cancer therapies are limited efficacy and severe side effects. Magnetic fluid hyperthermia (MFH) is a new cancer treatment approach being investigated in preclinical research. It has the ability to localize heat specifically in the tumor upon exposing magnetic nanoparticles, such as iron oxide nanoparticles (IONPs), to alternating magnetic field - with limited toxicity in normal tissue. IONPs have been intensively explored in the application of magnetic hyperthermia due to their unique magnetic properties. The intratumorally injected IONPs can generate the required heat (41- 45 °C) to induce apoptosis. Intratumoral injection provides the required amount of IONPs to generate enough heat to kill cancer cells with low systemic toxicity. However, the intratumoral injection is invasive and limited to localized and relatively accessible solid tumors. In contrast, systemic injection is minimally

invasive and can deliver nanoparticles to poorly defined, non-localized cancer tumors of various shapes and sizes, including small metastatic tumor growth.

To overcome the current limitations of intravenous administration of IONPs and their heating ability, we have developed magnetic nanoclusters that can be delivered systemically and produce higher heating efficiency in comparison with conventional IONPs. Magnetic nanoclusters have shown an efficient cytotoxic effect in tumor cell lines and resulted in suppressing tumor growth in mouse models of ovarian and prostate cancer. They are safe and biocompatible without noticeable side effects in mice.

©Copyright by Hassan Ahmad M. Albarqi
June 12, 2019
All Rights Reserved

Systemically Delivered Magnetic Hyperthermia for Cancer Treatment

By

Hassan Ahmad M. Albarqi

A THESIS

submitted to

Oregon State University

in partial fulfillment of
the requirements for the
degree of

Doctor of Philosophy

Presented June 12, 2019
Commencement June 2020

Doctor of Philosophy thesis of Hassan Ahmad M. Albarqi presented on June 12, 2019

APPROVED:

Major Professor, representing Pharmaceutical Sciences

Dean of the College of Pharmacy

Dean of the Graduate School

I understand that my thesis will become part of the permanent collection of Oregon State University libraries. My signature below authorizes release of my thesis to any reader upon request.

Hassan Ahmad M. Albarqi, Author

ACKNOWLEDGMENTS

I would like to thank Dr. Oleh Taratula and his amazing wife Dr. Olena Taratula for their advice, guidance, encouragement, passing knowledge on to me, and all that they have done for me. I enjoyed working with you and I hope the project goes from strength to strength.

Many thanks to Drs. John Christensen, Adam Alani, Gaurav Sahay, and Ling Jin for serving on my thesis committee and their guidance.

Special Thanks to the lab mates, Leon H. Wong, Canan Schumann, Fahad Y. Sabei, Tetiana Korzun, Abraham S. Moses, Anna St Lorenz, and Adel Al Fatease for their everyday support.

My sincere gratitude goes first to ALLAH, then to my parents, my brothers and sisters, my wife and children, and all my friends in Saudi Arabia and the USA, for their love, support, and patience over the last five years.

CONTRIBUTION OF AUTHORS

Chapter 1

Written by Hassan Albarqi with editing and revision help by Dr. Oleh Taratula and Dr. Olena Taratula

Chapter 2

Dr. Oleh Taratula, Dr. Olena Taratula, and Hassan Albarqi designed the experiments that were conducted within this manuscript. Hassan Albarqi worked on most of the experiments with help from Leon H. Wong, Canan Schumann, Fahad Y. Sabei, Tetiana Korzun, Xiaoning Li, and Abraham S. Moses. Mikkel N. Hansen, and Pallavi Dhagat worked on the magnetic properties of the nanoparticle. Dr. Oleh Taratula and Dr. Olena gave valuable advice as well as editing expertise during the construction of this manuscript.

Chapter 3

Dr. Oleh Taratula, Dr. Olena Taratula, and Hassan Albarqi designed the experiments that were conducted within this manuscript. Hassan Albarqi worked on most of the experiments with help from Fahad Y. Sabei. Mikkel N. Hansen, and Pallavi Dhagat worked on the magnetic properties of the nanoparticle. Dr. Oleh Taratula and Dr. Olena gave valuable advice as well as editing expertise during the construction of this manuscript.

Chapter 4

Written by Hassan Albarqi with editing and revision help by Dr. Oleh Taratula and

Dr. Olena Taratula.

TABLE OF CONTENTS

	<u>Page</u>
CHAPTER 1	1
INTRODUCTION	1
1.1 HYPERTHERMIA.....	2
1.2 MAGNETIC FLUID HYPERTHERMIA	3
1.3 EFFECT OF MAGNETIC PROPERTIES ON SAR.....	5
1.3.1 Effect of Magnetic Field Parameters: Frequency and Field Strength (amplitude)	5
1.3.2 Effect of Carrier Viscosity.....	6
1.3.3 Effect of Nanoparticle Size.....	7
1.3.4 Effect of Nanoparticle Shape	8
1.3.5 Effect of Chemical Composition.....	9
1.4 CLINICAL APPLICATION OF MFH.....	11
1.5 REFERENCES	13
CHAPTER 2	20
BIOCOMPATIBLE NANOCLUSTERS WITH HIGH HEATING EFFICIENCY FOR SYSTEMICALLY DELIVERED MAGNETIC HYPERTHERMIA	20
2.1 ABSTRACT	21
2.2 INTRODUCTION:.....	23
2.3 MATERIALS AND METHODS	25
2.3.1 Materials	25
2.3.2 Methods	26
2.4 RESULTS AND DISCUSSION	38
2.4.1 Development and characterization of nanoclusters with enhanced heating efficiency	38
2.4.2 In vitro characterization of the developed nanoclusters	44
2.4.3 In vivo evaluation of the developed nanoclusters	47
2.5 CONCLUSIONS	54
2.6 ACKNOWLEDGMENTS.....	55
2.7 REFERENCES.....	57
CHAPTER 3	90
ZINC AND MANGANESE-DOPED IRON OXIDE NANOCLUSTERS FOR SYSTEMICALLY DELIVERED MAGNETIC HYPERTHERMIA	90
3.1 ABSTRACT	91
3.2 INTRODUCTION.....	92
3.3 MATERIALS AND METHODS	93
3.3.1 Materials	93
3.3.2 Methods	94
3.4 RESULTS AND DISCUSSION	99
3.4.1 In vitro characterization of ZnMn-IONCs.....	101
3.4.2 In vivo evaluation of ZnMn-IONCs	102

TABLE OF CONTENTS

	<u>Page</u>
3.5 CONCLUSION	103
3.6 ACKNOWLEDGMENTS.....	104
3.7 REFERENCES	105
CHAPTER 4.....	118
GENERAL CONCLUSIONS	118

LIST OF FIGURES

<u>Figure</u>	<u>Page</u>
Figure 2.1: Schematic illustration of the nanoclusters for magnetic hyperthermia.	67
Figure 2.2: Characterization of CoMn-IONP and IONP.	68
Figure 2.3: Characterization of CoMn-IONP and IONP nanoclusters.	69
Figure 2.4: Cell viability and heating profile of CoMn-IONP and IONP nanoclusters.	70
Figure 2.5: In vivo biodistribution of CoMn-IONPs.	71
Figure 2.6: Tumor histology.	72
Figure 2.7: Intratumoral heating profile and tumor volume.	73
Figure 2.8: In vivo toxicity evaluation of CoMn-IONPs.	75
Figure 2.9: EDX line scans for metal composition of CoMn-IONPs.	76
Figure 2.10: EDX elemental mappings of CoMn-IONP.	77
Figure 2.11: Characterization of spherical IONPs obtained from Ocean NanoTech.	78
Figure 2.1: Characterization of spherical IONPs prepared in the lab.	79
Figure 2.13: Heating profiles of magnetic nanoparticle and nanocluster in THF and 5% dextrose.	80
Figure 2.14: Characterization of single magnetic nanoparticles by TEM and DLS.	81
Figure 2.15: Viability of ES-2 ovarian cancer cells with various concentrations of CoMn-IONP nanoclusters.....	82
Figure 2.16: Viability of human embryonic kidney cells (HEK-293) incubated for 24 h with different concentrations of CoMn-IONP and IONP nanoclusters.	83
Figure 2.17: Viability of A2780/CDDP human ovarian carcinoma cells with various concentrations of CoMn-IONP and IONP nanoclusters.	84
Figure 2.18: The NIR fluorescence intensity of CoMn-IONPs in tumor for 24 h.	85
Figure 2.19: Intratumoral heating profile and tumor volume of IONPs prepared in our lab.	86
Figure 2.20: Mice rectal temperature profile.	87

LIST OF FIGURES

<u>Figure</u>	<u>Page</u>
Figure 2.21: Size distribution of CoMn-IONP nanoclusters and empty PEG-PCL nanoparticles tested by DLS.....	88
Figure 2.22. Detection of tetrahydrofuran by reversed-phase high-performance liquid chromatography (RP-HPLC):	89
Figure 3.1: Schematic illustration of the nanoclusters for magnetic hyperthermia.	110
Figure 3.2: Characterization of ZnMn-IONP and IONP.	111
Figure 3.3: Characterization of ZnMn-IONCs and IONCs.	112
Figure 3.4: Cell viability and internalization of nanocluster.	113
Figure 3.5: Heating profile and cell viability of ZnMn-IONCs and IONCs.....	114
Figure 3.6: In vivo biodistribution of ZnMn-IONCs.....	115
Figure 3.7: Intratumoral heating profile, tumor volume, and body weight.	117

DEDICATION

This thesis is dedicated to my dear parents, amazing wife, and precious sons

CHAPTER 1

INTRODUCTION

Hassan Ahmad M. Albarqi

1.1 HYPERTHERMIA

Cancer hyperthermia is a technique used to treat cancer tumors where tissue is exposed to a temperature higher than normal.¹ The elevation in temperature can damage or destroy cancer cells. It can be used alone or in combination with other conventional therapies including chemotherapy and radiotherapy.² Hyperthermia treatment is classified according to the degree of temperature increase into three categories: thermal ablation, moderate hyperthermia, and mild hyperthermia. Thermal ablation aims to subject a tumor to temperatures above 46 °C, which yield tissue necrosis, carbonization, or coagulation. Moderate hyperthermia will heat cancer cells between 41 and 45 °C. During moderate hyperthermia, cells experience heat stress resulting in moderate cellular inactivation that affects most regulatory proteins involved in cell growth and inhibition of many cellular functions. Mild hyperthermia uses temperatures lower than 41 °C and it makes the tumor cells more sensitive to the effects of chemotherapy.³

Hyperthermia is also distinguished into three main clinical methods: local, regional, and whole body hyperthermia, which depend on the extent of the region being treated. Local hyperthermia is used to apply heat only to a small area of interest like a tumor. Regional hyperthermia involves applying heat to a part of the body such as whole tissue and organ. Whole body hyperthermia is used to treat metastatic cancer by heating the entire body.^{3,4}

One of the main challenges of hyperthermia treatment is to heat the targeted tissues of the disease without damaging healthy ones. Based on the tumor location, local hyperthermia is a promising approach to deliver heat to the specified region of interest.

1.2 MAGNETIC FLUID HYPERTHERMIA

Magnetic fluid hyperthermia (MFH) is an approach that has been used to damage or destroy cancer cells by localized heat. MFH is based on selective heating of the magnetic nanoparticles (MNPs) accumulated in the cancer tissue upon exposure to non-invasive alternating magnetic field (AMF). The generated heat can be remotely controlled by adjusting the parameters of external AMF - frequency (f) and amplitude (H).⁵⁻⁷ Selective accumulation of nanoparticles in cancer cells relies mostly on passive diffusion through the enhanced permeability and retention effect (EPR). To further improve MFH's efficacy, selectivity, and safety, tumor-targeted ligands (antibodies, peptides, etc) can be conjugated to nanoparticles.^{8, 9} MFH was first proposed in 1957 for cancer treatment by Gilchrist *et al.*⁹ Since then, MFH has been subjected to many *in vitro* and *in vivo* investigations. Iron oxide nanoparticle (IONP) is a promising candidate for magnetic hyperthermia therapy due to its unique physical and chemical properties, such as size, surface charge, superparamagnetism, etc.¹⁰ Direct local injections of IONPs have been used to focus the generated heat at the targeted tissue, and one of the examples is a successful treatment of brain tumor using this approach.^{11, 12} Despite a number of encouraging results, current clinical applications of MFH are limited to the treatment of relatively accessible tumors because the targeted temperatures required to induce apoptosis/necrosis can be achieved only by direct intratumoral injection of IONPs.^{13, 14} A reproducible and significant tumor accumulation of MNPs after systemic delivery has yet to be achieved. Therefore, there is a critical need to develop an efficient biocompatible magnetic nanoparticle capable of (i) efficient accumulation in cancer tumors following systemic delivery at a clinically relevant dose, and (ii) generation of desirable intratumoral temperatures upon exposure to AMF (> 41 °C).

The heating efficiency of any MNPs is measured in terms of specific absorption rate (SAR). SAR of MNPs must be determined to compare the efficiency of different magnetic nanoparticles. The SAR of any magnetic material is defined as the power to generate heat due to the transformation of magnetic energy into heat when placed under AMF.¹⁵ The SAR is defined by the equation below:

$$\text{SAR} = (CV_s/m) \times (dT/dt),$$

where C is the specific heat capacity of the medium, V_s is the sample volume, m is the mass of magnetic nanoparticle suspended in the medium, and dT/dt is the rate of change of temperature.

For MFH, higher SAR at low dosage is the main feature that should be achieved in the synthesis of MNPs for cancer hyperthermia application. The heat generation of MNPs can be ascribed to two different mechanisms: relaxation loss, and hysteresis loss. Hysteresis loss occurs when an AMF is applied to the MNPs; the atomic domains within the MNPs are aligned in one particular direction accordingly with the AMF. When AMF is reversed in the opposite direction, there will be a consumption of electrical energy that is released in the form of heat.¹⁶ MNPs exhibit superparamagnetic properties, have no hysteresis losses, and generate heat due to relaxational losses. The relaxation losses are categorized into two types: Néel and Brownian relaxations. Néel relaxation mechanism occurs due to the rapid reorientation in the magnetic nanoparticle moments internally (internal dynamics). Brownian relaxation is due to the physical rotation of individual MNP within a medium around their own axes (external dynamics).¹⁷

In general, SAR values depend on the following parameters: MNPs structure, magnetic properties, amplitude (H), and frequency (f) of AMF.^{18, 19} Thus, to achieve effective hyperthermia after systemic delivery of MNPs, further research is necessary to investigate how

the magnetic nanoparticle properties of MNPs and the magnetic field parameters can be optimized for efficient MFH application in reliable cancer therapy.

1.3 EFFECT OF MAGNETIC PROPERTIES ON SAR

1.3.1 Effect of Magnetic Field Parameters: Frequency and Field Strength (amplitude)

SAR of the magnetic nanoparticle can be influenced by changing the properties of the applied alternating magnetic field: frequency (f) and field strength (H). The heating ability of superparamagnetic iron oxide nanoparticle can be tuned by adjusting these parameters. Matching the total relaxation time with the frequency and the strength of the magnetic field can maximize the SAR. Generally, higher frequency and field strength can be used to increase the SAR value.²⁰⁻²² However, in accordance with the application of the Rosensweig equation, the applied AMF to the targeted area of the body and the amplification of frequency (f) and field strength (H) must not exceed $5 \times 10^9 \text{ A m}^{-1} \text{ s}^{-1}$ to minimize non-selective heating of AMF in healthy tissue due to the generation of eddy currents during magnetic hyperthermia therapy.²³ Consequently, the heat generated by eddy currents should be considered for optimization of the SAR of MNP. Therefore, the prediction of optimized AMF parameters has been investigated in several studies to maximize SAR value. Engelmann *et al.* reported the effects of different frequencies (176, 373, 744, and 992 kHz) and field strengths (6, 9, 12, 15, and 18 mT/ μ_0) on the SAR of nanoparticles. Different particle sizes (from 21.9 nm to 27.7 nm) have been investigated to determine the preferred AMF parameters for hyperthermia.²⁴ The SAR values generally increased by increasing both frequencies and field strength, with the highest SAR values achieved when $f = 992 \text{ kHz}$ and $H = 18 \text{ mT}/\mu_0$, respectively. They also observed that increasing the size of the particle and the frequency will increase the SAR, but this is not the case with

increasing amplitudes. At highest amplitude (18 mT/ μ_0), a particle size of 25.3 nm has better SAR value than 27.7 nm. In a separate study, Shah *et al.* compared the heating efficiency of iron oxide nanoparticles (8-18 nm) at different magnetic field parameters ($f = 123$ to 430 kHz, $H = 15.1$ to 47.7 kA/m).²⁰ The result was in agreement with the Engelmann group; the larger MNPs display higher SAR value, and it increased with higher frequency and amplitude.

However, it is challenging to select the optimal parameters for the applied magnetic field because of the effects of magnetic nanoparticles properties such as structure, magnetic properties, and viscosity of NP's surroundings.

1.3.2 Effect of Carrier Viscosity

The heating rate of MNPs is dependent on carrier viscosity (solvent or physiological solution). The SAR decreases with increasing of the carrier viscosity due to lower Brownian relaxation time.²⁵ In a recent publication, SAR of highly anisotropic cobalt ferrite magnetic nanoparticles in different viscosity of carrier media (hexane, toluene, chloroform, water, and cell culture medium), was investigated.²⁶ It was observed that SAR of CoFe_2O_4 decreased with an increase in carrier viscosity at $H = 24$ kA/m and $f = 571$ kHz. This is clearly revealing that the physical rotation of MNPs is hindered by carrier viscosity. A separate report further confirmed that the SAR values increased as the carrier viscosity decreased.²⁷ These results give some insight about the particle movement once they are accumulated in the targeted tissue and demonstrate that the MNPs rely on Néel relaxation rather than Brownian relaxation since the tissue viscosity is high.

1.3.3 Effect of Nanoparticle Size

The heating capability of MNPs depends on their sizes, which are controlled by magnetic energy dissipation.¹⁸ The types of MNPs used for MFH are superparamagnetic and ferromagnetic particles that have sizes from 2 to 100 nm and, thus, allow easy penetration into several cancer tumors. The optimal particle size for MFH that can demonstrate the phenomenon of superparamagnetic property is 5-20 nm. Superparamagnetic nanoparticle (SMNP) was demonstrated as a potential MFH agent either *in vitro* or *in vivo* due to their unique magnetic properties and colloidal stability to avoid aggregation. SMNP is the state when particles reach up to their saturation magnetization in the presence of AMF, and the lack of remnant magnetization upon removal of AMF. However, it has been reported that the magnetization decreases when the particle size is smaller than 5 nm due to the increase of disorder spin on the surface of MNPs.²⁸⁻³⁰ Khandhar *et al.* compared the effect of different size (13, 14, 15, 16, and 18 nm) of superparamagnetic Fe₃O₄ at AMF conditions ($f = 373$ kHz, $H = 14$ kA/m).³¹ They found that the SAR reaches its maximum value when the particle size is around 16 nm and observed a decrease in SAR value above this size. In contrast, Lima *et al.* have measured SAR value for magnetite MNP (size range of 6 - 23 nm) in AMF with $f = 100$ kHz and $H = 13$ kA/m.³² They reported an increase of SAR values up to a size of ~18 nm, followed by a decrease in SAR value for a particle size of 23 nm. Another study has been done by Engelmann *et al.*, they measured the SAR value of iron oxide nanoparticles with size ranging from 21.9 nm to 27.7 nm at different AMF conditions.²⁴ When the magnetic field strength increases to $H = 18$ mT/ μ_0 , the highest SAR value was recorded at 25.4 nm. Moreover, they realized that increasing size distribution of MNPs could influence the heating properties and decrease SAR five-fold. Therefore, optimization of

particle size distribution provides improved magnetic properties required for enhancing the SAR value and should eventually reduce the MNP dose required for MFH and improve patient safety.

1.3.4 Effect of Nanoparticle Shape

The shape of nanoparticle has been shown to play a significant role in the heating performance of MNPs as well - by tuning the saturation magnetization and magnetic anisotropy.³³ Different shapes of MNPs have been studied in attempts to enhance their SAR. Based on the literature, non-spherical MNPs such as cube, hexagon, and octagon have shown better heating efficiency compared to spherical MNPs.^{34, 35} The reason for this is that non-spherical MNPs have lower surface anisotropy compared to spherical MNPs due to the reduction of disordered spins on their surface. Nemati *et al.* studied the effect of octagonal shape on the heating performance of iron oxide nanoparticle.³⁶ At the same concentration of iron and approximately the same particle size, the SAR for nanoparticles with octagonal shapes become larger than spherical nanoparticles, and the difference in SAR reached its maximum (more than 50%) when they applied the highest magnetic strength (800 Oe). Another study by Martinez-Boubeta *et al.* compared 20 nm iron oxide nanocube with spherical nanoparticles of similar volume and demonstrated 20 % superior SAR of iron oxide nanocubes.³⁷ Bauer *et al.* synthesized cubical magnetite and compared the SAR with spherical magnetite at a fixed frequency of 380 kHz and an amplitude of 16 k/m.³⁸ The authors observed the cubical magnetite exhibited a 5-fold higher SAR value compared to the spherical magnetite, where the particle size of the cube is smaller than that of the sphere (15.5 nm and 19.2 nm, respectively). Guardia *et al.* measured the SAR of cube-shaped water-soluble iron oxide nanocrystals at different particle size (12, 19, 25, and 38 nm).³⁹ The highest SAR of 2452 W/g_{Fe} recorded for 19 nm particle size at magnetic field parameters of 520 kHz and 29

kA/m. This is a clear indication that by tuning the shape of nanoparticles an improvement in the SAR of MNPs can be achieved.

1.3.5 Effect of Chemical Composition

Various MNPs with different magnetic properties and morphological metallic structures have been applied for MFH. MNPs has been ranging from iron oxide-based nanoparticle to metallic nanoparticle such as Mn, Fe, Co, Ni, Zn to achieve higher SAR that is desirable for MFH. Iron oxide-based nanoparticles such as maghemite NPs ($\gamma\text{-Fe}_2\text{O}_3$) and magnetite NPs (Fe_3O_4) have been investigated in biomedical applications due to their biocompatibility and biodegradability. Magnetite NPs have higher potential as MFH agents compared to maghemite due to its higher values of magnetization saturation and magnetic anisotropy. These nanoparticles can demonstrate the phenomenon of superparamagnetic property.⁴⁰⁻⁴²

Iron oxide based nanoparticles can also exist in different chemical compositions of their ferrites (MFe_2O_4 , where M = Ni, Co, Mn, Zn, and Mg). These ferrites have the ability to tune the magnetic properties of the nanoparticle based on the concentration ratio of the composition. These ferrites can be classified into three groups based on their crystal structure: spinel, garnet, and hexagonal ferrite. The spinel ferrite is the most prominent ferrite used in biomedical applications due to its biocompatibility. Spinel ferrite structure consists of oxygen anions crystallized in a cubical close-packed structure, cations in octahedral sites, and cations in tetrahedral sites. There are two basic cation distributions in spinel ferrites: normal distribution and inverse distribution. In normal spinel ferrites, tetrahedral sites are occupied by divalent cations, and octahedral sites are occupied by trivalent cations.⁴³⁻⁴⁵ For example, Zinc ferrite (ZnFe_2O_4) has a normal spinel structure. Where Zn^{2+} ions occupy the tetrahedral site, while the

octahedral sites are occupied by Fe^{3+} ions. If the tetrahedral sites are completely occupied by trivalent cations and the octahedral sites are occupied by both di- and tri-valent cations, the structure is defined as inverse spinel. The physical properties and magnetic behavior of spinel ferrite depend on cation distribution. The orientation of the magnetic moments of the cations increases when they are aligned parallel to the magnetic field in the octahedral sites. On the other hand, the orientation of cation magnetic moment decreases in the case of tetrahedral sites because they are antiparallel. Thus, the net charge of the magnetic moment depends on the cation nature in the spinel crystal structure.

Dönmez and colleagues compared the heating efficiency of MnFe_2O_4 , CoFe_2O_4 , and NiFe_2O_4 MNPs 20 nm in size and demonstrated that CoFe_2O_4 showed the highest SAR of ~ 315 W/g compared to other ferrites (~ 295 W/g for MnFe_2O_4 and NiFe_2O_4).⁴⁶ Another study reported the composition effect of single and multi-components MNPs on the SAR. The SAR of Fe_3O_4 nanoparticles with 15 nm is 333 W/g, while for 15 nm MnFe_2O_4 is 411 W/g, and for 9 nm CoFe_2O_4 was found to be 443 W/g. They also studied the effect of core-shell nanoparticle on the SAR. They made nanoparticles with different compositions and found that the SAR values of the core-shell MNPs are higher than that of single component MNPs (2280 W/g for $\text{CoFe}_2\text{O}_4@ \text{MnFe}_2\text{O}_4$; 3034 W/g for $\text{MnFe}_2\text{O}_4@ \text{CoFe}_2\text{O}_4$). The higher SAR of core-shell is attributed to the effect of interfacial interaction between core and shell phases of MNPs.⁴⁷ Another type of MNPs is metallic NPs such as Fe-Co, Fe-Pt, etc. These types of MNPs have excellent heating performance and demonstrate the ability to control their size, shape, and composition compared to other MNPs. However, they are not favorable in hyperthermia application due to their potential toxicity, chemical instability, and easy oxidation.⁴⁸ However, coating their toxic core with a biocompatible shell can reduce their toxicity.

1.4 CLINICAL APPLICATION OF MFH

In the past two decades, the number of investigations has increased in various aspects of MNPs to translate them into clinical application for hyperthermia. There are still unmet challenges to develop MNPs that can be efficient as MFH agents with high SAR, biocompatibility, chemical and colloidal stability, and the ability to accumulate in tumors via a non-invasive route of administration.¹² The clinical application of MFH is still limited to direct intratumoral injection of MNPs to provide the temperature required to damage or kill cancer cells. NanoTherm® is a therapy that has been approved in the European Union for the treatment of brain tumors. It was developed by MagForce Nanotechnologies AG. In NanoTherm® therapy, iron oxide nanoparticle injected slowly into the brain tumor, and patients treated twice a week for 4 to 10 sessions.¹¹ The treatment has some benefits, such as limiting systemic toxicity and delivering a sufficient amount of MNPs into the tumor to achieve the required heat to kill cancer cells. Despite the benefits of direct intratumoral injection of MNPs, it is still invasive, impractical for metastatic disease, and leaves some regions untreated due to tumor incongruence. To overcome these problems, intravenous administration is minimally invasive and more effectively loads tumors as well as metastases. Preclinical applications of conventional iron oxide nanoparticles (IONP) for cancer treatment are limited by the fact that their heating efficiency is relatively low and as a result, the amount of nanoparticles delivered systemically to the tumor tissue is not sufficient to reach a required intratumoral temperature increase for effective cancer hyperthermia. The intratumoral temperatures desired to inhibit or ablate the tumor would require high doses of iron oxide nanoparticle that are toxic. As an example, Huang *et al.* have successfully ablated tumor following intravenous injection of iron oxide nanoparticles at a dose

of 1700 mg_{Fe}/kg.¹³ However, the dose is extremely high compared to the recommended dose for the FDA-approved iron oxide nanoparticle Feraheme, which is 510 mg for a 60 kg adult.⁴⁹

In this work, we have successfully developed magnetic nanoclusters that possess a high specific absorption rate suitable for systemically delivered magnetic hyperthermia. The magnetic nanoclusters efficiently accumulate in cancer tumors following a single intravenous injection at a low dosage, elevating the intratumoral temperature to 42-44 °C upon exposure to AMF, and thus significantly inhibiting tumor growth.

1.5 REFERENCES

1. Cihoric, N.; Tsikkinis, A.; van Rhoon, G.; Crezee, H.; Aebbersold, D. M.; Bodis, S.; Beck, M.; Nadobny, J.; Budach, V.; Wust, P., Hyperthermia-related clinical trials on cancer treatment within the ClinicalTrials.gov registry. *International journal of hyperthermia* **2015**, *31* (6), 609-614.
2. Datta, N.; Ordóñez, S. G.; Gaip, U.; Paulides, M.; Crezee, H.; Gellermann, J.; Marder, D.; Puric, E.; Bodis, S., Local hyperthermia combined with radiotherapy and/or chemotherapy: Recent advances and promises for the future. *Cancer treatment reviews* **2015**, *41* (9), 742-753.
3. Kumar, C. S.; Mohammad, F., Magnetic nanomaterials for hyperthermia-based therapy and controlled drug delivery. *Advanced drug delivery reviews* **2011**, *63* (9), 789-808.
4. Behrouzkhia, Z.; Joveini, Z.; Keshavarzi, B.; Eyvazzadeh, N.; Aghdam, R. Z., Hyperthermia: how can it be used? *Oman medical journal* **2016**, *31* (2), 89.
5. Chang, D.; Lim, M.; Goos, J. A.; Qiao, R.; Ng, Y. Y.; Mansfeld, F. M.; Jackson, M.; Davis, T. P.; Kavallaris, M., Biologically Targeted Magnetic Hyperthermia: Potential and Limitations. *Frontiers in pharmacology* **2018**, *9*.
6. Albarqi, H. A.; Wong, L. H.; Schumann, C.; Sabei, F. Y.; Korzun, T.; Li, X.; Hansen, M. N.; Dhagat, P.; Moses, A. S.; Taratula, O., Biocompatible Nanoclusters with High Heating Efficiency for Systemically Delivered Magnetic Hyperthermia. *ACS nano* **2019**.
7. Deatsch, A. E.; Evans, B. A., Heating efficiency in magnetic nanoparticle hyperthermia. *Journal of Magnetism and Magnetic Materials* **2014**, *354*, 163-172.

8. Maeda, H.; Nakamura, H.; Fang, J., The EPR effect for macromolecular drug delivery to solid tumors: Improvement of tumor uptake, lowering of systemic toxicity, and distinct tumor imaging in vivo. *Advanced drug delivery reviews* **2013**, 65 (1), 71-79.
9. Zhang, H.; Li, J.; Hu, Y.; Shen, M.; Shi, X.; Zhang, G., Folic acid-targeted iron oxide nanoparticles as contrast agents for magnetic resonance imaging of human ovarian cancer. *Journal of ovarian research* **2016**, 9 (1), 19.
10. Hilger, I.; Kaiser, W. A., Iron oxide-based nanostructures for MRI and magnetic hyperthermia. *Nanomedicine : nanotechnology, biology, and medicine* **2012**, 7 (9), 1443-1459.
11. Maier-Hauff, K.; Rothe, R.; Scholz, R.; Gneveckow, U.; Wust, P.; Thiesen, B.; Feussner, A.; von Deimling, A.; Waldoefner, N.; Felix, R., Intracranial thermotherapy using magnetic nanoparticles combined with external beam radiotherapy: results of a feasibility study on patients with glioblastoma multiforme. *Journal of neuro-oncology* **2007**, 81 (1), 53-60.
12. Wust, P.; Gneveckow, U.; Wust, P.; Gneveckow, U.; Johannsen, M.; Böhmer, D.; Henkel, T.; Kahmann, F.; Sehouli, J.; Felix, R., Magnetic nanoparticles for interstitial thermotherapy—feasibility, tolerance and achieved temperatures. *International Journal of Hyperthermia* **2006**, 22 (8), 673-685.
13. Huang, H. S.; Hainfeld, J. F., Intravenous magnetic nanoparticle cancer hyperthermia. *International journal of nanomedicine* **2013**, 8, 2521-32.
14. Hilger, I., In vivo applications of magnetic nanoparticle hyperthermia. *International Journal of Hyperthermia* **2013**, 29 (8), 828-834.
15. Obaidat, I.; Issa, B.; Haik, Y., Magnetic properties of magnetic nanoparticles for efficient hyperthermia. *Nanomaterials* **2015**, 5 (1), 63-89.

16. Hedayatnasab, Z.; Abnisa, F.; Daud, W. M. A. W., Review on magnetic nanoparticles for magnetic nanofluid hyperthermia application. *Materials & Design* **2017**, *123*, 174-196.
17. Jeyadevan, B., Present status and prospects of magnetite nanoparticles-based hyperthermia. *Journal of the Ceramic Society of Japan* **2010**, *118* (1378), 391-401.
18. Fortin, J.-P.; Wilhelm, C.; Servais, J.; Ménager, C.; Bacri, J.-C.; Gazeau, F., Size-sorted anionic iron oxide nanomagnets as colloidal mediators for magnetic hyperthermia. *Journal of the American Chemical Society* **2007**, *129* (9), 2628-2635.
19. Pankhurst, Q. A.; Connolly, J.; Jones, S.; Dobson, J., Applications of magnetic nanoparticles in biomedicine. *Journal of physics D: Applied physics* **2003**, *36* (13), R167.
20. Shah, R. R.; Davis, T. P.; Glover, A. L.; Nikles, D. E.; Brazel, C. S., Impact of magnetic field parameters and iron oxide nanoparticle properties on heat generation for use in magnetic hyperthermia. *Journal of magnetism and magnetic materials* **2015**, *387*, 96-106.
21. Glöckl, G.; Hergt, R.; Zeisberger, M.; Dutz, S.; Nagel, S.; Weitschies, W., The effect of field parameters, nanoparticle properties and immobilization on the specific heating power in magnetic particle hyperthermia. *Journal of Physics: Condensed Matter* **2006**, *18* (38), S2935.
22. Hedayatnasab, Z.; Abnisa, F.; Daud, W. W. In *Investigation properties of superparamagnetic nanoparticles and magnetic field-dependent hyperthermia therapy*, IOP Conference Series: Materials Science and Engineering, IOP Publishing: 2018; p 012042.
23. Hergt, R.; Dutz, S., Magnetic particle hyperthermia—biophysical limitations of a visionary tumour therapy. *Journal of Magnetism and Magnetic Materials* **2007**, *311* (1), 187-192.

24. Engelmann, U. M.; Shasha, C.; Teeman, E.; Slabu, I.; Krishnan, K. M., Predicting size-dependent heating efficiency of magnetic nanoparticles from experiment and stochastic Néel-Brown Langevin simulation. *Journal of Magnetism and Magnetic Materials* **2019**, *471*, 450-456.
25. Savitha, S.; Bhattacharya, S. In *Synthesis and Characterization of Magnetic Colloids*, Macromolecular Symposia, Wiley Online Library: 2017; p 1600195.
26. Torres, T. E.; Lima, E.; Calatayud, M. P.; Sanz, B.; Ibarra, A.; Fernández-Pacheco, R.; Mayoral, A.; Marquina, C.; Ibarra, M. R.; Goya, G. F., The relevance of Brownian relaxation as power absorption mechanism in Magnetic Hyperthermia. *Scientific reports* **2019**, *9* (1), 3992.
27. Darwish, M. S., Effect of carriers on heating efficiency of oleic acid-stabilized magnetite nanoparticles. *Journal of Molecular Liquids* **2017**, *231*, 80-85.
28. Mehdaoui, B.; Meffre, A.; Carrey, J.; Lachaize, S.; Lacroix, L. M.; Gougeon, M.; Chaudret, B.; Respaud, M., Optimal size of nanoparticles for magnetic hyperthermia: a combined theoretical and experimental study. *Advanced Functional Materials* **2011**, *21* (23), 4573-4581.
29. Lévy, M.; Wilhelm, C.; Siaugue, J.-M.; Horner, O.; Bacri, J.-C.; Gazeau, F., Magnetically induced hyperthermia: size-dependent heating power of γ -Fe₂O₃ nanoparticles. *Journal of Physics: Condensed Matter* **2008**, *20* (20), 204133.
30. Tong, S.; Quinto, C. A.; Zhang, L.; Mohindra, P.; Bao, G., Size-dependent heating of magnetic iron oxide nanoparticles. *ACS nano* **2017**, *11* (7), 6808-6816.
31. Khandhar, A. P.; Ferguson, R. M.; Simon, J. A.; Krishnan, K. M., Tailored magnetic nanoparticles for optimizing magnetic fluid hyperthermia. *Journal of Biomedical Materials Research Part A* **2012**, *100* (3), 728-737.

32. Lima Jr, E.; De Biasi, E.; Mansilla, M. V.; Saleta, M. E.; Granada, M.; Troiani, H. E.; Effenberger, F.; Rossi, L.; Rechenberg, H.; Zysler, R. D., Heat generation in agglomerated ferrite nanoparticles in an alternating magnetic field. *Journal of Physics D: Applied Physics* **2012**, *46* (4), 045002.
33. Guardia, P.; Labarta, A.; Batlle, X., Tuning the size, the shape, and the magnetic properties of iron oxide nanoparticles. *The Journal of Physical Chemistry C* **2010**, *115* (2), 390-396.
34. Guardia, P.; Di Corato, R.; Lartigue, L.; Wilhelm, C.; Espinosa, A.; Garcia-Hernandez, M.; Gazeau, F.; Manna, L.; Pellegrino, T., Water-soluble iron oxide nanocubes with high values of specific absorption rate for cancer cell hyperthermia treatment. *ACS nano* **2012**, *6* (4), 3080-3091.
35. Wang, H.; Shrestha, T. B.; Basel, M. T.; Pyle, M.; Toledo, Y.; Konecny, A.; Thapa, P.; Ikenberry, M.; Hohn, K. L.; Chikan, V., Hexagonal magnetite nanoprisms: preparation, characterization and cellular uptake. *Journal of Materials Chemistry B* **2015**, *3* (23), 4647-4653.
36. Nemati, Z.; Alonso, J.; Martinez, L.; Khurshid, H.; Garaio, E.; Garcia, J.; Phan, M.; Srikanth, H., Enhanced magnetic hyperthermia in iron oxide nano-octopods: size and anisotropy effects. *The Journal of Physical Chemistry C* **2016**, *120* (15), 8370-8379.
37. Martinez-Boubeta, C.; Simeonidis, K.; Makridis, A.; Angelakeris, M.; Iglesias, O.; Guardia, P.; Cabot, A.; Yedra, L.; Estradé, S.; Peiró, F., Learning from nature to improve the heat generation of iron-oxide nanoparticles for magnetic hyperthermia applications. *arXiv preprint arXiv:1304.1298* **2013**.

38. Bauer, L. M.; Situ, S. F.; Griswold, M. A.; Samia, A. C. S., High-performance iron oxide nanoparticles for magnetic particle imaging-guided hyperthermia (hMPI). *Nanoscale* **2016**, 8 (24), 12162-12169.
39. Guardia, P.; Di Corato, R.; Lartigue, L.; Wilhelm, C.; Espinosa, A.; Garcia-Hernandez, M.; Gazeau, F.; Manna, L.; Pellegrino, T., Water-soluble iron oxide nanocubes with high values of specific absorption rate for cancer cell hyperthermia treatment. *ACS Nano* **2012**, 6 (4), 3080-91.
40. Sharifi, I.; Shokrollahi, H.; Amiri, S., Ferrite-based magnetic nanofluids used in hyperthermia applications. *Journal of magnetism and magnetic materials* **2012**, 324 (6), 903-915.
41. Ghosh Chaudhuri, R.; Paria, S., Core/shell nanoparticles: classes, properties, synthesis mechanisms, characterization, and applications. *Chemical reviews* **2011**, 112 (4), 2373-2433.
42. Ferrando, R.; Jellinek, J.; Johnston, R. L., Nanoalloys: from theory to applications of alloy clusters and nanoparticles. *Chemical reviews* **2008**, 108 (3), 845-910.
43. Kolhatkar, A.; Jamison, A.; Litvinov, D.; Willson, R.; Lee, T., Tuning the magnetic properties of nanoparticles. *International journal of molecular sciences* **2013**, 14 (8), 15977-16009.
44. Ding, L.; Xue, L.; Li, Z.; Li, S.; Tang, G.; Qi, W.; Wu, L.; Ge, X., Study of cation distributions in spinel ferrites $M_x Mn_{1-x} Fe_2O_4$ ($M = Zn, Mg, Al$). *AIP Advances* **2016**, 6 (10), 105012.
45. Mathew, D. S.; Juang, R.-S., An overview of the structure and magnetism of spinel ferrite nanoparticles and their synthesis in microemulsions. *Chemical engineering journal* **2007**, 129 (1-3), 51-65.

46. Dönmez, C. E. D.; Çiğdem, E.; Manna, P. K., Comparative Heating Efficiency of Cobalt-, Manganese-, and Nickel-Ferrite Nanoparticles for a Hyperthermia Agent in Biomedicines. *ACS APPLIED MATERIALS & INTERFACES* **2019**, *11* (7), 6858-6866.
47. Lee, J.-H.; Jang, J.-t.; Choi, J.-s.; Moon, S. H.; Noh, S.-h.; Kim, J.-w.; Kim, J.-G.; Kim, I.-S.; Park, K. I.; Cheon, J., Exchange-coupled magnetic nanoparticles for efficient heat induction. *Nature nanotechnology* **2011**, *6* (7), 418-422.
48. Matoussevitch, N.; Gorschinski, A.; Habicht, W.; Bolle, J.; Dinjus, E.; Bönnemann, H.; Behrens, S., Surface modification of metallic Co nanoparticles. *Journal of Magnetism and Magnetic Materials* **2007**, *311* (1), 92-96.
49. Nguyen, K. L.; Yoshida, T.; Han, F.; Ayad, I.; Reemtsen, B. L.; Salusky, I. B.; Satou, G. M.; Hu, P.; Finn, J. P., MRI with ferumoxytol: a single center experience of safety across the age spectrum. *Journal of Magnetic Resonance Imaging* **2017**, *45* (3), 804-812.

CHAPTER 2

Biocompatible Nanoclusters with High Heating Efficiency for Systemically Delivered Magnetic Hyperthermia

Hassan A. Albarqi, Leon H. Wong, Canan Schumann, Fahad Y. Sabei, Tetiana
Korzun, Xiaoning Li, Mikkel N. Hansen, Pallavi Dhagat, Abraham S. Moses,
Olena Taratula and Oleh Taratula

Journal: *ACS Nano* 2019, *ASAP*

Publication Date: May 13, 2019

DOI: 10.1021/acsnano.8b06542

Copyright © 2019 American Chemical Society

2.1 ABSTRACT

Despite its promising therapeutic potential, nanoparticle-mediated magnetic hyperthermia is currently limited to treatment of localized and relatively accessible cancer tumors because the required therapeutic temperatures above 40 °C can only be achieved by direct intratumoral injection of conventional iron oxide nanoparticles. To realize the true potential of magnetic hyperthermia for cancer treatment, there is an unmet need for nanoparticles with high heating capacity that can efficiently accumulate at tumor sites following systemic administration and generate desirable intratumoral temperatures upon exposure to an alternating magnetic field (AMF). Although there have been many attempts to develop the desired nanoparticles, reported animal studies reveal the challenges associated with reaching therapeutically relevant intratumoral temperatures following systemic administration at clinically relevant doses. Therefore, we developed efficient magnetic nanoclusters with enhanced heating efficiency for systemically delivered magnetic hyperthermia that are composed of cobalt- and manganese-doped, hexagon-shaped iron oxide nanoparticles (CoMn-IONP) encapsulated in biocompatible PEG-PCL (poly(ethylene glycol)-*b*-poly(ϵ -caprolactone))-based nanocarriers. Animal studies validated that the developed nanoclusters are non-toxic, efficiently accumulate in ovarian cancer tumors following a single intravenous injection, and elevate intratumoral temperature up to 44 °C upon exposure to safe and tolerable AMF. Moreover, the obtained results confirmed the efficiency of the nanoclusters to generate the required intratumoral temperature after repeated injections and demonstrated that nanoclusters-mediated magnetic hyperthermia significantly inhibits cancer growth. In summary, this nanoplatform is a milestone in the development of systemically delivered magnetic hyperthermia for treatment of cancer tumors that are difficult to access for intratumoral injection.

Keywords: magnetic hyperthermia, magnetic nanoparticles, nanoclusters, systemic delivery

2.2 INTRODUCTION:

Magnetic hyperthermia is a highly promising therapeutic modality for treatment of various cancers.^{1, 2} It is based on the concept that magnetic nanoparticles delivered to tumors can generate heat after exposure to a non-invasive external alternating magnetic field (AMF) and consequently induce cell death.^{2, 3} In general, cancer cells heated to temperatures between 42 and 46 °C for 30 min or longer undergo apoptosis, whereas temperatures above 46 °C (thermoablation) result in cancer cell necrosis.^{3, 4} In contrast to thermoablation, hyperthermia-induced apoptosis is a preferable strategy for tumor eradication without causing severe side effects to healthy tissues. It has also been validated that magnetic hyperthermia at moderate temperatures increases the susceptibility of cancer cells to chemotherapy, radiation and immunotherapy.^{1, 2, 5-8}

Clinical trials confirmed that external AMF can remotely generate therapeutic temperatures (≥ 42 °C) in deep-lying cancer tumors (*e.g.*, prostate cancer) containing iron oxide nanoparticles, without causing severe side effects to healthy tissue.⁹⁻¹¹ Despite this success, magnetic hyperthermia is currently limited to treatment of localized and relatively accessible tumors because the required therapeutic temperatures (≥ 42 °C) can only be achieved by direct intratumoral injection of conventional iron oxide nanoparticles.^{12, 13} Intratumoral delivery of magnetic nanoparticles, however, is challenging for non-localized tumors with regional metastases. It is also invasive and success is dependent on the skill and experience of the operator. For example, the delivery of iron oxide nanoparticles to cancer tumors was performed intraoperatively in patients with cervical carcinoma.¹¹ In contrast, intravenous administration is minimally invasive and can potentially deliver magnetic nanoparticles to poorly defined, non-localized cancer tumors of various shapes and sizes, including small metastatic tumor growths.

Previous reports suggest that the moderate heating efficiency of iron oxide nanoparticles combined with their relatively low tumor accumulation determine their limited application in systemically delivered magnetic hyperthermia.^{12, 13} Several preclinical studies have revealed the challenges associated with elevating intratumoral temperatures above 38 °C after intravenous injection of iron oxide nanoparticles at clinically relevant doses.¹⁴⁻¹⁶ To generate desired intratumoral temperatures, Huang *et al.* reported that mice require intravenous injection with conventional nanoparticles at an extremely high dose of 1700 mg of iron (Fe) per kg of body weight.¹² Importantly, the recommended intravenous dosage of the FDA-approved iron oxide nanoparticle, Ferumoxytol, is 510 mg, which corresponds to 8.5 mg of iron per kilogram of body weight for a 60 kg patient.^{17,18}

Many attempts have been made to develop efficient nanoparticles capable of generating sufficient heat at low concentrations in order to overcome the limitations of conventional iron oxide nanoparticles associated with their relatively low heating efficiency.^{4, 14, 19-26} A literature review, however, revealed that the heating efficiency of the developed nanoparticles was predominantly evaluated following intratumoral injections and the number of reports demonstrating the intratumoral heating efficiency of systemically administered nanoparticles is sparse.^{4, 14, 20, 21} One of the few available reports demonstrated that intravenously injected nanoclusters, composed of multiple iron oxide nanoparticles, were able to elevate the temperature of the tumor to ~38-39 °C.¹⁴ In a separate study, Xie *et al.* reported that cancer-targeted iron oxide nanoparticles co-doped with zinc and manganese elevated the temperature of tumors to ~40 °C following a single intravenous injection of a relatively high dose (30 mg Fe/kg).¹⁹ To further increase the average temperature of the tumor to ~42.8 °C, five repeated

intravenous injections of the developed nanoparticles were required, resulting in a total dose of ~150 mg of iron per kg of body weight.¹⁹

To the best of our knowledge, there are no published studies demonstrating nanoparticles capable of increasing intratumoral temperatures over 42 °C following a single intravenous injection at a clinically relevant dose. Therefore, we hypothesized that magnetic nanoclusters consisting of hexagon-shaped cobalt- and manganese-doped iron oxide nanoparticles (CoMn-IONP, Figure 2.1) can efficiently accumulate in cancer tumors following a single intravenous injection at a low dose (6.0 mg Fe/kg), elevate intratumoral temperature to 44 °C upon exposure to AMF, and significantly inhibit tumor growth.

2.3 MATERIALS AND METHODS

2.3.1 Materials

Iron (III) acetylacetonate ((Fe(acac)₃) was purchased from ACROS Organics (Fair Lawn, NJ). Oleylamine was purchased from Sigma-Aldrich (St. Louis, MO). Oleic acid, manganese (II) chloride tetrahydrate (MnCl₂·4H₂O), and cobalt (II) chloride hexahydrate (CoCl₂·6H₂O) were obtained from Alfa Aesar (Ward Hill, MA). Oleic acid-coated iron oxide nanoparticles (IONP, 15 nm) dispersed in tetrahydrofuran (THF) and iron oxide nanoparticles with carboxylic acid were obtained from Ocean NanoTech (San Diego, CA). Trioctyl ether and n-octyl ether were purchased from Tokyo chemical industry Co. (Tokyo, Japan). m-PEG-PCL (methoxy poly(ethylene glycol)-b-poly(ε-caprolactone), MW: 5k-10k) was obtained from Advanced Polymer Materials Inc. (Montreal, Canada). SiNc (silicon 2,3-naphthalocyanine bis(trihexylsilyloxy)) was purchased from Sigma-Aldrich (Milwaukee, WI). All other chemicals and supplies were obtained from VWR International (Radnor, PA).

2.3.2 Methods

2.3.2.1 Synthesis of cobalt- and manganese-doped iron oxide nanoparticles

Iron oxide nanoparticles doped with cobalt and manganese (CoMn-IONP) were synthesized by a modified thermal decomposition method.²⁷⁻²⁹ First, cobalt (II) chloride hexahydrate ($\text{CoCl}_2 \cdot 6\text{H}_2\text{O}$, 3.25 mmol) and iron (III) acetylacetonate ($\text{Fe}(\text{acac})_3$, 5.00 mmol) were added to a solution containing oleic acid (2.0 mL), oleylamine (2.0 mL) and trioctyl ether (20 mL). The obtained reaction mixture was placed in a 250 mL three-neck round-bottom flask and heated at 300 °C under nitrogen flow and vigorous stirring. After 1 h, the mixture was cooled to room temperature and the product was precipitated with ethanol (30 mL), followed by centrifugation at 7000 rpm for 30 min. The obtained precipitate was re-dispersed in hexane (10 mL), and the purification process was repeated three times to produce black cobalt ferrite (CoFe_2O_4) nanoparticles. In the next step, manganese chloride ($\text{MnCl}_2 \cdot 4\text{H}_2\text{O}$, 3.25 mmol) and $\text{Fe}(\text{acac})_3$ (5.00 mmol) were placed in a 250 mL three-neck round-bottom flask containing oleic acid (2.0 mL), oleylamine (2.0 mL) and trioctyl ether (20 mL). After addition of freshly made CoFe_2O_4 nanoparticles suspended in 10 mL of hexane (8 mg/mL), the reaction mixture was heated at 360 °C for 1 h under stirring and nitrogen flow. Subsequently, the resulting reaction mixture was cooled to room temperature, ethanol (30 mL) was added, followed by centrifugation at 7000 rpm for 30 min, and the obtained precipitate was re-dispersed in hexane (10 mL). The purification procedure was repeated three times. The obtained CoMn-IONP were dried at 70 °C for 12 h.

2.3.2.2 Nanoparticle characterization

The shape and size of the synthesized CoMn-IONP and IONP were examined using an FEI Tecnai™ Spirit transmission electron microscopy (TEM) system. The chemical composition and distribution of elements (Fe, Co, Mn) in a single CoMn-IONP was evaluated by energy

dispersive x-ray spectroscopy (EDX) using an FEI 80-300 kV Titan. The magnetization curves of tested nanoparticles were determined with a homemade vibrating magnetometer at room temperature.³⁰ The heating efficiency of nanoparticles in the presence of an alternating magnetic field generated by an induction heating system (MSI Automation, Wichita, KS) was evaluated, and the corresponding specific absorption rates (SAR) were calculated according to previously reported procedures.³⁰ Detailed characterization procedures are provided in Supporting Information.

2.3.2.3 Nanocluster preparation

Nanoclusters loaded with either CoMn-IONP or IONP were prepared by a solvent evaporation method.³¹⁻³³ Briefly, CoMn-IONP or IONP suspended in 1 mL of THF (8 mg Fe/mL) were added to 5 mL of THF solution containing m-PEG-PCL (2 mg/mL) followed by constant stirring for 20 min. Next, 6 mL of 5% dextrose solution in water was added to the reaction mixture and stirred for 20 min. THF was removed by using a rotovap. To remove any non-encapsulated, hydrophobic CoMn-IONP and non-soluble PEG-PCL molecules, the prepared aqueous solution was centrifuged at 1,000 g for 5 min and filtered through a 0.2 μ m cellulose acetate filter (cellulose acetate, VWR International, Radnor, PA). Of note, the employed methoxy PEG-PCL diblock copolymer consists of hydrophilic 5 kDa PEG and hydrophobic 10 kDa PCL blocks. Due to the high molecular weight of the hydrophobic PCL block, the copolymer has negligible water solubility and therefore free PEG-PCL molecules cannot be dissolved in the final aqueous solution of nanoclusters. The certificate of analysis provided by the manufacturer and the corresponding experiment in our lab validated that the employed PEG-PCL is insoluble in water. It is possible, however, that some PEG-PCL molecules could self-assemble into empty nanoparticles (without CoMn-IONP) during the preparation of nanoclusters. To remove any

empty PEG-PCL nanoparticles, the filtered solution was placed on a strong magnet (SuperMag Separator, Ocean NanoTech) for 6 h and PEG-PCL nanoparticles loaded with magnetic CoMn-IONP (nanoclusters) were separated and re-dispersed in 5% dextrose. The DLS spectra of CoMn-IONP nanoclusters and separately prepared empty PEG-PCL nanoparticles suggest that empty PEG-PCL nanoparticles were not present in the final nanocluster solution (Figure 2.21). High-performance liquid chromatography (HPLC) was also used to verify that THF (solvent) was not present in the final nanocluster solution (Figure 2.22).

2.3.2.4 Synthesis of spherical IONP:

Iron (III) acetylacetonate ($\text{Fe}(\text{acac})_3$, 5.00 mmol) were added to a solution containing oleic acid (2.0 mL), oleylamine (4.0 mL) and trioctyl ether (20 mL). The obtained reaction mixture was placed in a 250 mL three-neck round-bottom flask and heated to 300 °C under nitrogen flow and vigorous stirring. After 1 h, the mixture was cooled down to room temperature and the product was precipitated with ethanol (30 mL), followed by centrifugation at 7000 rpm for 30 min. The obtained precipitate was re-dispersed in hexane (10 mL), and the purification process was repeated three times to produce black iron oxide nanoparticle. The seed growth method was used to increase the size of iron oxide nanoparticles up to 15 nm.³⁴

2.3.2.5 Synthesis of SiNc-loaded CoMn-IONP nanoclusters:

The SiNc-loaded CoMn-IONP nanoclusters were prepared by a solvent evaporation method where CoMn-IONP nanoparticles suspended in THF (1 mL at 8 mg Fe/mL) were added to the THF solution containing PEG-PCL (5 mL at 2 mg/mL) and then silicon naphthalocyanine (SiNc, 0.5 mg/mL THF) was added followed by stirring for 20 min. Next, 5% dextrose solution in water (6 mL) was added to the reaction mixture and stirred for 20 min. THF was removed by using a rotovap. The obtained SiNc-loaded CoMn-IONP nanoclusters were filtered through a 0.2 μm

filter to remove any possible aggregate. To remove any empty PEG-PCL nanoparticles, the filtered solution was placed on a strong magnet (SuperMag Separator, Ocean NanoTech) for 6 h and PEG-PCL nanoparticles loaded with CoMn-IONP (nanoclusters) were separated and re-dispersed in 5% dextrose. Samples were analyzed in terms of composition, loading efficiency, and size.

2.3.2.6 Synthesis of water-soluble, individual CoMn-IONP and IONP:

Oleic acid coated CoMn-IONP and IONP, from Ocean NanoTech and our lab, were suspended in tetrahydrofuran and added to 2,3-Dimercaptosuccinic acid dissolved in DMSO, the mixture was vortexed for 24 h, and then nanoparticles were precipitated by centrifugation and dissolved in water. Finally, the solution was filtered through a 0.2 μ m syringe filter to remove any particle aggregates.

Iron oxide nanoparticles with carboxylic acid as a reference sample were purchased from Ocean NanoTech.³⁵

2.3.2.7 Nanocluster characterization

The hydrodynamic diameter, zeta potential, and polydispersity index (PDI) of the obtained nanoclusters were evaluated by dynamic light scattering (DLS, ZetaSizer NanoSeries, Malvern, UK).³¹⁻³³ The morphology and size of the nanoclusters were determined by transmission electron microscopy (TEM). The iron content in the obtained nanoclusters was determined using a colorimetric ferrozine-based assay according to our previously reported procedure.³⁰ The heating efficiency of the obtained nanoclusters in the presence of AMF was measured as described above and in Supporting Information.

2.3.2.8 In vitro studies

A2780/CDDP human ovarian carcinoma and ES-2 human ovarian clear cell carcinoma cell lines were purchased from Developmental Therapeutics Core (Northwestern University, IL) and ATCC (Manassas, VA) and cultured in RPMI 1640 medium supplemented with fetal bovine serum (10%) and penicillin-streptomycin (1%).

To evaluate the cytotoxicity of the developed nanoclusters, the employed cancer cells were seeded in 96-well plates at a density of 10×10^3 cells/well and allowed to grow for 24 h. Culture medium was removed, and the cells were treated for 24 h with 100 μ L of cell culture medium containing different concentrations (50-1000 μ g Fe/mL) of CoMn-IONP and IONP nanoclusters. After treatment, cell viability was evaluated using a modified Calcein AM assay according to a previously published protocol.³⁶

To evaluate cellular internalization efficiency, cancer cells seeded in T-25 cell culture flasks were incubated with 6 mL of media containing CoMn-IONP nanoclusters (100 μ g Fe/mL) for 24 h. Afterward, cells were collected, counted, rinsed with DPBS in pre-cleaned Sarstedt digestion tubes, and 10^6 cells were digested with 150 μ L of 75% HNO_3 (trace metal grade, Fisher Scientific, Fair Lawn, NJ) by incubating for 2 h at 90 °C. Finally, 850 μ L of 1% HNO_3 was added to each tube, and the amount of Fe in cancer cells was quantified by inductively coupled plasma mass spectrometry (ICP-MS) at the Oregon Health & Science University (OHSU) Elemental Analysis Core.

Evaluation of the heating efficiency of nanoclusters in vitro was accomplished according to our previously published protocol.³⁰ Briefly, after incubation with different non-toxic concentrations of CoMn-IONP nanoclusters (50, 100, 150, 200 μ g Fe/mL) and IONP nanoclusters (50 μ g Fe/mL) for 24 h, cancer cells were washed with DPBS, detached by 0.25% trypsin/EDTA and resuspended in cell culture media prior to counting. After counting, a portion of the cell

suspension containing 5×10^6 cells were centrifuged at 1000 rpm for 5 min to form the cell pellet. The pellets were maintained in a constant volume of 0.1 mL of cell culture media in a 0.5 mL microcentrifuge tube. Samples were then placed in the center of a 6-turn copper coil (inner diameter: 40 mm) and exposed to AMF (420 kHz, 26.9 kA/m) for 30 min. The temperature changes were measured by placing a fiber optic probe (Neoptix Inc., QC, Canada) inside the cell pellets. The water jacket inside the coil was maintained at $\sim 37^\circ\text{C}$, and the samples were allowed to equilibrate to this temperature before exposure to AMF. Controls were carried out with non-treated cells exposed to AMF alone and with cells exposed to no field.

To evaluate the anticancer effect of nanocluster-mediated magnetic hyperthermia, cancer cells were incubated with CoMn-IONP nanoclusters (50-200 $\mu\text{g Fe/mL}$) and IONP nanoclusters (50 $\mu\text{g Fe/mL}$) for 24 h and the formed cell pellets were exposed to AMF (420 kHz, 26.9 kA/m) for 30 min as described above. The cell pellets were maintained during exposure to AMF in a constant volume of 0.1 mL of cell culture media in a 0.5 mL microcentrifuge tube. Then, the cells were resuspended in media and seeded in 96-well plates at a density of 10×10^3 cells/well and cultured for an additional 48 h. Finally, cell viability was assessed using a Calcein AM assay.

2.3.2.9 In vitro toxicity studies:

To evaluate the cytotoxicity of the developed nanoclusters, the employed human embryonic kidney cells (HEK-293) were seeded in 96-well plates at a density of 10×10^3 cells/well and allowed to grow for 24 h. Culture medium was removed, and the cells were treated for 24 h with 100 μL of cell culture medium containing different concentrations (50-300 $\mu\text{g Fe/mL}$) of CoMn-IONP and IONP nanoclusters. After treatment, cell viability was evaluated using a modified Calcein AM assay according to a previously published protocol.³⁶

2.3.2.10 Genotoxicity studies:

Genotoxicity of the CoMn-IONP nanoclusters was evaluated using the in vitro micronucleus assay on CHO-K1 cells as previously described.³² Briefly, approximately 300,000 cells were cultured with media in a 6-well plate and held 24 hours before treatment. They were then incubated with tested samples for 24 h. Negative control cells were incubated with fresh media, while positive control cells were treated with ethyl methanesulfonate (EMS, 400 µg/mL) and 200 µg /mL of CoMn-IONP nanoclusters. After incubation, the cells were fixed in a cold solution of 100 % methanol for 10 minutes at room temperature. The methanol was removed and the cells were washed with Dulbecco's phosphate buffered saline (DPBS) and the cells' nuclei were then stained with Invitrogen NucBlue fixed cell reagent (DAPI) for 10 minutes in a 37°C incubator. This solution was removed, and all flasks were washed twice with DPBS containing 0.05 % Tween 20 (Bio-Rad Laboratories). After staining, the formation of micronuclei was detected using an EVOS FL Cell Imaging System (Life Technologies, Grand Island, NY) and documented by counting the number of micronuclei per 1000 cells.

2.3.2.11 In vivo studies

All animal studies were conducted under a protocol approved by the Institutional Animal Care and Use Committee of Oregon State University and Oregon Health and Science University.

Development of a subcutaneous xenograft mouse model of human ovarian cancer

Three million ES-2 cells re-suspended in 50 µL of RPMI 1460 medium, along with 50 µL of Matrigel, were injected subcutaneously into the flank of 5-week-old female nude mice purchased from Charles River Laboratories (Wilmington, MA, USA). The tumors were measured by a caliper every other day, and animal experiments started when tumors reached 50 mm³.

Evaluation of nanoclusters biodistribution

Five mice bearing subcutaneous xenografts of ES-2 ovarian cancer cells were injected via tail vein with 150 μ L of CoMn-IONP nanoclusters at a dose of 6 mg Fe/kg. The nanoclusters distribution in the mouse body after injection was monitored using the Pearl® Impulse Small Animal Imaging System at various time points after injection. For this purpose, nanoclusters were loaded with the near-infrared (NIR) fluorescent dye SiNc.White light and fluorescence images of each mouse were recorded and overlaid by the imaging system.

To confirm the accumulation of CoMn-IONP nanoclusters in tumors following i.v. injection, tissue samples dissected at 12 h after administration were stained with Prussian blue (iron) according to a previously published procedure³⁷

To quantify the amount of nanoclusters accumulated in tumors, the collected tissues were weighed and digested with 200 mL of 70% HNO₃ for 2 h at 90 °C. The iron (Fe) concentrations in the tested samples were determined using ICP-MS.

2.3.2.12 Evaluation of the therapeutic efficiency of nanoclusters-mediated hyperthermia

Mice bearing subcutaneous ES-2 xenografts were randomly divided into six groups with five animals per group. To evaluate the therapeutic efficacy of magnetic hyperthermia mediated by the developed nanoclusters, mice in groups 1 and 2 were injected intravenously (i.v.) with CoMn-IONP nanoclusters or IONP nanoclusters (5% dextrose solution), respectively, at a dose of 6 mg Fe/kg. Twelve hours following injection, animals were anesthetized using isoflurane in an induction chamber and maintained under anesthesia during treatment by isoflurane administration via a face mask. A fiber optic temperature probe was inserted into the center of the tumor following our previously reported procedure.³⁸ Afterward, each mouse was centered inside the induction coil, and temperature measurements were taken during animal exposure to AMF (420 kHz, 26.9 kA/m). When the intratumoral temperature reached 42 °C, AMF-induced

heating was continued for 10 min (total exposure time to AMF 30 min). Each group was treated once per week for 4 weeks with appropriate formulations. The tumor size in each group was measured every seven days for 5 weeks and compared to the tumor size of mice injected once per week for 4 weeks with 5% dextrose (group 3), CoMn-IONP nanoclusters (group 4), and IONP nanoclusters (group 5) without AMF exposure. To evaluate whether AMF alone increases the tumor temperature and demonstrates any anticancer effect, mice injected with 5% dextrose (group 6) were exposed to AMF once per week for 4 weeks as described above. To evaluate the influence of AFM exposure time on the therapeutic efficacy of CoMn-IONP nanoclusters-mediated hyperthermia, five mice were injected i.v. with CoMn-IONP nanoclusters at a dose of 6 mg Fe/kg. Twelve hours following injection, each mouse was centered inside the induction coil and exposed to AMF (420 kHz, 26.9 kA/m). When the intratumoral temperature reached 42 °C, AMF-induced heating was continued for 40 min (total exposure time to AMF 60 min).

To assess potential side effects caused by nanocluster-mediated hyperthermia, blood and organs were collected post-euthanasia and examined at the Oregon State University veterinary diagnostic laboratory.

Statistical analysis

The data were analyzed using descriptive statistics and presented as mean value \pm standard deviation (SD) from 3-5 separate measurements. Comparisons among groups were executed using independent samples Student's t-tests. Differences between groups were considered statistically significant at $p < 0.05$.

2.3.2.13 Transmission Electron Microscopy (TEM):

The size and morphology of the synthesized nanoparticles were evaluated using FEI Titan 80-200 transition electron microscope (FEI, Hillsboro, OR). 5-7 μ l of nanoparticles were deposited

onto glow discharged carbon formvar 400 Mesh copper grids (Ted Pella 01822-F) for 3 min, rinsed 15 secs in water, wicked on Whatman filter paper 1, stained for 60 seconds in filtered 1.33 % (w/v) uranyl acetate in water, wicked and air dried. Samples were imaged at 120 kV on a FEI Tecnai™ Spirit TEM system. Images were acquired as 2048×2048 pixel, 16-bit gray scale files using the FEI's TEM Imaging & Analysis (TIA) interface on an Eagle™ 2K CCD multiscan camera. Images were acquired at 2-4 microns defocused to improve contrast. All measurements were performed at 25 °C after pre-equilibration for 2 min and each parameter was measured in triplicate.

2.3.2.14 Magnetic measurements

The magnetization curves of CoMn-IONP and IONP were measured at room temperature using a custom-built vibrating sample magnetometer in Dr. Dhagat's laboratory.³⁰ The magnetometer is calibrated using a 2.383 mm diameter nickel sphere standard (SRM 772a from the National Institute of Standards and Technology, Gaithersburg, MD, USA) with a saturation magnetic moment of $3.47 \text{ mA} \cdot \text{m}^2$ at 0.5 Tesla. The hysteresis of the magnetization was evaluated by changing outside fields between +0.6 and -0.6 T at a temperature of 300 K.

2.3.2.15 Chemical composition structure:

The chemical composition of the synthesized nanoparticles was evaluated using FEI 80-300 kV Titan (S)TEM equipped with a spherical aberration image corrector. 5 -7 μL of nanoparticle solution were deposited onto the TEM grid. A TEM grid was held by a pair of self-closing tweezers. A small amount of liquid was drawn into a glass pipet. A small amount of that liquid was placed on the TEM grid. After waiting for 10-15 seconds, the liquid was wicked away with filter paper.

2.3.2.16 Specific absorption rate (SAR):

To measure the SAR values of CoMn-IONP, IONP and the developed nanoclusters, each sample (Fe concentration 1 mg/mL) was transferred into a standard 0.5 mL microcentrifuge tube and inserted into the insulating sample holder. The sample holder was then placed in the center of a 6-turn copper coil (40 mm inner diameter), connected to a radio frequency (RF) generator (MSI automation, Wichita, KS) that produces AMF. To minimize the influence of heat rising near the coil on the samples, the coil was cooled with circulating cold water. Within the coil, a jacket, through which polypropylene based coolant was circulated, additionally provided a thermal barrier to heat generated directly by the coil. The coolant temperature was adjusted in order to obtain an equilibrium temperature of $\sim 30^{\circ}\text{C}$ for all the samples prior to AMF application. The samples were then exposed to AMF of 26.9 kA/m or 10.6 kA/m amplitude and the temperature rise was recorded in 10-s intervals with a fiber optic probe (Neoptix Inc., QC, Canada) placed in the center of the sample solution. The SAR values of CoMn-IONP, IONP and the prepared nanoclusters were determined from the initial slope of the time-temperature curve (dT/dt), as described previously.³⁰ SAR was calculated using the following equation:

$$\text{SAR} = (CV_s/m) \times (dT/dt)$$

where C is the specific heat capacity of the medium ($C_{\text{water}} = 4.185 \text{ J g}^{-1} \text{ }^{\circ}\text{C}^{-1}$ and $C_{\text{THF}} = 4.434 \text{ J g}^{-1} \text{ }^{\circ}\text{C}^{-1}$), V_s is the sample volume, m is the mass of iron in the sample and dT/dt is the initial slope of the time-dependent temperature curve.

2.3.2.17 Prussian blue staining:

Briefly, Prussian blue staining was performed using the iron stain kit (Polysciences, Inc., Warrington, PA, USA). The assay was performed by placing deparaffinized slides in a working solution of equal amounts of 4% Potassium Ferrocyanide and 4% hydrochloric acid. The staining took 2 changes of the working solution at 10 minutes each. Then, slides were rinsed in several

changes of distilled water, counter-stained with nuclear-fast red for 3-5 minutes. Finally, the slides rinsed in running tap water for 1 minute. Dehydrated through ascending alcohols to xylene and cover slipped with ploy mount. Slides were imaged with an EVOS FL Cell Imaging System (Life Technologies, Grand Island, NY).

Evaluation of Co leaching from nanoclusters of CoMn-IONP:

CoMn-IONP nanoclusters (200 µg/mL) were incubated at 37°C in complete culture medium (RPMI) containing 10% fetal bovine serum for 7 days. After that, the samples were centrifuged at 10,000 rpm for 20 mins; supernatants were collected and digested with HNO₃. The total amount of Co and Mn ions in the medium was determined by ICP-MS.

2.3.2.18 Detection of tetrahydrofuran by reversed-phase high-performance liquid chromatography (RP-HPLC):

A Shimadzu RP-HPLC system was employed to determine whether trace amounts of tetrahydrofuran (THF) solvent was present in the final aqueous solution of the prepared CoMn-IONP nanoclusters. The HPLC system consists of LC-20 AD liquid chromatograph, SPD-M20A diode array detector, SIL-20A HT autosampler, and Shimadzu C18 column (5 µm. 50 x 4.6 mm). Elution of the samples was carried out in an isocratic mode with acetonitrile/water (60/40 v/v %) stabilized with 0.1% trifluoric acid. The flow rate was kept at 0.5 mL/min and injection volume of 10 µL. The column temperature was maintained at 40 °C with a run time of 15 min. The spectrophotometric peak was detected at 190 nm using a diode array detector. The following samples were analyzed: (1) aqueous solution of CoMn-IONP nanoclusters diluted in acetonitrile, (2) 5 µL THF was added to 995 µL aqueous solution of CoMn-IONP nanoclusters diluted in acetonitrile, and (3) acetonitrile only.

2.4 RESULTS AND DISCUSSION

2.4.1 Development and characterization of nanoclusters with enhanced heating efficiency

The literature suggests that nanoparticles with non-spherical shapes (*e.g.*, cubical, hexagonal) demonstrate superior heating efficiency in comparison to their spherical counterparts of the same size and composition.^{25, 39} However, non-spherical nanoparticles have not been adequately explored yet for systemically delivered magnetic hyperthermia. In an attempt to develop systemically delivered intratumoral nanoheaters with high heating efficiency, we, therefore, synthesized hexagon-shaped iron oxide nanoparticles (IONP, Figure 2.1) coated with oleic acid. According to the literature, nanoparticles of hexagonal shape demonstrate enhanced heating performance due to their optimal surface magnetic anisotropy.³⁹ To further enhance their heating efficiency, hexagonal IONP were doped with cobalt (Co) and manganese (Mn). Incorporating certain metals into iron oxide nanoparticles at a specific ratio can enhance their magnetic properties and improve the heating performance of magnetic nanoparticles.^{20, 23, 26, 27}

Bauer *et al.* previously suggested that heating efficiency of spherical iron oxide nanoparticles could potentially be enhanced by changing both the shape and composition of nanoparticles.⁴⁰ It was confirmed that iron oxide nanoparticles with both cubical shape and Zn doping exhibited significantly higher heating efficiency than Zn-doped spherical nanoparticles and non-doped cubical nanoparticles alone.⁴⁰

TEM imaging revealed that synthesized CoMn-IONP display an irregular hexagonal shape with an average size (width) of 14.80 ± 3.52 nm (Figure 2.2A). The size of CoMn-IONP was measured as the longest distance between two opposite vertices of the irregular hexagon (Figure 2.2A, inset). The EDX (energy dispersive x-ray spectroscopy) spectrum of CoMn-IONP reveals the presence of Fe, Co, and Mn within the magnetic nanoparticles (Figure 2.2B). EDX

spectroscopy analysis of multiple nanoparticles further confirmed that each CoMn-IONP contains $8.14 \pm 0.98\%$ Co and $5.3 \pm 0.82\%$ Mn (Figure 2.9).

Finally, the EDX line scanning profile verified that Fe, Co, and Mn are distributed through the entire nanoparticle (Figure 2.2C). In addition, EDX mapped images of CoMn-IONP (Figure 2.10) confirmed that Co, Mn and Fe elements are distributed throughout the nanoparticle.

In order to make a valid comparison and estimate the efficiency of the developed nanoheaters in an unbiased manner, commercially available spherical IONP⁴¹ with a similar size (14.91 ± 1.12 nm) and surface coating (oleic acid) were used as a reference sample in all of the studies (Figure 2.11). The magnetization curves of CoMn-IONP and IONP nanoparticles were recorded using a custom-built vibrating magnetometer at room temperature (Figure 2.2D). Our measurements verified that the saturation magnetization (M_s) of the developed CoMn-IONP ($93 \text{ Am}^2/\text{kg}$) is 1.7 times higher than that of the spherical IONP ($54 \text{ Am}^2/\text{kg}$) tested under identical conditions (Figure 2.2D). The saturation magnetization was normalized by the total weight of nanoparticles. The obtained M_s value of $93 \text{ Am}^2/\text{kg}$ (93 emu/g) for the developed 15 nm CoMn-IONP is in good agreement with previous reports.²⁷ For example, Lee *et al.* reported the M_s value of 110 emu/g (measured at 300 K) for 15 nm core-shell $\text{CoFe}_2\text{O}_4@\text{MnFe}_2\text{O}_4$ nanoparticles.²⁷ As shown in Figure 2.2D, almost no coercivity is observed for either CoMn-IONP nanoparticles or IONP, reaffirming their superparamagnetic properties at room temperature.²⁶ Of note, a specific absorption rate (SAR), as a measure of nanoparticle heating efficiency, is highly dependent on, and proportional to, the saturation magnetization.^{42, 43} It is also known that SAR values depend on the size and shape of nanoparticles as well as on AMF parameters (frequency (f) and magnetic field strength (H)) during measurement.²⁵ Consequently, a comparison of SAR values of nanoparticles with different shapes or sizes will naturally be biased toward a certain type of

nanoparticle. According to the literature, however, this strategy is widely used to evaluate the effect of shape or size on nanoparticles heating efficiency.^{25, 26, 40, 44, 45} Therefore, we compare SAR values of spherical IONP and hexagonal-shaped CoMn-IONP with similar size (IONP: 14.91 ± 1.12 nm vs CoMn-IONP: 14.80 ± 3.52 nm) and surface coating upon exposure to AMF with the same parameters ($f = 420$ kHz; $H = 26.9$ kA/m, $H \times f = 11.3 \times 10^9$ A m⁻¹ s⁻¹). Based on the obtained heating profiles of CoMn-IONP and IONP in tetrahydrofuran (THF) (Figure 2.2E), it was further calculated that CoMn-IONP have a specific absorption rate 3.6 times larger than that of IONP with values of 1718.0 and 475.3 W/g, respectively, under the same experimental conditions ($f = 420$ kHz; $H = 26.9$ kA/m). In addition, oleic acid-coated IONP with an average diameter of 13.97 ± 3.63 nm (Figure 2.12A) were prepared in our lab under the same experimental conditions used for CoMn-IONP synthesis and their heating efficiency was evaluated (Figure 2.12B). The obtained results revealed that our IONP with a SAR value of 586.2 W/g ($f = 420$ kHz; $H = 26.9$ kA/m) demonstrate slightly higher heating efficiency than commercially available IONP (475.3 W/g) and significantly lower heating efficiency than CoMn-IONP (1718.0 W/g).

To minimize non-selective heating of healthy tissue in patients by AMF alone, Hergt *et al.* proposed that the product of the magnetic field strength and the frequency ($H \times f$) should be $\leq 5 \times 10^9$ A m⁻¹ s⁻¹.⁴⁶ Therefore, the heating profiles of spherical and hexagonal-shaped nanoparticles were recorded (Figure 2.13A) upon exposure to AFM with the suggested field–frequency product of 4.5×10^9 A m⁻¹ s⁻¹ ($f = 420$ kHz; $H = 10.6$ kA/m). It was calculated that the SAR value of CoMn-IONP (897.9 W/g) is 6.2 and 2.6 times higher than that of commercially available IONP (145.9 W/g) and IONP prepared in our lab (348.5 W/g) under the same experimental conditions ($f = 420$ kHz; $H = 10.6$ kA/m), respectively.

To transform hydrophobic, oleic acid-coated, CoMn-IONP into a water-soluble nanopatform, the constructs were loaded into the hydrophobic interior of a PEG-PCL-based polymeric nanoparticle (Figure 2.1). PEG-PCL-based delivery vehicles were selected for the developed nanoheaters based on previous reports confirming their safety and biocompatibility.^{32, 33} Most importantly, systemic administration of PEG-PCL-based polymeric nanoparticles was reported to efficiently deliver hydrophobic payloads to subcutaneous and orthotopic cancer tumors while preventing their leaching into systemic circulation.^{32, 33} Furthermore, PEG-PCL-based carriers are simple to prepare and characterized by a uniform size distribution, extended shelf life, and batch-to-batch reproducibility.^{32, 33} All of these features are critical requirements for clinical translation of nanomedicines. The CoMn-IONP nanoclusters were prepared by using our previously developed solvent evaporation approach for transformation of hydrophobic entities into water-soluble PEG-PCL-based polymeric nanopatforms.³³ Our previous reports confirm that this highly reproducible approach results in PEG-PCL-based polymeric nanoparticles with monodispersed size distribution as indicated by a polydispersity index (PDI) of ≤ 0.1 .^{32, 33} Of note, PDI values of ≤ 0.1 specify unimodal distribution of nanoparticles. Briefly, this approach is based on solubilizing hydrophobic entities (*e.g.*, oleic acid-coated CoMn-IONP) and non-water soluble PEG-PCL copolymer in THF followed by the addition of water to produce an emulsion. After evaporation of THF, the amphiphilic PEG-PCL molecules, which consist of hydrophilic 5 kDa poly(ethylene glycol) (PEG) and hydrophobic 10 kDa poly(ϵ -caprolactone) (PCL) blocks, self-assemble in aqueous solution to form nanoparticles with a hydrophobic PCL core suitable for loading multiple hexagon-shaped CoMn-IONP (Figure 2.1). TEM images reveal that CoMn-IONP form clusters within a single PEG-PCL nanoparticle (Figure 2.3A, inset). The final nanoclusters have a hydrodynamic size of 78.67 ± 0.49 nm (Figure 2.3A) with a monodispersed

size distribution (PDI = 0.113), and a slightly negative charge (-2.64 ± 0.34 mV). The obtained size of nanoclusters was achieved by dissolving the appropriate concentrations of CoMn-IONP (1.33 mg Fe/mL) and PEG-PCL (1.67 mg/mL) in 6 mL of THF. The nanoclusters are characterized by an extended shelf life, which further indicates their translational potential: no noticeable change in nanoparticle size distribution and surface charge was detected over the tested 12-week period (Figure 2.3A).

As a control, we used the same approach to prepare nanoclusters of commercially available, spherical IONP with similar parameters (size: 89.52 ± 1.17 nm (Figure 2.11B, C); PDI: 0.104; surface charge: -5.40 ± 0.83 mV). We demonstrated that the developed CoMn-IONP nanoclusters in aqueous solution have a significantly higher heating efficiency upon exposure to AMF ($f = 420$ kHz; $H = 26.9$ kA/m) than the nanoclusters of spherical IONP (IONP nanoclusters). Figure 2.3B demonstrates that CoMn-IONP nanoclusters increased the solution temperature by 40 °C within 10 min (red curve), while the temperature increase mediated by nanoclusters of spherical IONP (black curve) was only 20 °C under identical conditions. It was calculated that the SAR value ($f = 420$ kHz; $H = 26.9$ kA/m) of CoMn-IONP nanoclusters (1237.0 W/g) in aqueous solution is 3.2 times higher than that of IONP nanoclusters (390.4 W/g). Previous reports suggest that clustering of magnetic nanoparticles produces strong magnetic dipole-dipole attractions between the nanoparticles that result in enhanced magnetic anisotropy at small cluster sizes, and helps to delay the relaxation time of magnetic moment, thereby maximizing their heating efficiency.^{14, 24, 42, 47} We also confirmed that CoMn-IONP nanoclusters exhibit enhanced heating efficiency when compared to their individual nanoparticles (Figure 2.3B, navy curve). The SAR values ($f = 420$ kHz; $H = 26.9$ kA/m) of individual CoMn-IONP and IONP dispersed in aqueous solution are only 997.2 W/g and 364.5

W/g, respectively. To obtain water-dispersed individual nanoparticles, a previously reported ligand exchange method was employed.⁴⁸ Briefly, dispersions of oleic acid-coated CoMn-IONP and IONP in THF were mixed with a solution of 2,3-Dimercaptosuccinic acid (DMSA) dissolved in DMSO and stirred for 24 h to allow the ligand exchange. Afterward, the particles were precipitated by centrifugation and re-dispersed in water. The TEM imaging revealed that individual nanoparticles with an average size of 18.94 ± 3.91 nm were obtained (Figure 2.14A). The size distribution of the prepared individual nanoparticles in aqueous solution was measured by DLS and validated by comparison to water-dispersed individual nanoparticles with 15 nm iron oxide core that were obtained from Ocean Nanotech (Figure 2.14B).³⁵

Of note, the measured SAR values ($f = 420$ kHz; $H = 26.9$ kA/m) of the individual oleic acid coated CoMn-IONP (1718.0 W/g) and IONP (475.3 W/g) are higher than the SAR values ($f = 420$ kHz; $H = 26.9$ kA/m) of the same CoMn-IONP (997.2 W/g) and IONP (364.5 W/g) transferred to water through oleic acid substitution with DMSA. This discrepancy could be related to the fact that the heating efficiencies of oleic acid and DMSA-coated nanoparticles were measured in different media, displaying different viscosities: THF (lower viscosity, 0.48 cP at 25 °C) and water (higher viscosity, 0.89 cP at 25 °C). The previous studies revealed a decrease in the SAR values with increasing solvent viscosity.^{44, 49} Therefore, it is important to compare the heating efficiency of nanoparticles measured in the same medium. Our data confirmed that the SAR values ($f = 420$ kHz; $H = 26.9$ kA/m) of water-dispersed nanoclusters of CoMn-IONP (1237.0 W/g) and spherical IONP (390.4 W/g) are higher than SAR values ($f = 420$ kHz; $H = 26.9$ kA/m) of individual CoMn-IONP (997.2 W/g) and IONP (364.5 W/g) dispersed in water. Of note, a large value of SAR is crucial for the use of nanoparticles for systemically delivered

magnetic hyperthermia because it allows a smaller dose of nanoparticles to be injected to achieve the desirable intratumoral temperature.

To validate the observed trend in the SAR values of nanoclusters and individual nanoparticles, we also employed oleic acid-coated IONP synthesized in our lab for use in preparation of corresponding nanoclusters (size: 80.10 ± 0.25 nm (Figure 2.12C); PDI: 0.180; surface charge: -2.48 ± 0.19 mV) and individual, water-dispersed IONP. The obtained data (Figure 2.12D) suggest the prepared nanoclusters (SAR: 493.8 W/g) demonstrate higher heating efficiency than their individual nanoparticles dispersed in aqueous solution (SAR: 391.3 W/g) under the same experimental conditions ($f = 420$ kHz; $H = 26.9$ kA/m). It was also confirmed that the SAR value of these nanoclusters (493.8 W/g) is 2.5 times lower than that of CoMn-IONP nanoclusters (1237.0 W/g). Finally, the SAR value ($f = 420$ kHz; $H = 26.9$ kA/m) of the individual oleic acid coated IONP (586.2 W/g) measured in THF is higher than the SAR value ($f = 420$ kHz; $H = 26.9$ kA/m) of the same DMSA-coated IONP (391.3 W/g) dispersed in water.

In addition, the heating efficiency of all nanoclusters was evaluated upon exposure to AFM with the field–frequency product of 4.5×10^9 ($f = 420$ kHz; $H = 10.6$ kA/m, Figure 2.13B). The SAR value of CoMn-IONP nanoclusters (732.4 W/g) is 11.8 and 3.3 times higher than that of nanoclusters of commercially available IONP (61.9 W/g) and IONP prepared in our lab (224.3 W/g), respectively.

2.4.2 *In vitro* characterization of the developed nanoclusters

In vitro studies revealed that the developed CoMn-IONP nanoclusters are non-toxic at high concentrations (~ 1000 $\mu\text{g/mL}$), efficiently deliver their payload into ovarian cancer cells and exhibit significant heating and therapeutic efficacy. ICP-MS measurements indicated that 14.04 ± 0.02 pg of iron was delivered to each cell as a result of incubation of ES-2 human ovarian

cancer cells with CoMn-IONP nanoclusters at an iron concentration of 100 $\mu\text{g/mL}$ for 24 h. The detected cellular internalization efficiency of the developed non-targeted CoMn-IONP nanoclusters is comparable with that of the previously reported iron oxide nanoparticles equipped with cancer-targeted peptides.³⁰ Despite their high internalization efficiency, the nanoclusters do not compromise the viability of cancer cells at iron concentrations up to 250 $\mu\text{g/mL}$ (Figure 2.4A), and cell viability only decreased by 10-25% at significantly high concentrations (300–1000 $\mu\text{g/mL}$) (Figure 2.15A).

It was also validated that the developed CoMn-IONP nanoclusters are not toxic to non-malignant, human embryonic kidney cells (HEK-293) at iron concentrations up to 300 $\mu\text{g/mL}$ (Figure 2.16A). Finally, *in vitro* micronucleus assay (formation of micronuclei) was performed to evaluate the genotoxicity of CoMn-IONP nanoclusters. Compared to the negative control, CoMn-IONP nanoclusters did not induce the formation of more micronuclei (Figure 2.16B), suggesting no genotoxicity observed at the tested concentration.

In contrast to CoMn-IONP nanoclusters, nanoclusters of commercially available IONP considerably reduced cancer cell viability at concentrations above 50 $\mu\text{g/mL}$ (Figure 2.4A). Of note, the developed hexagon-shaped CoMn-IONP and commercially available IONP have similar size and surface coating. Moreover, the prepared nanoclusters of CoMn-IONP and commercially available IONP are characterized by similar hydrodynamic size and surface charge. Therefore, we speculate that the observed discrepancy in toxicity profiles of the tested nanoclusters could be due to discrepancies in methods of nanoparticle preparation and purification used in our and Ocean NanoTech laboratories. This speculation can be further supported by the fact that the nanoclusters of IONP (prepared in our lab) do not compromise the

viability of ES-2 ovarian cancer cells and human kidney cells (HEK-293) at iron concentrations up to 300 $\mu\text{g/mL}$ (Figure 2.16C, D).

To evaluate and compare the heating efficiencies of both CoMn-IONP and IONP nanoclusters, ES-2 cells were incubated with nanoclusters at a non-toxic concentration of 50 $\mu\text{g/mL}$ for 24 h, and formed cell pellets were exposed to AMF at a magnetic field frequency of 420 kHz and strength of 26.9 kA/m. The recorded temperature profiles demonstrated that CoMn-IONP nanoclusters increased cellular temperature by 17 $^{\circ}\text{C}$ upon exposure to AMF, reaching 46 $^{\circ}\text{C}$ inside the cell pellets within ~ 8 min (Figure 2.4B). In comparison, the IONP nanoclusters were only capable of elevating cellular temperature by 3 $^{\circ}\text{C}$ under identical experimental conditions (Figure 2.4B).

To evaluate anticancer effect of nanocluster-mediated magnetic hyperthermia, ES-2 cells were incubated for 24 h with CoMn-IONP, and IONP nanoclusters (50 $\mu\text{g Fe/mL}$), and cell culture media (AMF) and the cells pellets (maintained in 0.1 mL of cell culture media) were exposed to AMF (420 kHz, 26.9 kA/m) for 30 min. Then, the cells were resuspended in media, seeded in 96-well plates at a density of 10^4 cells/well and were cultured for an additional 48 h. Cell viability measurements further demonstrated that magnetic hyperthermia mediated by CoMn-IONP nanoclusters at a concentration of 50 $\mu\text{g/mL}$ reduced the viability of cancer cells by $\sim 99\%$, while treatment mediated by IONP nanoclusters under the same experimental conditions was less efficient, resulting in only $\sim 10\%$ reduction of cellular viability (Figure 2.4C). Of note, the nanoclusters at the tested concentration of 50 $\mu\text{g/mL}$ (Figure 2.4A) or the applied AMF alone (Figure 2.4C) did not result in a significant reduction in cell viability. It was also confirmed that the heating and therapeutic efficiencies of magnetic hyperthermia depend on the concentration of the CoMn-IONP nanoclusters (Figure 2.15B, C). For example, CoMn-IONP nanoclusters

incubated with ES-2 cells at a non-toxic Fe concentration of 200 $\mu\text{g/mL}$ can further elevate the cellular temperature by 23 $^{\circ}\text{C}$ and consequently reduced cell viability by $\sim 100\%$ (Figure 2.15B, C). We also showed that the desired temperature increase could be achieved by varying AMF strength (Figure 2.15D), providing the possibility for controlling therapeutic temperature during treatment. Finally, the enhanced heating potency and therapeutic efficiency were also validated for the treatment of the platinum-resistant A2780 human ovarian cancer line (Figure 2.17).

2.4.3 *In vivo* evaluation of the developed nanoclusters

In vivo studies revealed that the CoMn-IONP nanoclusters intravenously (i.v.) injected into nude mice bearing subcutaneous ovarian cancer xenografts of ES-2 cells efficiently accumulated in the tumors. The NIR fluorescence signal generated by the dye (SiNc), encapsulated into the CoMn-IONP nanoclusters, was detected in the tumor as early as ~ 10 min following intravenous administration and reached its maximum intensity at ~ 5 h with a gradual decrease at 24 h post-injection (Figure 2.5 and Figure 2.18).

Microscopic analysis of tumor slices, collected and stained with Prussian blue for Fe detection at 12 h post-injection, further confirmed accumulation and penetration of CoMn-IONP nanoclusters in the tumors following systemic administration (Figure 2.6).

Finally, by quantifying the amount of Fe in cancer tissue with ICP-MS, it was determined that 3.5% (26 μg of Fe per gram of tissue) of the injected dose accumulated in the tumor at 12 h post-injection. This value is relatively high based on a Chan *et al.* review of 117 papers, which reported that a mere 0.7% (median) of the administered nanoparticle dose is found to be delivered to solid tumors.⁵⁰ In a separate study, Hayashi *et al.* also reported that the concentration of folate receptor-targeted iron oxide nanoclusters in the tumor was only 1.3 μg Fe per gram of tissue (24 nmol Fe/g) at 24 h post i.v. injection.¹⁴ The detected nanocluster

concentration was capable of elevating the temperature of the tumor to ~38-39 °C upon exposure to AMF.¹⁴

The above-described results suggested that the systemically injected CoMn-IONP nanoclusters efficiently accumulated in the tumors *via* passive targeting (EPR effect). It is believed that long-circulating nanoparticles leak preferentially into cancer tissue through fenestrated tumor blood vessels and are then retained in the tumor bed due to reduced lymphatic drainage.⁵¹ Our nanoclusters' hydrodynamic size (78.67 nm, Figure 2.3A) is optimal for minimization of rapid clearance by the kidneys (<10 nm), identification by macrophages (<100 nm), and increased accumulation in cancer tumors through a leaky tumor vasculature (<200 nm).⁵²⁻⁵⁴ In addition, the PEG-PCL co-polymer introduces a hydrophilic, non-charged PEG layer to the nanocluster surface (Figure 2.1), which provides slightly negative zeta potential of the nanoparticles (-2.64 mV).³³ The PEG layer and neutral/ slightly negative surface charge significantly reduce non-specific interaction with plasma proteins, qualities which increase nanoparticle circulation in blood and enhance accumulation in cancer tumors.^{52, 55, 56} Finally, our previous reports confirmed that PEG-PCL-based polymeric nanoparticles prevent leaching of hydrophobic payloads into the systemic circulation and efficiently accumulate in subcutaneous and metastatic ovarian cancer tumors after i.v. injections *via* passive targeting.³² Notably, there is considerable debate in the literature surrounding the existence of the EPR phenomenon in human tumors. For example, Danhier indicated that there is great tumor heterogeneity among and even within separate tumors in patients with regard to the extent of vascular disarray and permeability (*e.g.*, “EPR”ness).⁵⁷ Leaders in the field including Mark Davis have noted from their clinical data that this EPR phenomenon does occur in human tumors,⁵⁸ however, it is not as universally present as previously hypothesized.⁵⁹ The over-enthusiasm for EPR effect, and subsequent backlash on

nanoparticle technologies, should not diminish its utility for the subset of patients in which it may exist. There are studies considering companion imaging agents to stratify patient populations where exploiting the EPR phenomenon would be effective.⁵⁹ Such a patient pre-selection would lead to improved response rates and facilitate the clinical translation of the proposed nanocluster-based magnetic hyperthermia.

By quantifying the amount of Fe in various organs, it was revealed that 6.2 % and 19.5% of the injected dose were found in the spleen and liver at 12 h post injection, suggesting that the developed nanoclusters of CoMn-IONP are cleared from the body by these organs.

Next, we demonstrated that 12 h after i.v. injection of the CoMn-IONP nanoclusters, the tumors were heated to 44 °C upon exposure to AMF (Figure 2.7A, red curve). In contrast, the intratumoral temperature measured by a fiber optic probe in mice treated with the same dose of nanoclusters of spherical IONP from Ocean NanoTech reached only 38.5 °C (Figure 2.7B, black curve). The nanoclusters of IONP from our lab demonstrated slightly better heating efficiency and increased intratumoral temperature to 40.5 °C under the same experimental conditions (Figure 2.19). The obtained results are in agreement with a previous report demonstrating that i.v. injection of 100 nm clusters consisting of spherical superparamagnetic IONP elevated the temperature of a subcutaneous tumor to ~39 °C upon exposure to AMF.¹⁴

Because several cycles of hyperthermia need to be performed during a treatment regimen, we also validated the efficiency of CoMn-IONP nanoclusters to generate the required intratumoral temperature during a 4th weekly treatment (Figure 2.7A, navy curve). In addition, it was detected that untreated mice exposed to AMF showed little elevation (~2 °C) in tumor temperature (Figure 2.7A, dark cyan curve).

Of note, Figure 2.7A shows that the intratumoral temperature prior to AMF exposure (0 h) is ~32 °C. It is presumably related to the fact that mice were maintained under isoflurane anesthesia during exposure to AMF and general anesthesia causes a loss in thermoregulation. The loss of temperature occurs in small rodents due to their high body surface area to volume ratio, and their reliance upon locomotor activity for heat generation.⁶⁰ A significant number of reports focused on evaluation of anticancer effects of nanoparticle-mediated magnetic hyperthermia in mice revealed that initial temperature of subcutaneous cancer tumors was in the range of 28 - 33 °C.^{5, 12, 14, 21, 44, 61} Our previous reports also confirmed that initial temperature of subcutaneous cancer tumors measured in nude mice that were anesthetized and placed on a heating pad (37 °C) was in the range of 31 - 34 °C.^{32, 33}

Finally, *in vivo* studies demonstrated that magnetic hyperthermia mediated by CoMn-IONP nanoclusters significantly inhibited the growth of tumors. Mice bearing subcutaneous xenografts of ovarian ES-2 cancer cells were injected i.v. with CoMn-IONP nanoclusters at a dose of 6 mg Fe/kg, and the whole mouse was exposed to AMF at 12 h post-injection. When intratumoral temperatures reached 42 °C, AMF-induced heating was continued for 10 min (total exposure time to AMF 30 min), and the treatment procedure was repeated once a week for four weeks. Thirty-five days after initiation of treatment, the tumor volume of mice treated with hyperthermia mediated by CoMn-IONP nanoclusters (Figure 2.7B, red curve) was 5 and 3 times smaller than that of mice treated with hyperthermia generated by nanoclusters of spherical IONP from Ocean Nanotech (Figure 2.7B, black curve) and nanoclusters of IONP prepared in our lab (Figure 2.19B, black curve), respectively.

The obtained results also confirmed that cancer growth was not affected by AMF alone (Figure 2.7B, dark cyan curve) or non-activated nanoclusters (Figure 2.7B, navy and olive curves). We

also demonstrated that the therapeutic efficacy of CoMn-IONP nanocluster-mediated hyperthermia significantly increases with AMF exposure time. The volume of tumor 28 days after treatment with one cycle of magnetic hyperthermia for 40 min was 3 times smaller than that of tumor exposed to 4 cycles of hyperthermia for 10 min (Figure 2.7C).

It is obvious that the employed mouse with a subcutaneous cancer xenograft is not an ideal model. However, this model was widely used in the previous reports to evaluate the potential of nanoparticles for systemically delivered magnetic hyperthermia.^{12, 14, 19} By using this model we were able to prove our hypothesis that the developed nanoclusters efficiently accumulate in cancer tissue after a single intravenous injection at a clinically relevant dose and increase intratumoral temperatures over 42 °C upon exposure to safe AMF. Most importantly, this model allowed monitoring intratumoral temperature in a minimally invasive way during hyperthermia treatment.

Despite the high intratumoral temperature (44 °C) and strong anticancer effect (Figure 2.7B), mice did not lose body weight (Figure 2.8A) or display any signs of toxicity (*e.g.*, appearance, death) after 4 cycles of nanocluster-mediated hyperthermia.

To evaluate the effect of the treatment on acute liver, renal and muscle toxicity, we measured the concentrations of surrogate biomarkers in the blood for liver function (ALP and ALT), muscle function (CK) (Figure 2.8B), and kidney function (BUN and Cr) (Figure 2.8C). In addition, the serum levels of blood electrolytes (Figure 2.8C) and proteins (Figure 2.8D) were evaluated as an indicator of major organ toxicity.⁶² The measured serum levels of blood electrolytes, proteins and surrogate biomarkers in the mice treated with 4 cycles of magnetic hyperthermia were not different than those of non-treated mice. These results show that repeated injections of CoMn-

IONP nanoclusters (6 mg Fe/kg) and exposure to the employed AMF (420 kHz; 26.9 kA/m) did not cause any acute toxicity.

The developed nanoclusters are doped with Co, and therefore it is expected that significant leaching of Co ions from these nanoclusters following systemic injection could result in toxic side effects. To address this concern, potential leaching of Co ions following the incubation of CoMn-IONP nanoclusters in complete culture medium at 37 °C for 7 days was evaluated. The obtained results revealed only negligible leaching of Co (< 0.03%) from the developed nanoclusters under these experimental conditions. The translational potential of the developed nanoclusters might also be supported by the results of a recent clinical trial that demonstrated no side effects in people who voluntarily ingested ~ 1.0 mg Co/day (0.080-0.19 mg Co/kg x day) of a commercially available cobalt supplement over a 3-mo period. This study concluded that peak cobalt whole blood concentrations ranging between 9.4 and 117 µg/L were not associated with clinically significant changes in basic hematologic and clinical variables.⁶³

It is a known fact that AMF with specific parameters (frequency (f) and magnetic field strength (H)) can cause excessive non-selective Joule heating of healthy tissue due to the generation of eddy currents.⁶⁴ To minimize undesired side effects of AMF on healthy tissue during magnetic hyperthermia, Hergt *et al.* suggested that focused AMF has to be applied to the targeted area of the body and the field–frequency product ($H \times f$) should be $\leq 5 \times 10^9 \text{ A m}^{-1} \text{ s}^{-1}$.⁴⁶ For example, AMF with a field–frequency product up to $1.8 \times 10^9 \text{ A m}^{-1} \text{ s}^{-1}$ ($f = 100 \text{ kHz}$; $H = 18 \text{ kA/m}$) was safely applied to the human brain in multiple 60 min sessions.^{1, 10, 65} Notably, the maximum allowed frequency and strength of AMF that can be considered safe and tolerable is not completely agreed upon by the magnetic hyperthermia community, and the main requirement is to minimize non-specific heating to tissue due to eddy currents generated by AMF alone.^{42, 66}

Currently, several groups work on the development of different strategies to decrease eddy current heating during magnetic hyperthermia⁶⁴ and, therefore the suggested upper limit for the product of frequency and field strength may be reconsidered in the future. Consequently, clinical safety studies will be needed for each developed magnetic hyperthermia regimen achieved with the specific AMF system. Although the product of frequency and field strength ($f = 420$ kHz; $H = 26.9$ kA/m, $H \times f = 11.3 \times 10^9$ A m⁻¹ s⁻¹) used in the current studies was 2.3 times higher than the previously suggested upper limit ($\leq 5 \times 10^9$ A m⁻¹ s⁻¹), both *in vitro* and *in vivo* studies validated the safety and tolerability of the selected AMF parameters. The recorded temperature profiles suggest that AMF alone only increases intratumoral and rectal temperatures by 2.3 °C and 1.5 °C, respectively (Figure 2.7A, dark cyan curve and Figure 2.20). In a clinical trial, median rectal temperature of prostate cancer patients was 39.8 °C during magnetic hyperthermia treatment and the applied AMF was tolerable without significant side effects.⁹ The obtained results also confirmed that AMF alone did not significantly affect cell viability *in vitro* (Figure 2.4C) or tumor growth in animal studies (Figure 2.7B). It was further documented that after whole-body exposure to the selected AMF for four sessions (30 min each), mice displayed no signs of discomfort or toxicity. Finally, it was revealed that the employed AMF did not cause any major organ toxicity (Figure 2.8B-D).

Of note, the current report demonstrates proof of concept that PEG-PCL-based nanoclusters of magnetic nanoparticles with high heating efficiency can increase intratumoral temperatures over 42 °C following a single intravenous injection at a clinically relevant dose and upon exposure to safe AMF. However, the developed nanoclusters could potentially be optimized in order to provide similar or even higher heating efficiency *in vivo* upon exposure to AFM with the previously suggested parameters ($H \times f = 5 \times 10^9$ A m⁻¹ s⁻¹). For example, one strategy might be

to increase the nanoclusters accumulation and retention in cancer tumors by modifying their surface with cancer targeting moieties. The previous reports by Chen *et al.* concluded that various targeted nanoparticles outperformed non-targeted nanoparticles, affording ≥ 2 times higher delivery efficiency to tumors.^{50, 67, 68} It was also revealed that accumulation in the RES organs (*e.g.*, liver) was significantly lower for the targeted nanoparticles.⁶⁸ The non-targeted nanoclusters reported herein show significantly higher accumulation in tumors after intravenous injection (3.5% ID (injected dose)) relative to that reported by Chen *et al.* ($< 1\%$ ID). If the targeting moieties could provide ~ 2 times higher delivery of these nanoclusters to tumors while limiting their accumulation in healthy tissue, their ability to generate high intratumoral temperature upon exposure to AMF with low parameters will be substantially improved. Another strategy could be to further increase the SAR of the current CoMn-IONP that are clustered in the hydrophobic interior of a PEG-PCL-based delivery vehicle. It could be achieved by modifying CoMn-IONP core size, shape, composition, *etc.* Moreover, hydrophobic nanoparticles with a superior SAR that will be developed in the future could also be encapsulated into the reported PEG-PCL-based nanoclusters.

2.5 CONCLUSIONS

In summary, we have designed and synthesized efficient hexagon-shaped iron oxide nanoparticles doped with Co and Mn and confirmed that they exhibit significantly higher saturation magnetization and heating efficiency in comparison with conventional spherical iron oxide nanoparticles. The developed nanoparticles clustered inside a PEG-PCL-based nanocarrier were found to be safe and efficiently accumulated in cancer tumors following intravenous administration. Moreover, we demonstrated that systemically delivered nanoclusters elevate the

intratumoral temperature up to 44 °C in the presence of a safe AMF, and the required temperatures could be achieved after repeated injections of the nanoclusters. Finally, animal studies validated that the nanocluster-mediated hyperthermia efficiently inhibited the growth of subcutaneous ovarian tumors. These nanoparticles, and their capability to achieve therapeutically relevant temperatures in tumors following a single intravenous injection at low dose, will allow the scientific community to exploit the full potential of magnetic hyperthermia for treatment of cancer, either alone or in combination with other therapies including radiation, chemotherapy, or immunotherapy. To further advance this technology, it will be important in future studies to evaluate the therapeutic efficacy of the developed nanoclusters in orthotopic animal models with deep-seated primary and metastatic tumors. In addition, to minimize non-specific heating of healthy tissues due to eddy currents, there is a need to optimize current, or develop new, AMF systems that can deliver the focused AMF to a small part of the body where the cancer tumor is located.

2.6 ACKNOWLEDGMENTS

This research was supported by NIH/NBIB (1R15EB020351-01A1), the College of Pharmacy at Oregon State University (OSU), Najran University, and National Center for Advancing Translational Sciences of NIH (KL2 TR002370). The funding sources had no involvement in the collection, analysis, and interpretation of the data or in the decision to submit the article for publication. Electron microscopy was performed using the Multiscale Microscopy Core (MMC) at Oregon Health & Science University with technical support from the (OHSU)-FEI Living Lab and the Center for Spatial Systems Biomedicine (OCSSB). ICP-MS measurements were

performed by M. Ralle at the OHSU Elemental Analysis Core with partial support from NIH core grant S10RR025512.

2.7 REFERENCES

1. Luo, S.; Wang, L. F.; Ding, W. J.; Zhou, M. J.; Jin, H. K.; Su, S. F.; Ouyang, W. W., Clinical trials of magnetic induction hyperthermia for treatment of tumours. *OA Cance* **2014**, 2 (1), 2.
2. Torres-Lugo, M.; Rinaldi, C., Thermal potentiation of chemotherapy by magnetic nanoparticles. *Nanomedicine (Lond)* **2013**, 8 (10), 1689-707.
3. Deatsch, A. E.; Evans, B. A., Heating efficiency in magnetic nanoparticle hyperthermia. *Journal of Magnetism and Magnetic Materials* **2014**, 354, 163–172.
4. Kumar, C. S.; Mohammad, F., Magnetic nanomaterials for hyperthermia-based therapy and controlled drug delivery. *Advanced drug delivery reviews* **2011**, 63 (9), 789-808.
5. Sato, I.; Umemura, M.; Mitsudo, K.; Fukumura, H.; Kim, J. H.; Hoshino, Y.; Nakashima, H.; Kioi, M.; Nakakaji, R.; Sato, M.; Fujita, T.; Yokoyama, U.; Okumura, S.; Oshiro, H.; Eguchi, H.; Tohnai, I.; Ishikawa, Y., Simultaneous hyperthermia-chemotherapy with controlled drug delivery using single-drug nanoparticles. *Scientific reports* **2016**, 6, 24629.
6. Shetake, N. G.; Balla, M. M. S.; Kumar, A.; Pandey, B. N., Magnetic hyperthermia therapy: an emerging modality of cancer treatment in combination with radiotherapy. *Journal of Radiation and Cancer Research* **2016**, 7, 13-7.
7. Toraya-Brown, S.; Sheen, M. R.; Zhang, P.; Chen, L.; Baird, J. R.; Demidenko, E.; Turk, M. J.; Hoopes, P. J.; Conejo-Garcia, J. R.; Fiering, S., Local hyperthermia treatment of tumors induces CD8(+) T cell-mediated resistance against distal and secondary tumors. *Nanomedicine : nanotechnology, biology, and medicine* **2014**, 10 (6), 1273-1285.
8. Moy, A. J.; Tunnell, J. W., Combinatorial immunotherapy and nanoparticle mediated hyperthermia. *Advanced drug delivery reviews* **2017**, 114, 175-183.

9. Johannsen, M.; Gneveckow, U.; Taymoorian, K.; Thiesen, B.; Waldofner, N.; Scholz, R.; Jung, K.; Jordan, A.; Wust, P.; Loening, S. A., Morbidity and quality of life during thermotherapy using magnetic nanoparticles in locally recurrent prostate cancer: results of a prospective phase I trial. *Int J Hyperthermia* **2007**, *23* (3), 315-23.
10. Maier-Hauff, K.; Rothe, R.; Scholz, R.; Gneveckow, U.; Wust, P.; Thiesen, B.; Feussner, A.; von Deimling, A.; Waldoefner, N.; Felix, R.; Jordan, A., Intracranial thermotherapy using magnetic nanoparticles combined with external beam radiotherapy: results of a feasibility study on patients with glioblastoma multiforme. *J Neurooncol* **2007**, *81* (1), 53-60.
11. Wust, P.; Gneveckow, U.; Johannsen, M.; Bohmer, D.; Henkel, T.; Kahmann, F.; Sehouli, J.; Felix, R.; Ricke, J.; Jordan, A., Magnetic nanoparticles for interstitial thermotherapy--feasibility, tolerance and achieved temperatures. *Int J Hyperthermia* **2006**, *22* (8), 673-85.
12. Huang, H. S.; Hainfeld, J. F., Intravenous magnetic nanoparticle cancer hyperthermia. *International journal of nanomedicine* **2013**, *8*, 2521-32.
13. Hilger, I., In vivo applications of magnetic nanoparticle hyperthermia. *International journal of hyperthermia : the official journal of European Society for Hyperthermic Oncology, North American Hyperthermia Group* **2013**, *29* (8), 828-34.
14. Hayashi, K.; Nakamura, M.; Sakamoto, W.; Yogo, T.; Miki, H.; Ozaki, S.; Abe, M.; Matsumoto, T.; Ishimura, K., Superparamagnetic nanoparticle clusters for cancer theranostics combining magnetic resonance imaging and hyperthermia treatment. *Theranostics* **2013**, *3* (6), 366-76.

15. Pham, H. N.; Pham, T. H.; Nguyen, D. T.; Phan, Q. T.; Le, T. T. H.; Ha, P. T.; Do, H. M.; N, H. T. M.; Nguyen, X. P., Magnetic inductive heating of organs of mouse models treated by copolymer coated Fe₃O₄ nanoparticles. *Advances in Natural Sciences: Nanoscience and Nanotechnology* **2017**, 8 025013.
16. Kalber, T. L.; Ordidge, K. L.; Southern, P.; Loebinger, M. R.; Kyrtatos, P. G.; Pankhurst, Q. A.; Lythgoe, M. F.; Janes, S. M., Hyperthermia treatment of tumors by mesenchymal stem cell-delivered superparamagnetic iron oxide nanoparticles. *International journal of nanomedicine* **2016**, 11, 1973-83.
17. https://www.rxlist.com/feraheme-drug.htm#indications_dosage.
18. Nguyen, K. L.; Yoshida, T.; Han, F.; Ayad, I.; Reemtsen, B. L.; Salusky, I. B.; Satou, G. M.; Hu, P.; Finn, J. P., MRI with ferumoxytol: A single center experience of safety across the age spectrum. *Journal of magnetic resonance imaging : JMRI* **2017**, 45 (3), 804-812.
19. Xie, J.; Yan, C.; Yan, Y.; Chen, L.; Song, L.; Zang, F.; An, Y.; Teng, G.; Gu, N.; Zhang, Y., Multi-modal Mn-Zn ferrite nanocrystals for magnetically-induced cancer targeted hyperthermia: a comparison of passive and active targeting effects. *Nanoscale* **2016**, 8 (38), 16902-15.
20. Xie, J.; Zhang, Y.; Yan, C.; Song, L.; Wen, S.; Zang, F.; Chen, G.; Ding, Q.; Yan, C.; Gu, N., High-performance PEGylated Mn-Zn ferrite nanocrystals as a passive-targeted agent for magnetically induced cancer theranostics. *Biomaterials* **2014**, 35 (33), 9126-36.
21. Cho, M.; Cervadoro, A.; Ramirez, M. R.; Stigliano, C.; Brazdeikis, A.; Colvin, V. L.; Civera, P.; Key, J.; Decuzzi, P., Assembly of Iron Oxide Nanocubes for Enhanced Cancer Hyperthermia and Magnetic Resonance Imaging. *Nanomaterials* **2017**, 7 (4).

22. Lartigue, L.; Hugounenq, P.; Alloyeau, D.; Clarke, S. P.; Levy, M.; Bacri, J. C.; Bazzi, R.; Brougham, D. F.; Wilhelm, C.; Gazeau, F., Cooperative organization in iron oxide multi-core nanoparticles potentiates their efficiency as heating mediators and MRI contrast agents. *ACS Nano* **2012**, *6* (12), 10935-49.
23. He, S.; Zhang, H.; Liu, Y.; Sun, F.; Yu, X.; Li, X.; Zhang, L.; Wang, L.; Mao, K.; Wang, G.; Lin, Y.; Han, Z.; Sabirianov, R.; Zeng, H., Maximizing Specific Loss Power for Magnetic Hyperthermia by Hard-Soft Mixed Ferrites. *Small* **2018**, e1800135.
24. Qu, Y.; Li, J.; Ren, J.; Leng, J.; Lin, C.; Shi, D., Enhanced magnetic fluid hyperthermia by micellar magnetic nanoclusters composed of $\text{Mn}(x)\text{Zn}(1-x)\text{Fe}_2\text{O}_4$ nanoparticles for induced tumor cell apoptosis. *ACS applied materials & interfaces* **2014**, *6* (19), 16867-79.
25. Guardia, P.; Di Corato, R.; Lartigue, L.; Wilhelm, C.; Espinosa, A.; Garcia-Hernandez, M.; Gazeau, F.; Manna, L.; Pellegrino, T., Water-soluble iron oxide nanocubes with high values of specific absorption rate for cancer cell hyperthermia treatment. *ACS Nano* **2012**, *6* (4), 3080-91.
26. Noh, S. H.; Na, W.; Jang, J. T.; Lee, J. H.; Lee, E. J.; Moon, S. H.; Lim, Y.; Shin, J. S.; Cheon, J., Nanoscale magnetism control via surface and exchange anisotropy for optimized ferrimagnetic hysteresis. *Nano letters* **2012**, *12* (7), 3716-21.
27. Lee, J. H.; Jang, J. T.; Choi, J. S.; Moon, S. H.; Noh, S. H.; Kim, J. W.; Kim, J. G.; Kim, I. S.; Park, K. I.; Cheon, J., Exchange-coupled magnetic nanoparticles for efficient heat induction. *Nature nanotechnology* **2011**, *6* (7), 418-22.
28. Sun, S.; Zeng, H., Size-controlled synthesis of magnetite nanoparticles. *J Am Chem Soc* **2002**, *124* (28), 8204-5.

29. Sun, S.; Zeng, H.; Robinson, D. B.; Raoux, S.; Rice, P. M.; Wang, S. X.; Li, G., Monodisperse MFe_2O_4 ($M = Fe, Co, Mn$) nanoparticles. *J Am Chem Soc* **2004**, *126* (1), 273-9.
30. Taratula, O.; Dani, R. K.; Schumann, C.; Xu, H.; Wang, A.; Song, H.; Dhagat, P.; Taratula, O., Multifunctional nanomedicine platform for concurrent delivery of chemotherapeutic drugs and mild hyperthermia to ovarian cancer cells. *Int J Pharm* **2013**, *458* (1), 169-180.
31. Duong, T.; Li, X.; Yang, B.; Schumann, C.; Alabrqi, H. A.; Taratula, O.; Taratula, O., Phototheranostic Nanoplatform Based on a Single Cyanine Dye for Image-Guided Combinatorial Phototherapy *Nanomedicine : nanotechnology, biology, and medicine* **2016**, [Epub ahead of print]
32. Li, X.; Schumann, C.; Albarqi, H. A.; Lee, C. J.; Alani, A. W. G.; Bracha, S.; Milovancev, M.; Taratula, O.; Taratula, O., A Tumor-Activatable Theranostic Nanomedicine Platform for NIR Fluorescence-Guided Surgery and Combinatorial Phototherapy. *Theranostics* **2018**, *8* (3), 767-784.
33. Taratula, O.; Doddapaneni, B. S.; Schumann, C.; Li, X.; Bracha, S.; Milovancev, M.; Alani, A.; Taratula, O., Naphthalocyanine-based biodegradable polymeric nanoparticles for image-guided combinatorial phototherapy. *Chemistry of Materials* **2015**, *27*, 6155 - 6165.
34. Sun, S.; Zeng, H.; Robinson, D. B.; Raoux, S.; Rice, P. M.; Wang, S. X.; Li, G., Monodisperse mfe_2o_4 ($m= fe, co, mn$) nanoparticles. *Journal of the American Chemical Society* **2004**, *126* (1), 273-279.
35. <https://www.oceannanotech.com/products-type/iron-oxide-nanoparticles-5-30nm/functionalized-iron-oxide-nanoparticles/carboxyl-iron-oxide-nanoparticles/carboxyl-iron-oxide-nanoparticles-534.html>.

36. Taratula, O.; Schumann, C.; Naleway, M. A.; Pang, A. J.; Chon, K. J., A multifunctional theranostic platform based on phthalocyanine-loaded dendrimer for image-guided drug delivery and photodynamic therapy. *Mol Pharm* **2013**, *10* (10), 3946-58.
37. Sharkey, J.; Lewis, P. J. S.; Barrow, M.; Alwahsh, S. M.; Noble, J.; Livingstone, E.; Lennen, R. J.; Jansen, M. A.; Carrion, J. G.; Liptrott, N., Functionalized superparamagnetic iron oxide nanoparticles provide highly efficient iron-labeling in macrophages for magnetic resonance-based detection in vivo. *Cytotherapy* **2017**, *19* (4), 555-569.
38. Taratula, O.; Schumann, C.; Duong, T.; Taylor, K. L., Dendrimer-encapsulated naphthalocyanine as a single agent-based theranostic nanopatform for near-infrared fluorescence imaging and combinatorial anticancer phototherapy. *Nanoscale* **2015**, *7* (9), 3888-902.
39. Wang, H.; Shrestha, T. B.; Basel, M. T.; Pyle, M.; Toledo, Y.; Konecny, A.; Thapa, P.; Ikenberry, M.; Hohn, K. L.; Chikan, V.; Troyerb, D. L.; Bossmann, S. H., Hexagonal magnetite nanoprisms: preparation, characterization and cellular uptake. *Journal of Materials Chemistry B* **2015**, *3*, 4647.
40. Bauer, L. M.; Situ, S. F.; Griswold, M. A.; Samia, A. C., High-performance iron oxide nanoparticles for magnetic particle imaging - guided hyperthermia (hMPI). *Nanoscale* **2016**, *8* (24), 12162-9.
41. <https://www.oceannanotech.com/products-type/iron-oxide-nanoparticles-5-30nm/iron-oxide-in-organic-solvents/sor-15.html>.
42. Obaidat, I. M.; Issa, B.; Haik, Y., Magnetic Properties of Magnetic Nanoparticles for Efficient Hyperthermia. *Nanomaterials* **2015**, *5* (1), 63-89.
43. Tong, S.; Quinto, C. A.; Zhang, L.; Mohindra, P.; Bao, G., Size-Dependent Heating of Magnetic Iron Oxide Nanoparticles. *ACS Nano* **2017**, *11* (7), 6808-6816.

44. Jang, J. T.; Lee, J.; Seon, J.; Ju, E.; Kim, M.; Kim, Y. I.; Kim, M. G.; Takemura, Y.; Arbab, A. S.; Kang, K. W.; Park, K. H.; Paek, S. H.; Bae, S., Giant Magnetic Heat Induction of Magnesium-Doped γ -Fe₂O₃ Superparamagnetic Nanoparticles for Completely Killing Tumors. *Advanced materials* **2018**, *30* (6).
45. Di Corato, R.; Espinosa, A.; Lartigue, L.; Tharaud, M.; Chat, S.; Pellegrino, T.; Menager, C.; Gazeau, F.; Wilhelm, C., Magnetic hyperthermia efficiency in the cellular environment for different nanoparticle designs. *Biomaterials* **2014**, *35* (24), 6400-11.
46. Hergt, R.; Dutz, S., Magnetic particle hyperthermia—biophysical limitations of a visionary tumour therapy. *Journal of Magnetism and Magnetic Materials* **2007**, *311*, 187-192.
47. Martinez-Boubeta, C.; Simeonidis, K.; Makridis, A.; Angelakeris, M.; Iglesias, O.; Guardia, P.; Cabot, A.; Yedra, L.; Estradé, S.; Peiró, F., Learning from nature to improve the heat generation of iron-oxide nanoparticles for magnetic hyperthermia applications. *Scientific reports* **2013**, *3*, 1652.
48. Salas, G.; Casado, C.; Teran, F. J.; Miranda, R.; Serna, C. J.; Morales, M. P., Controlled synthesis of uniform magnetite nanocrystals with high-quality properties for biomedical applications. *Journal of Materials Chemistry* **2010**, *22*, 21065.
49. Pineiro-Redondo, Y.; Banobre-Lopez, M.; Pardinas-Blanco, I.; Goya, G.; Lopez-Quintela, M. A.; Rivas, J., The influence of colloidal parameters on the specific power absorption of PAA-coated magnetite nanoparticles. *Nanoscale Res Lett* **2011**, *6* (1), 383.
50. Wilhelm, S.; Tavares, A. J.; Dai, Q.; Ohta, S.; Audet, J.; Dvorak, H. F.; Chan, W. C. W., Analysis of nanoparticle delivery to tumours. *Nature Reviews Materials* **2016**, *1*, 16014.

51. Maeda, H.; Nakamura, H.; Fang, J., The EPR effect for macromolecular drug delivery to solid tumors: Improvement of tumor uptake, lowering of systemic toxicity, and distinct tumor imaging in vivo. *Advanced drug delivery reviews* **2013**, *65* (1), 71-9.
52. Alexis, F.; Pridgen, E.; Molnar, L. K.; Farokhzad, O. C., Factors affecting the clearance and biodistribution of polymeric nanoparticles. *Mol Pharmaceut* **2008**, *5* (4), 505-515.
53. Longmire, M.; Choyke, P. L.; Kobayashi, H., Clearance properties of nano-sized particles and molecules as imaging agents: considerations and caveats. *Nanomedicine : nanotechnology, biology, and medicine* **2008**, *3* (5), 703-717.
54. Maruyama, K., Intracellular targeting delivery of liposomal drugs to solid tumors based on EPR effects. *Advanced drug delivery reviews* **2011**, *63* (3), 161-169.
55. Duan, X.; Li, Y., Physicochemical characteristics of nanoparticles affect circulation, biodistribution, cellular internalization, and trafficking. *Small* **2013**, *9* (9-10), 1521-32.
56. Petros, R. A.; DeSimone, J. M., Strategies in the design of nanoparticles for therapeutic applications. *Nature reviews. Drug discovery* **2010**, *9* (8), 615-27.
57. Danhier, F., To exploit the tumor microenvironment: Since the EPR effect fails in the clinic, what is the future of nanomedicine? *J Control Release* **2016**, *244* (Pt A), 108-121.
58. Clark, A. J.; Wiley, D. T.; Zuckerman, J. E.; Webster, P.; Chao, J.; Lin, J.; Yen, Y.; Davis, M. E., CRLX101 nanoparticles localize in human tumors and not in adjacent, nonneoplastic tissue after intravenous dosing. *P Natl Acad Sci USA* **2016**, *113* (14), 3850-4.
59. Golombek, S. K.; May, J. N.; Theek, B.; Appold, L.; Drude, N.; Kiessling, F.; Lammers, T., Tumor targeting via EPR: Strategies to enhance patient responses. *Advanced drug delivery reviews* **2018**, *130*, 17-38.

60. Kersemans, V.; Gilchrist, S.; Allen, P. D.; Beech, J. S.; Kinchesh, P.; Vojnovic, B.; Smart, S. C., A resistive heating system for homeothermic maintenance in small animals. *Magn Reson Imaging* **2015**, *33* (6), 847-51.
61. Kolosnjaj-Tabi, J.; Di Corato, R.; Lartigue, L.; Marangon, I.; Guardia, P.; Silva, A. K.; Luciani, N.; Clement, O.; Flaud, P.; Singh, J. V.; Decuzzi, P.; Pellegrino, T.; Wilhelm, C.; Gazeau, F., Heat-generating iron oxide nanocubes: subtle "destructorators" of the tumoral microenvironment. *ACS Nano* **2014**, *8* (5), 4268-83.
62. Shah, V. M.; Nguyen, D. X.; Alfatease, A.; Bracha, S.; Alani, A. W., Characterization of pegylated and non-pegylated liposomal formulation for the delivery of hypoxia activated vinblastine-N-oxide for the treatment of solid tumors. *J Control Release* **2017**, *253*, 37-45.
63. Tvermoes, B. E.; Unice, K. M.; Paustenbach, D. J.; Finley, B. L.; Otani, J. M.; Galbraith, D. A., Effects and blood concentrations of cobalt after ingestion of 1 mg/d by human volunteers for 90 d. *Am J Clin Nutr* **2014**, *99* (3), 632-46.
64. Stigliano, R. V.; Shubitidze, F.; Petryk, J. D.; Shoshiashvili, L.; Petryk, A. A.; Hoopes, P. J., Mitigation of eddy current heating during magnetic nanoparticle hyperthermia therapy. *Int J Hyperthermia* **2016**, *32* (7), 735-48.
65. Mahmoudi, K.; Bouras, A.; Bozec, D.; Ivkov, R.; Hadjipanayis, C., Magnetic hyperthermia therapy for the treatment of glioblastoma: a review of the therapy's history, efficacy and application in humans. *Int J Hyperthermia* **2018**, *34* (8), 1316-1328.
66. Ortega, D.; Pankhurst, Q., *Magnetic Hyperthermia*. 2013; Vol. 1.
67. Sykes, E. A.; Chen, J.; Zheng, G.; Chan, W. C., Investigating the impact of nanoparticle size on active and passive tumor targeting efficiency. *ACS Nano* **2014**, *8* (6), 5696-706.

68. Dai, Q.; Wilhelm, S.; Ding, D.; Syed, A. M.; Sindhwani, S.; Zhang, Y.; Chen, Y. Y.; MacMillan, P.; Chan, W. C. W., Quantifying the Ligand-Coated Nanoparticle Delivery to Cancer Cells in Solid Tumors. *ACS Nano* **2018**, *12* (8), 8423-8435.

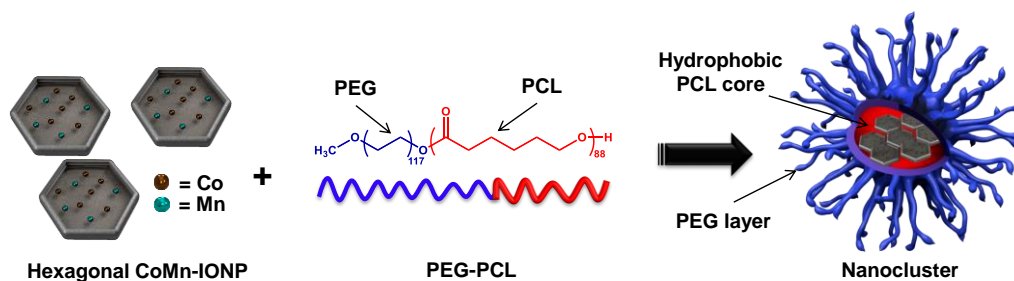


Figure 2.1: Schematic illustration of the nanoclusters for magnetic hyperthermia.

The nanoclusters are prepared by encapsulation of hexagon-shaped cobalt- and manganese-doped iron oxide nanoparticles (CoMn-IONP) into the hydrophobic core of PEG-PCL-based nanocarriers.

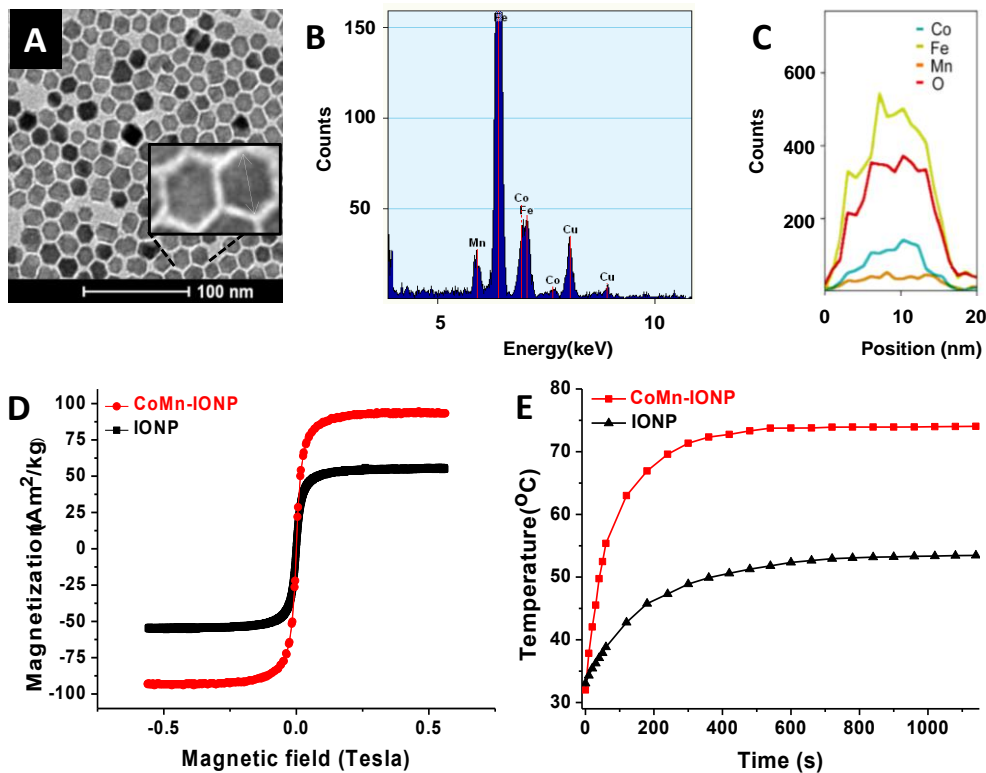


Figure 2.2: Characterization of CoMn-IONP and IONP.

(A) Representative TEM image of hexagonal iron oxide nanoparticles doped with Co and Mn (CoMn-IONP). (B) Representative EDX spectrum of CoMn-IONP demonstrating the presence of Co, Mn, and Fe in CoMn-IONPs. (C) Co, Fe, Mn and oxygen (O) EDX line scanning profile of a single CoMn-IONP confirms that Co and Mn are distributed throughout the nanoparticle. (D) Magnetization curves of CoMn-IONP (red) and spherical IONP (black) at room temperature. The magnetization values were normalized by the total weight of nanoparticles. (E) Heating profiles of CoMn-IONP and IONP dispersed in THF (1 mg Fe /mL) and subjected to AMF (420 kHz, 26.9 kA/m).

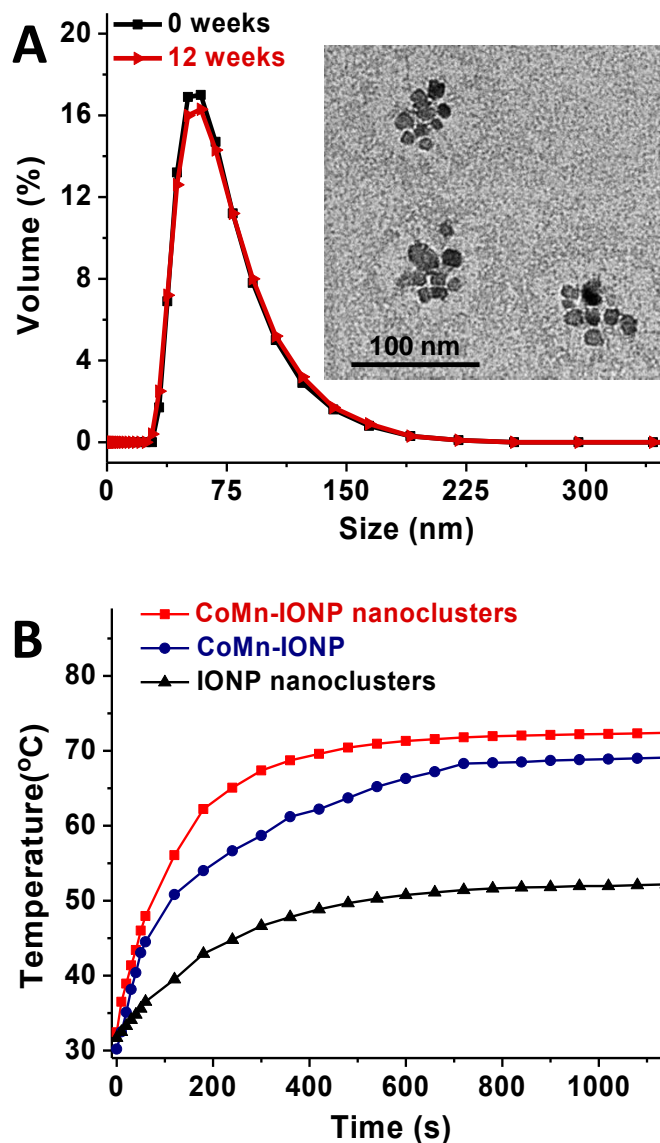


Figure 2.3: Characterization of CoMn-IONP and IONP nanoclusters.

(A) Size distribution of CoMn-IONP nanoclusters tested by DLS before and after storage for 12 weeks at room temperature. Inset: TEM image of CoMn-IONP nanoclusters. (B) Heating profiles of CoMn-IONP nanoclusters, individual CoMn-IONP and IONP nanoclusters in water (1 mg Fe /mL) subjected to AMF (420 kHz, 26.9 kA/m).

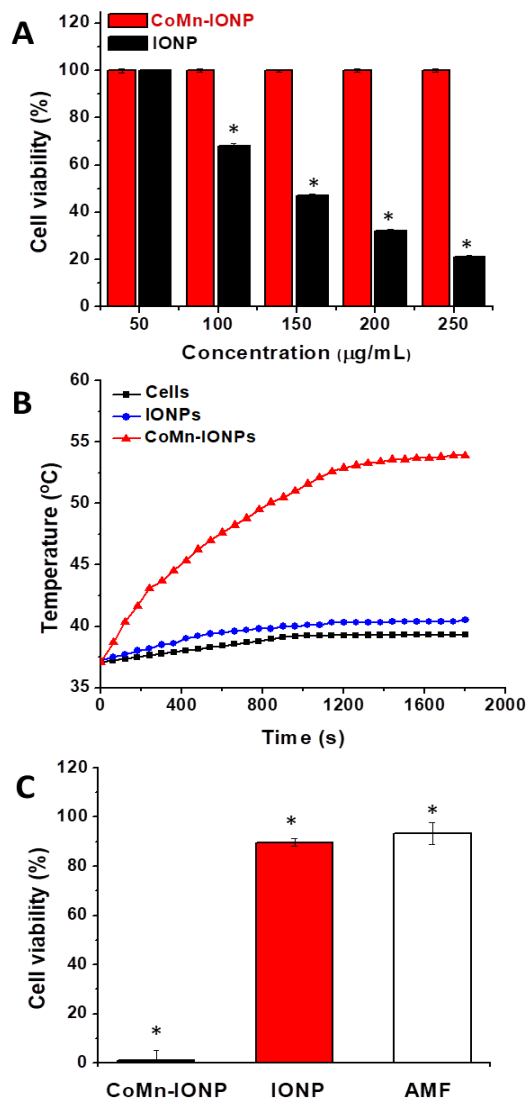


Figure 2.4: Cell viability and heating profile of CoMn-IONP and IONP nanoclusters.

(A) Viability of ES-2 cells incubated for 24 h with different concentrations of CoMn-IONP and IONP nanoclusters (50–250 μg Fe/mL). * $p < 0.05$ when compared with non-treated cells. (B) Representative heating profiles of ES-2 cells incubated with media only (cells only), CoMn-IONP and IONP nanoclusters (50 μg Fe/mL) for 24 h, and subjected to AMF (420 kHz, 26.9 kA/m). (C) The viability of ES-2 cells incubated with CoMn-IONP nanoclusters, IONP nanoclusters (50 μg Fe/mL), and medium (AMF) for 24 h and exposed to AMF (420 kHz, 26.9 kA/m) for 30 min. * $p < 0.05$ when compared with untreated cells.

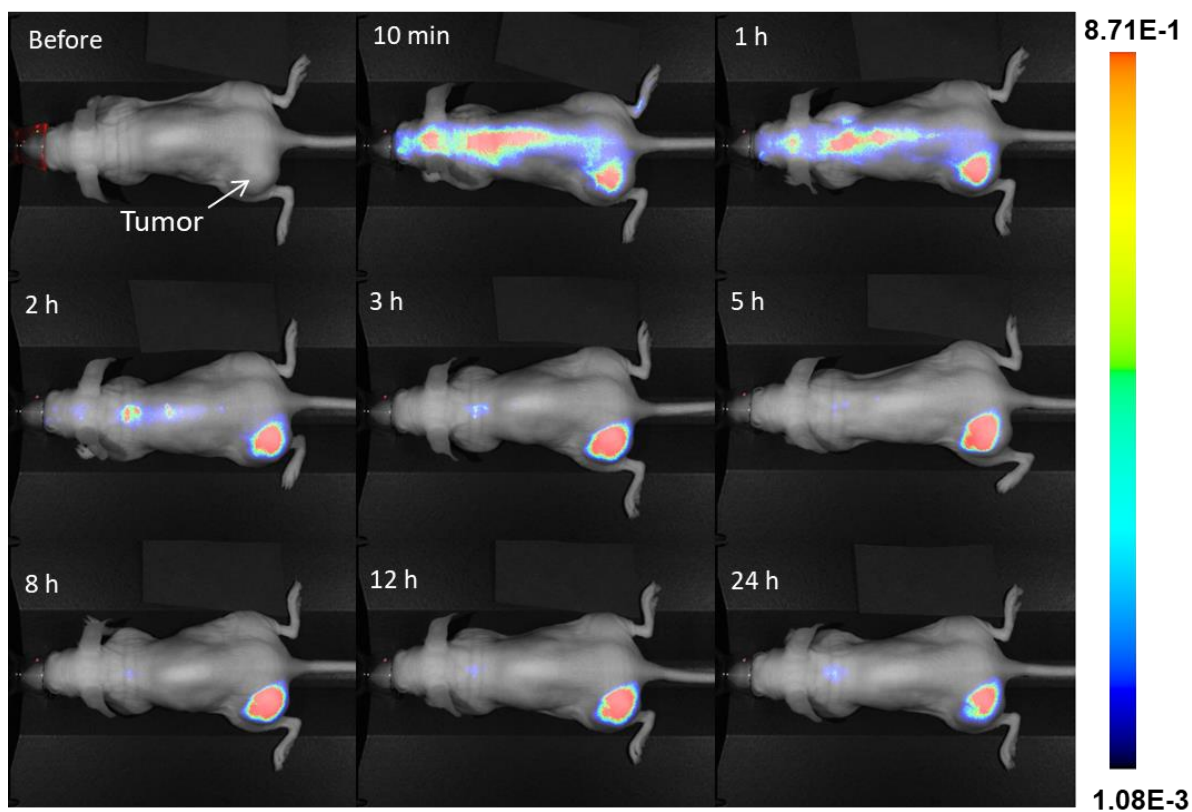


Figure 2.5: In vivo biodistribution of CoMn-IONPs.

Representative NIR fluorescence images of a live anesthetized mouse with an ES-2 subcutaneous tumor at various time points after i.v. injection of CoMn-IONP nanoclusters loaded with a hydrophobic NIR dye (silicon 2,3-naphthalocyanine bis(trihexylsilyloxy), SiNc).

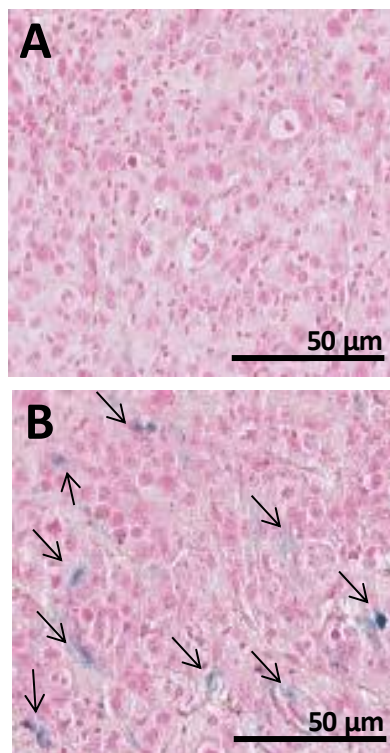


Figure 2.6: Tumor histology.

Prussian blue staining of tumor slices harvested from mice 12 h after i.v. injection with **(A)** 5% Dextrose and **(B)** CoMn-IONP nanoclusters (6 mg Fe/kg). Black arrows indicate Prussian blue staining of iron. Scale bar = 50 μm .

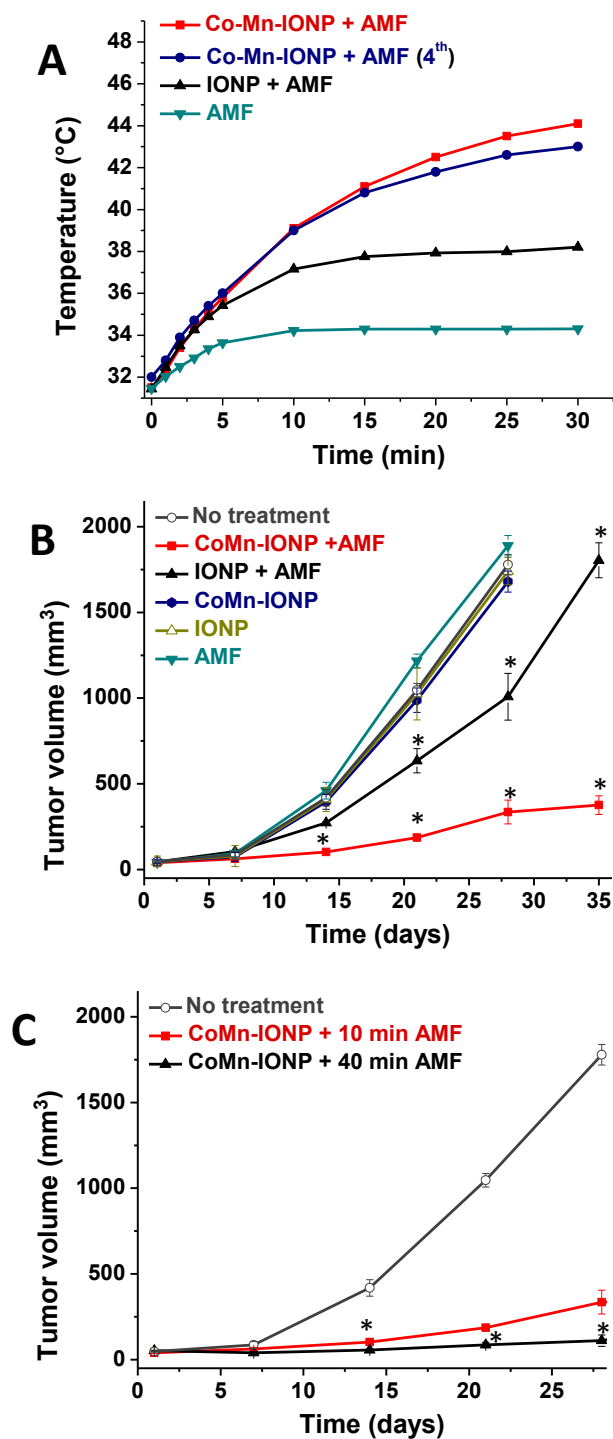


Figure 2.7: Intratumoral heating profile and tumor volume.

(A) Representative intratumoral temperature profiles during AMF (420 kHz, 26.9 kA/m) exposure of mice injected with a single dose of 5% dextrose (AMF), CoMn-IONP nanoclusters

(6 mg Fe/kg) and IONP nanoclusters (6 mg Fe/kg). The navy curve shows the intratumoral temperature during the 4th cycle in a mouse that was treated with CoMn-IONP nanoclusters (6 mg Fe/kg) and AMF once a week for 4 weeks. **(B)** Tumor growth profiles of mice with ES-2 xenografts after 4 cycles of the following treatments: (i) no treatment; (ii) CoMn-IONP + AMF, mice injected with CoMn-IONP nanoclusters (6 mg Fe/kg) and exposed to AMF for 30 min; (iii) IONP + AMF, mice injected i.v. with IONP nanoclusters (6 mg Fe/kg) and exposed to AMF for 30 min; (iv) CoMn-IONP, mice injected i.v. with CoMn-IONP nanoclusters (6 mg Fe/kg); (v) IONP, mice injected with IONP nanoclusters (6 mg Fe/kg); and (vi) AMF, mice injected with 5% dextrose and exposed to AMF. * $p < 0.05$ when compared with non-treated animals. **(C)** Tumor growth profiles of mice with ES-2 xenografts after the following treatments: (i) no treatment; (ii) CoMn-IONP + 10 min AMF, mice injected with CoMn-IONP nanoclusters (6 mg Fe/kg) and exposed to AMF for 10 min when intratumoral temperatures reached 42 °C (total exposure time to AMF 30 min) once a week during four weeks (4 cycles); (iii) CoMn-IONP + 40 min AMF, mice injected with CoMn-IONP nanoclusters (6 mg Fe/kg) and exposed once to AMF for 40 min when intratumoral temperatures reached 42 °C (total exposure time AMF 60 min). * $p < 0.05$ when compared with CoMn-IONP + 10 min AMF.

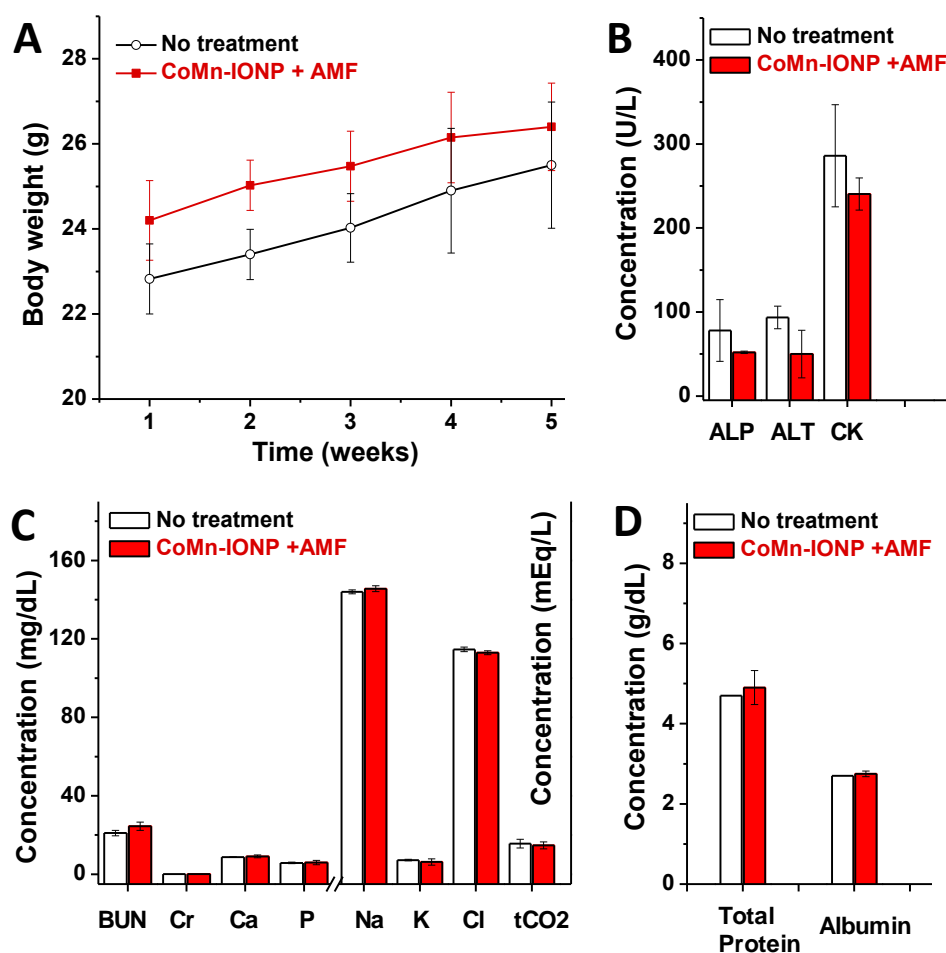


Figure 2.8: In vivo toxicity evaluation of CoMn-IONPs.

(A) Changes in body weights of untreated mice and mice treated with 4 cycles of CoMn-IONP nanocluster-mediated hyperthermia. (B-D) Blood levels of biomarkers (*alkaline phosphatase* (ALP), *aminotransferase* (ALT), *creatine kinase* (CK), *blood urea nitrogen* (BUN) and *creatinine* (Cr)), blood electrolytes, and proteins in non- and hyperthermia-treated mice.

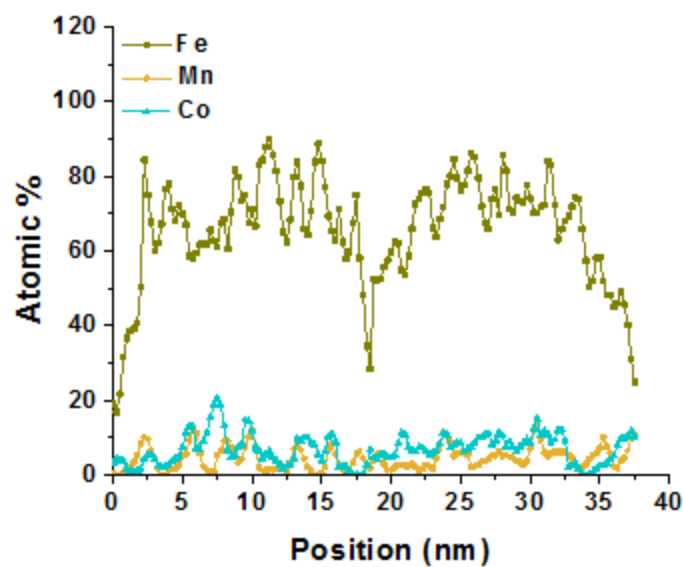


Figure 2.9: EDX line scans for metal composition of CoMn-IONPs.

Atomic percentages of iron (Fe), cobalt (Co) and manganese (Mn) in two nanoparticles (CoMn-IONP) obtained from EDX line scans.

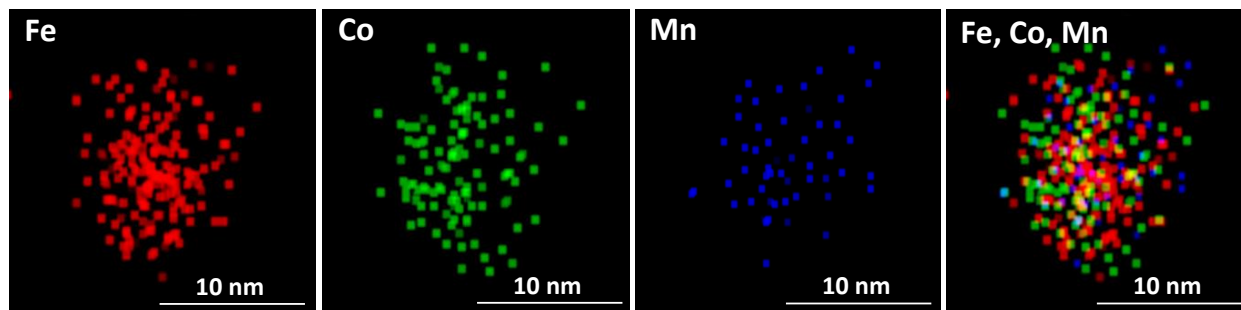


Figure 2.10: EDX elemental mappings of CoMn-IONP.

EDX elemental mappings of CoMn-IONP, revealing the distribution of Fe, Co and Mn in a single nanoparticle. Fe: iron mapped image; Co: cobalt mapped image; Mn: manganese mapped image and Fe, Co, Mn: overlay image.

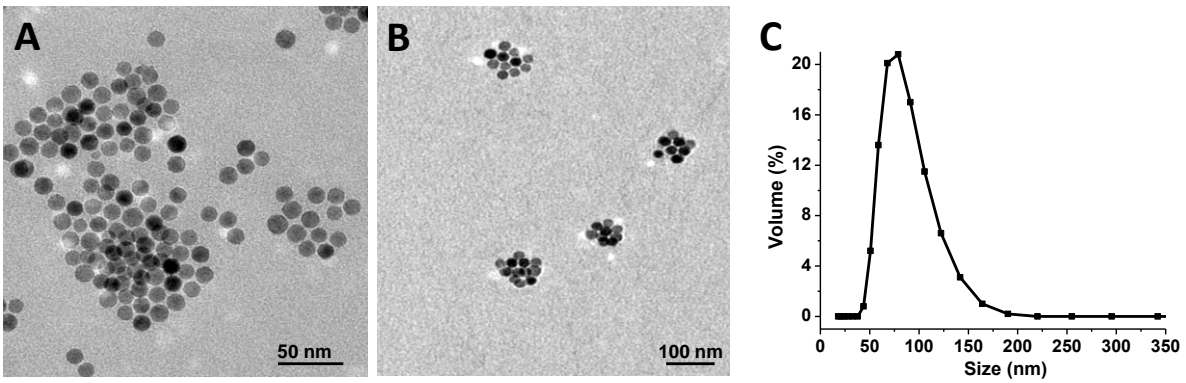


Figure 2.11: Characterization of spherical IONPs obtained from Ocean NanoTech.

Representative TEM images of (A) spherical iron oxide nanoparticles (IONP) from Ocean NanoTech and (B) corresponding IONP nanoclusters. (C) Size distribution of IONP nanoclusters tested by DLS.

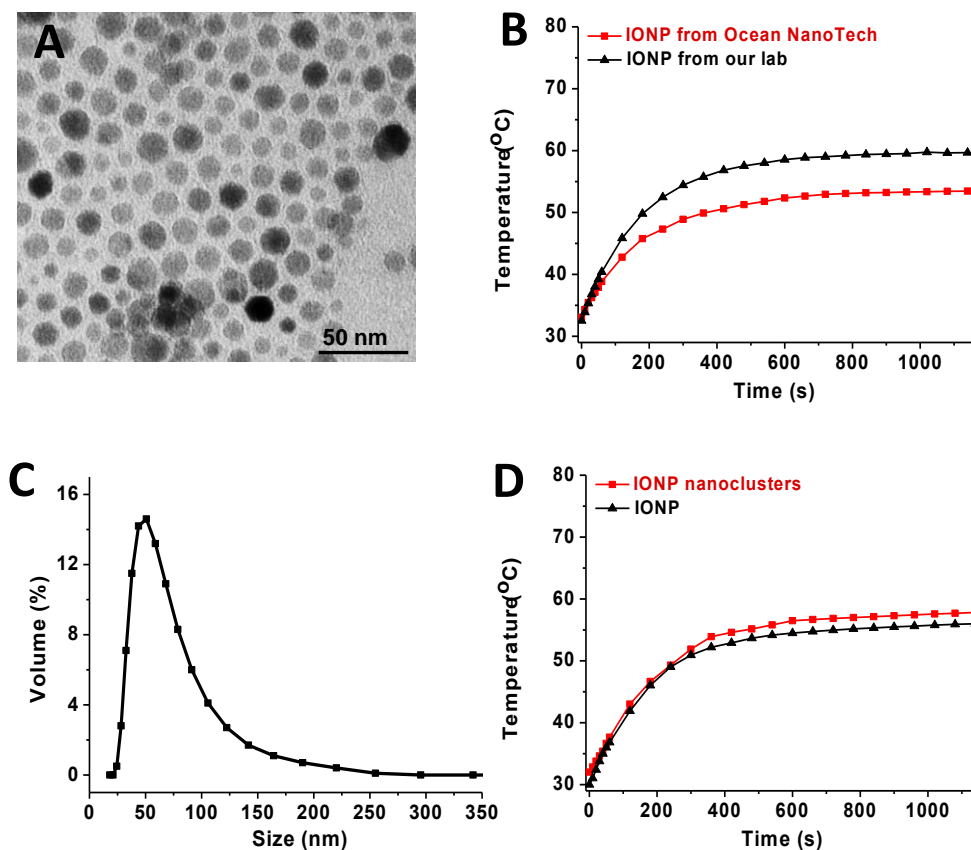


Figure 2.1: Characterization of spherical IONPs prepared in the lab.

(A) Representative TEM image of iron oxide nanoparticles (IONP) prepared in our lab and (B) Heating profiles of IONP prepared by Ocean NanoTech (red) and our lab (black). IONP were dispersed in THF (1 mg Fe /mL) and subjected to AMF (420 kHz, 26.9 kA/m). (C) DLS size distribution profile of nanoclusters of IONP prepared in our lab. (D) Heating profiles of IONP nanoclusters and individual IONP nanoparticles in water (1 mg Fe /mL) subjected to AMF (420 kHz, 26.9 kA/m).

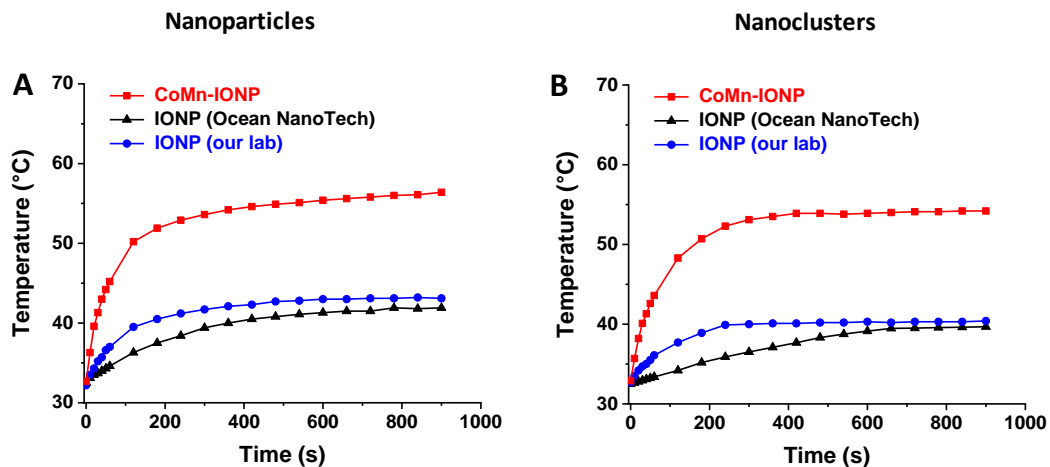


Figure 2.13: Heating profiles of magnetic nanoparticle and nanocluster in THF and 5% dextrose.

Heating profiles of (A) oleic acid-coated nanoparticles (CoMn-IONP (red), spherical IONP prepared by Ocean NanoTech (black) and IONP from our lab (blue) and (B) their corresponding nanoclusters. Oleic acid-coated nanoparticles were dispersed in THF (1 mg Fe /mL) and subjected to AMF (420 kHz, 10.6 kA/m). Nanoclusters were dispersed in 5% dextrose (1 mg Fe /mL) and subjected to AMF (420 kHz, 10.6 kA/m).

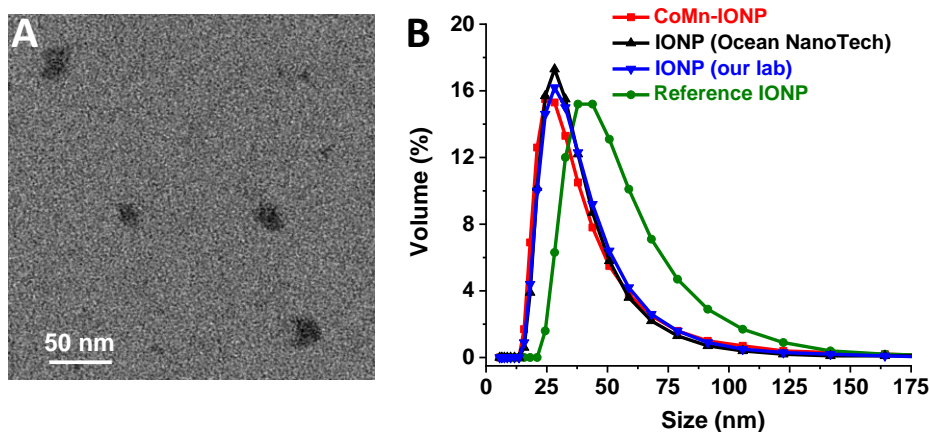


Figure 2.14: Characterization of single magnetic nanoparticles by TEM and DLS.

(A) A representative TEM image of water-dispersed individual CoMn-IONP. (B) DLS size distribution of water-dispersed individual CoMn-IONP (red), IONP from Ocean NanoTech (black) and IONP from our lab (blue). To obtain water-dispersed individual nanoparticles, oleic acid-coated CoMn-IONP (14.80 nm), IONP from Ocean NanoTech (14.91 nm) and IONP from our lab (13.97 nm) in THF were mixed with a solution of 2,3-Dimercaptosuccinic acid (DMSA) dissolved in DMSO and stirred for 24 h to allow the ligand exchange. Afterward, the particles were precipitated by centrifugation and re-dispersed in water. The green curve represents DLS size distribution of water-dispersed individual IONP (15.0 nm) with carboxylic acid groups on the surface. This reference sample was purchased from Ocean NanoTech.

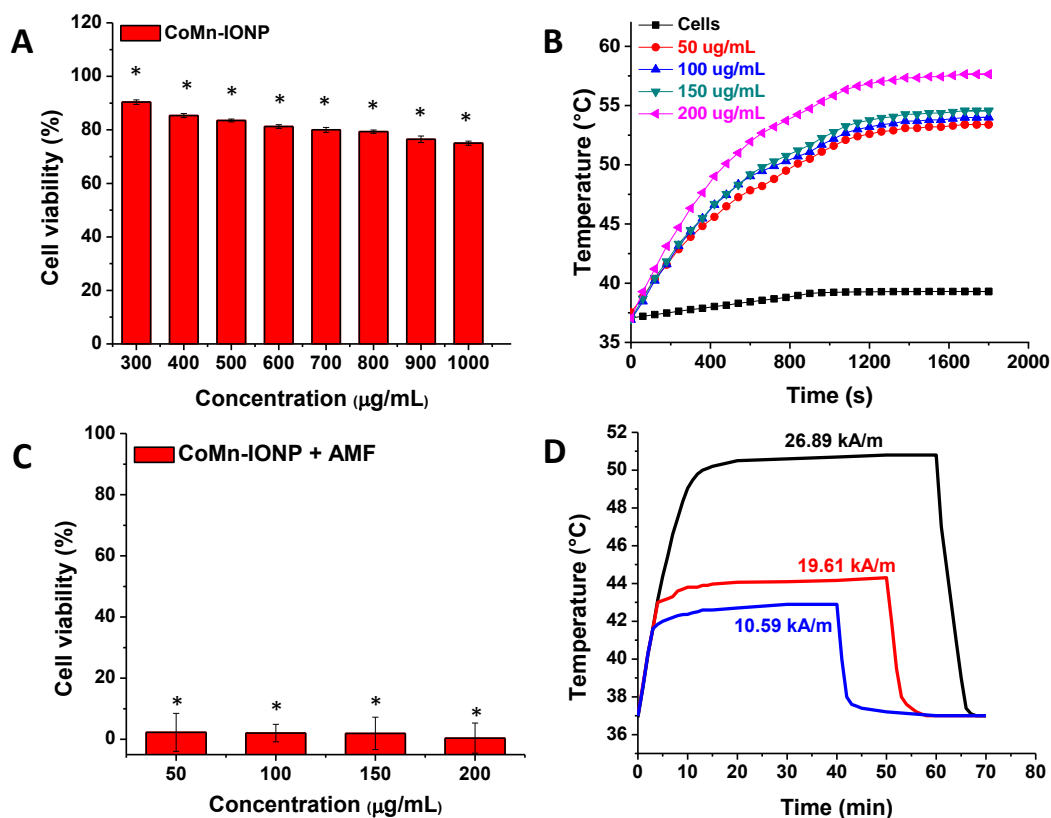


Figure 2.15: Viability of ES-2 ovarian cancer cells with various concentrations of CoMn-IONP nanoclusters

(A) Viability of ES-2 ovarian cancer cells incubated for 24 h with various concentrations of CoMn-IONP nanoclusters (300 -1000 μg Fe/mL). $*p < 0.05$ when compared with non-treated cells. (B) Heating profiles of ES-2 cells incubated with CoMn-IONP nanoclusters at various concentrations (50, 100, 150, and 200 μg Fe/mL) for 24 h and subjected to AMF (420 kHz, 26.9 kA/m). (C) Viability of ES-2 cells incubated with CoMn-IONP nanoclusters at various concentrations (50, 100, 150, and 200 μg Fe/mL) for 24 h and subjected to AMF for 30 min (420 kHz, 26.9 kA/m). $*p < 0.05$ when compared with non-treated cells. (D) Heating profiles of ES-2 cells incubated with CoMn-IONP nanoclusters (100 μg Fe/mL) for 24 h and exposed to AMF (420 kHz) with the following amplitudes: 26.89, 19.61, and 10.59 kA/m.

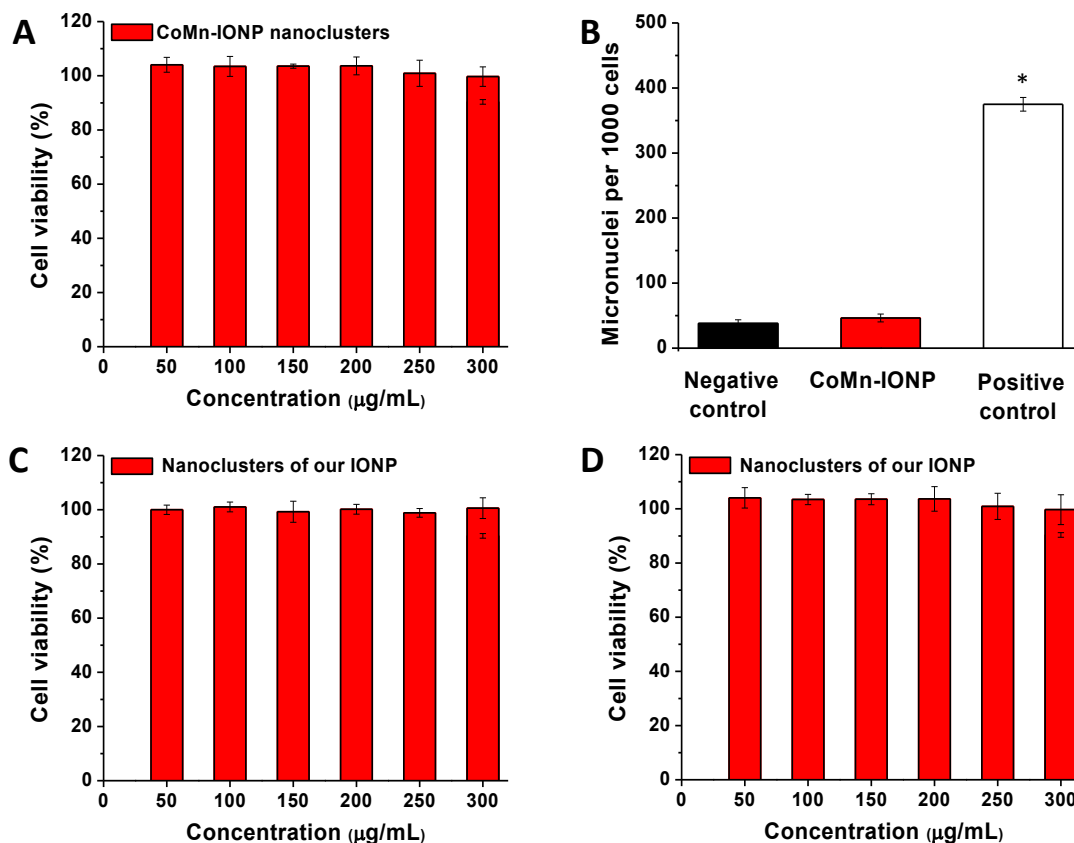


Figure 2.16: Viability of human embryonic kidney cells (HEK-293) incubated for 24 h with different concentrations of CoMn-IONP and IONP nanoclusters.

(A) Viability of human embryonic kidney cells (HEK-293) incubated for 24 h with different concentrations of CoMn-IONP nanoclusters (50–300 µg Fe/mL). (B) An *in vitro* micronucleus assay (formation of micronuclei) was used to determine the genotoxicity of CoMn-IONPs. Chinese hamster ovary (CHO-K1) cells were treated with CoMn-IONP nanoclusters (200 µg Fe/mL) for the experiment group, fresh media for negative control, or ethyl methanesulfonate (EMS, 400 µg/mL) for a positive control. * $p < 0.05$ when compared with negative control. Viability of ES-2 (C) and HEK-293 (D) cells incubated for 24 h with different concentrations of nanoclusters prepared from IONP synthesized in our lab (50–300 µg Fe/mL).

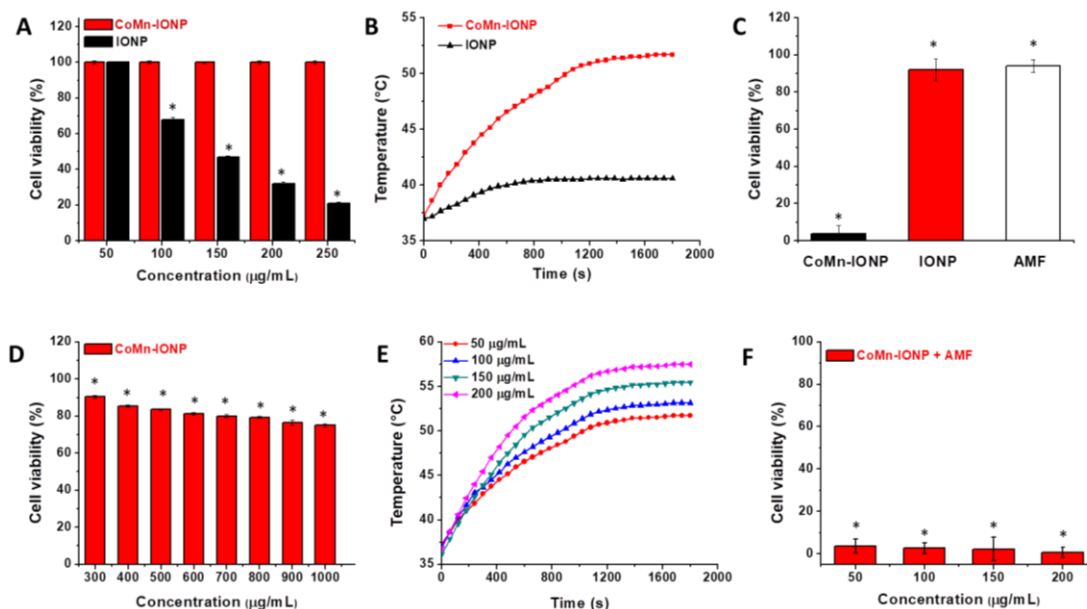


Figure 2.17: Viability of A2780/CDDP human ovarian carcinoma cells with various concentrations of CoMn-IONP and IONP nanoclusters.

(A) Viability of A2780/CDDP human ovarian carcinoma cells incubated for 24 h with various concentrations of CoMn-IONP and IONP nanoclusters (50 -250 Fe μg /mL). * $p < 0.05$ when compared with non-treated cells. (B) Heating profiles of A2780/CDDP cells incubated with CoMn-IONP and IONP nanoclusters (50 μg Fe/mL) for 24 h and subjected to AMF at magnetic field frequency of 420 kHz and amplitude of 26.9 kA/m. (C) Viability of A2780/CDDP cells incubated with CoMn-IONP and IONP nanoclusters (50 μg Fe/mL) and media (AMF) for 24 h and exposed to AMF (420 kHz, 26.9 kA/m) for 30 min. * $p < 0.05$ when compared with non-treated cells. (D) Viability of A2780/CDDP ovarian cancer cells incubated for 24 h with various concentrations of CoMn-IONP nanoclusters (300 -1000 Fe μg/mL). (E) Heating profiles of A2780/CDDP cells incubated with CoMn-IONP nanoclusters at various concentrations (50, 100, 150, and 200 μg Fe/mL) for 24 h and subjected to AMF (420 kHz, 26.9 kA/m). (F) Viability of A2780/CDDP cells incubated with CoMn-IONP nanoclusters at various concentrations (50, 100, 150, and 200 μg Fe/mL) for 24 h and subjected to AMF for 30 min (420 kHz, 26.9 kA/m). * $p < 0.05$ when compared with non-treated cells.

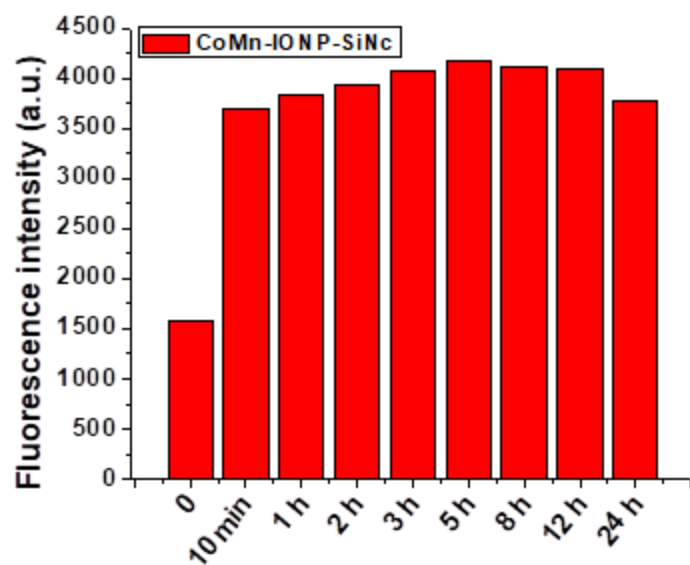


Figure 2.18: The NIR fluorescence intensity of CoMn-IONPs in tumor for 24 h.

The NIR fluorescence intensity measured in the tumor as a function of time after intravenous injection of SiNc-CoMn-IONP in a mouse bearing ES2 tumor.

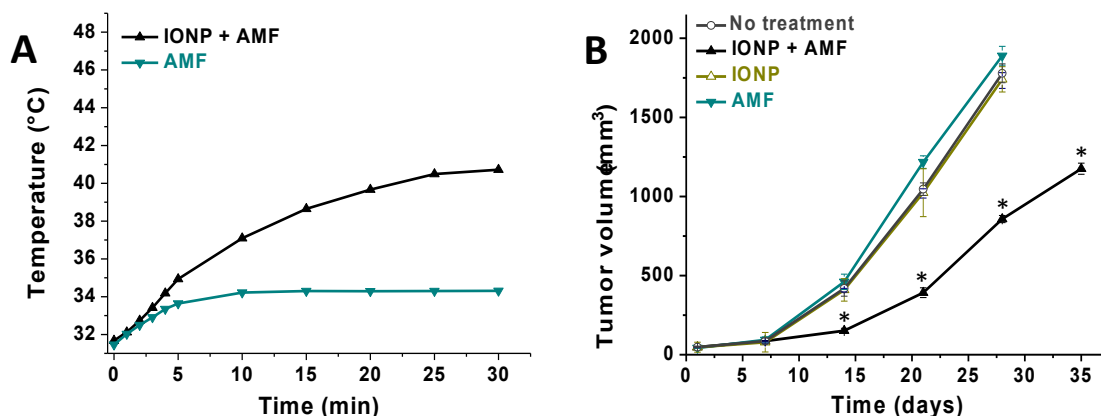


Figure 2.19: Intratumoral heating profile and tumor volume of IONPs prepared in our lab.

(A) Representative intratumoral temperature profiles during AMF (420 kHz, 26.9 kA/m) exposure of mice injected with a single dose of 5% dextrose (AMF), and nanoclusters of IONP prepared in our lab (6 mg Fe/kg). (B) Tumor growth profiles of mice with ES-2 xenografts after 4 cycles of the following treatments: (i) no treatment; (ii) IONP + AMF, mice injected i.v. with nanoclusters of IONP prepared in our lab (6 mg Fe/kg) and exposed to AMF for 10 min when intratumoral temperatures reached 42 °C (total exposure time 30 min); (iii) IONP, mice injected with nanoclusters of spherical IONP prepared in our lab (6 mg Fe/kg); and (iv) AMF, mice injected with 5% dextrose and exposed to AMF. * $p < 0.05$ when compared with non-treated animals.

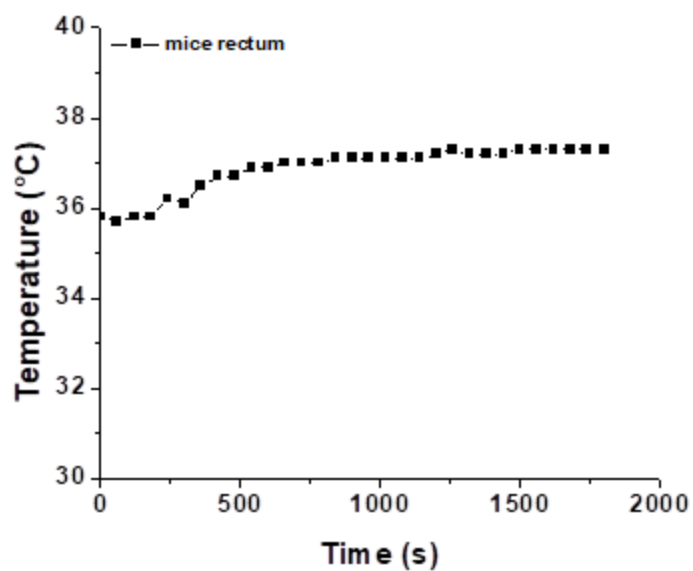


Figure 2.20: Mice rectal temperature profile.

Representative rectal temperature profile during AMF (420 kHz, 26.9 kA/m) exposure of a mouse injected with a single dose of 5% dextrose.

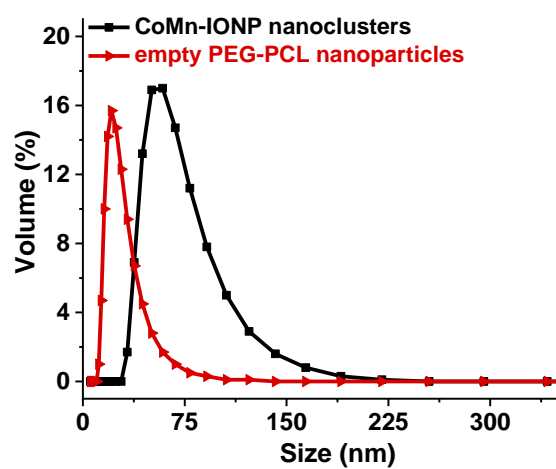


Figure 2.21: Size distribution of CoMn-IONP nanoclusters and empty PEG-PCL nanoparticles tested by DLS.

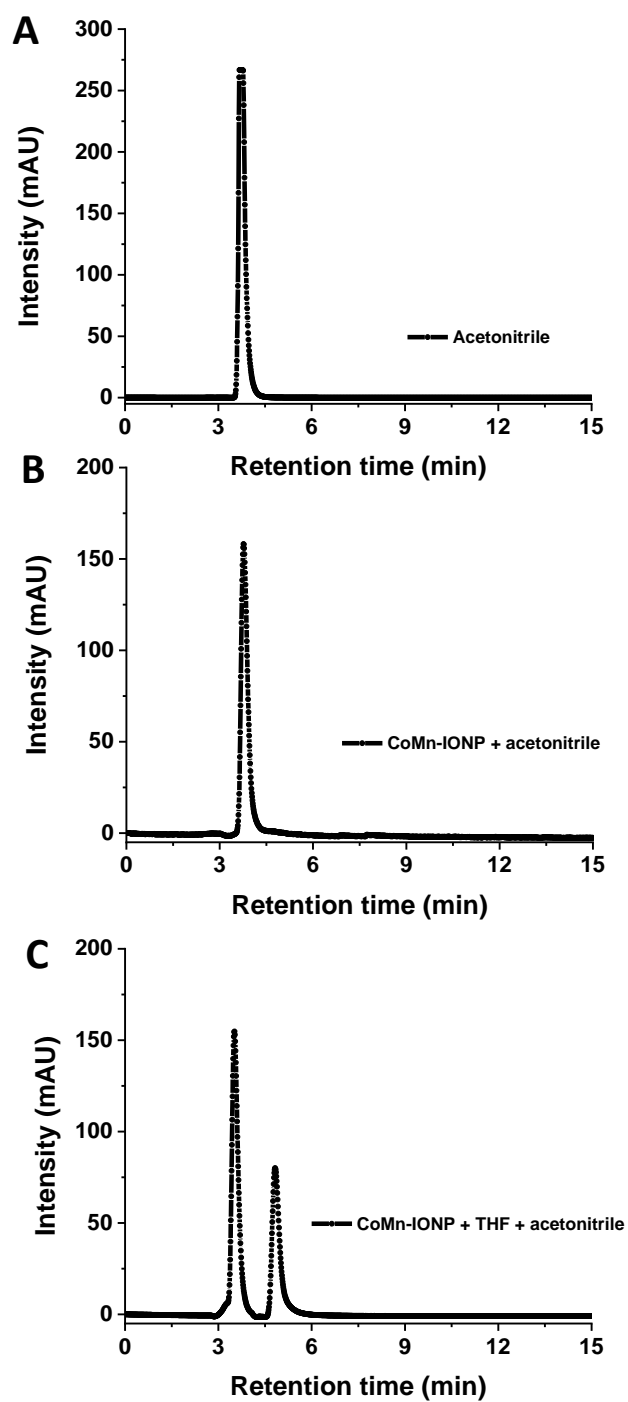


Figure 2.22. Detection of tetrahydrofuran by reversed-phase high-performance liquid chromatography (RP-HPLC):

HPLC spectra for (A) Acetonitrile, (B) aqueous solution of CoMn-IONP nanoclusters diluted in acetonitrile, and (C) 5 μ L Tetrahydrofuran (THF) was added to 995 μ L aqueous solution of CoMn-IONP nanoclusters diluted in acetonitrile.

CHAPTER 3

Zinc and Manganese-Doped Iron Oxide Nanoclusters for Systemically Delivered Magnetic Hyperthermia

Hassan A. Albarqi, Fahad Y. Sabei, Abraham S. Moses, Mikkel N. Hansen, Pallavi

Dhagat, Olena Taratula and Oleh Taratula

3.1 ABSTRACT

An effective systemically delivered magnetic hyperthermia is a significant challenge. To address this, we have previously developed and reported magnetic nanoclusters consisting of hexagonal-shaped, iron oxide nanoheaters doped with cobalt (8.1%) and manganese (5.3%). Although our data confirmed that cobalt ions do not leach from the developed nanoclusters and that they are non-toxic, we understand that concerns associated with potential toxicity of cobalt-containing nanoclusters could limit their clinical translational potential. Therefore, we have developed cobalt-free nanoclusters for systemically delivered magnetic hyperthermia. The developed nanoclusters consist of zinc and manganese-doped iron oxide nanoparticles (ZnMn-IONPs) encapsulated in PEG-PCL-based drug delivery system. Animal studies validated that, following intravenous injection, the developed nanoclusters (ZnMn-IONCs) efficiently accumulate in the cancer tumor and elevate the intratumoral temperature to 42 °C upon exposure to AMF (420 kHz, 26.9 kA/m). Magnetic hyperthermia mediated by these ZnMn-IONCs substantially inhibited tumor growth and did not exhibit any signs of toxicity.

Keywords: magnetic hyperthermia, magnetic nanoparticles, nanoclusters, systemic delivery

3.2 INTRODUCTION

Magnetic fluid hyperthermia (MFH) is a powerful technique to treat malignant tumors with minimal side effects on surrounding healthy tissue.^{1, 2} MFH can achieve local hyperthermia by using magnetic nanoparticles (MNPs) that generate heat upon exposure to an alternating magnetic field (AMF).^{3, 4} Magnetic metal ferrite nanoparticles ($M\text{-Fe}_2\text{O}_4$ where $M = \text{Fe, Mn, Zn, Ni, Co, Mg}$ etc) are the most promising candidates and have important characteristics that make them attractive for MFH. Magnetic metal ferrite nanoparticles are tunable, chemically stable, and biocompatible.⁵ However, despite its promising magnetic properties, low specific absorption rate (SAR) is still a significant challenge to be overcome in translating MFH to a clinical application.^{2, 6, 7} Thus, there is a critical need to develop new types of nanoparticles that have high SAR at low dosage.

It has been reported that SAR can be improved by tuning characteristics of the magnetic nanoparticle structure such as size, shape, and metal composition.^{5, 8} In this regard, metal-doped magnetic ferrite nanoparticles have been explored in attempts to develop highly efficient nanoheaters for magnetic hyperthermia.^{9, 10} A recent report revealed that zinc doped cubical iron oxide nanoparticle has SAR value (1019.2 W/g at $f = 380$ kHz, $H = 16$ kA/m) that is 2.8 times higher than non-doped cubical iron oxide nanoparticles.¹¹ Another study suggested that $\text{Mg}_{0.13}\gamma\text{-Fe}_2\text{O}_3$ superparamagnetic nanoparticles have SAR value 100 times higher than commercially available iron oxide nanoparticles.¹² Therefore, incorporation of metal dopant into magnetic ferrite nanoparticles can tune their magnetic properties and finally enhance their heating efficiency.

In our previous work, we were able to synthesize biocompatible nanoclusters consisting of hexagon-shaped cobalt and manganese-doped iron oxide nanoparticles (CoMn-IONPs) loaded

into PEG-PCL (poly(ethylene glycol)-*b*-poly(ϵ -caprolactone) polymers. These CoMn-IONP nanoclusters have a SAR value (1237.0 W/g) 3.2 times larger than commercially available IONPs (390.4 W/g) and they were able to increase the intratumoral temperature above 42 °C after a single intravenous injection at a clinically relevant dose. We determined that CoMn-IONP nanoclusters are not genotoxic and mice did not display any signs of toxicity 35 days after treatment with these nanoclusters. We also validated that negligible leaching of Co (<0.03%) from the nanoclusters was detected after incubation in serum at 37 °C for 7 days.¹³ Furthermore, a clinical trial with people who voluntarily ingested a cobalt supplement (0.080-0.19 mg Co/kg x day) over a 3-month period revealed no side effects.¹⁴ Nevertheless, we realize that CoMn-IONP nanoclusters might have limited translational potential due to theoretical concerns of Co leaching from the nanoclusters resulting in toxicity. Therefore, we have developed and evaluated cobalt-free nanoclusters doped with Zn and Mn (ZnMn-IONP) that possess a heating efficiency similar to that of nanoclusters made with cobalt, but without the putative toxicity. Among metal dopants, manganese (Mn) and zinc (Zn) are considered to be the safest magnetic metals to which the human body can be exposed at low dosage, and the softest ferrite materials, which have higher saturation magnetization to enhance the heating efficiency of nanoparticles.¹⁵

3.3 MATERIALS AND METHODS

3.3.1 Materials

Iron (III) acetylacetonate ((Fe(acac)₃) was purchased from Acros Organics (Fair Lawn, NJ). Zinc chloride anhydrous (ZnCl₂) and Oleylamine were purchased from Sigma-Aldrich (St. Louis, MO). Oleic acid, manganese (II) chloride tetrahydrate (MnCl₂·4H₂O) was obtained from Alfa Aesar (Ward Hill, MA). n-Octyl ether was purchased from Tokyo chemical industry Co. (Tokyo, Japan). m-PEG-PCL (methoxy poly(ethylene glycol)-*b*-poly(ϵ -caprolactone), MW: 5k-10k) was

obtained from Advanced Polymer Materials Inc. (Montreal, Canada). SiNc (silicon 2,3-naphthalocyanine bis(trihexylsilyloxy)) was purchased from Sigma-Aldrich (Milwaukee, WI). All other chemicals and supplies were obtained from VWR International (Radnor, PA).

3.3.2 Methods

3.3.2.1 Synthesis of zinc- and manganese-doped iron oxide nanoparticles

Iron oxide nanoparticles doped with Zinc and manganese (ZnMn-IONP) were synthesized according to our recently published protocol with some modification.^{13, 16, 17} Zinc chloride hexahydrate (ZnCl_2 , 2 mmol), manganese chloride ($\text{MnCl}_2 \cdot 4\text{H}_2\text{O}$, 3 mmol), and iron (III) acetylacetonate ($\text{Fe}(\text{acac})_3$, 5.00 mmol) were placed in a 250 mL three-neck round-bottom flask containing oleic acid (6 mmol), oleylamine (6 mmol) and n-octyl ether (25 mL). The obtained mixture was heated to 300 °C and stirred under nitrogen flow. After 1 h at 300 °C, the black mixture was precipitated and washed three times with ethanol (30 mL), followed by centrifugation at 7000 rpm for 30 min. The obtained precipitate was re-dispersed in hexane (10 mL). The obtained ZnMn-IONPs were dried at 70 °C for 12 h.

3.3.2.2 Nanoparticle characterization

The surface morphology and particle size of ZnMn-IONPs were examined using a FEI Tecnai™ Spirit transmission electron microscopy (TEM) system. To characterize the chemical composition structure of nanoparticles, a FEI 80-300 kV Titan (S) TEM equipped with a spherical aberration image corrector was used. The elements composition was analyzed by energy dispersive x-ray spectroscopy (EDX). EDX analysis was employed to confirm the presence and the location of elements (Fe, Zn, Mn) in a single nanoparticle. The saturation magnetization measurement was performed using a vibrating sample magnetometer at room

temperature to investigate the saturation magnetization of the nanoparticle.^{13, 18} The heating efficiency of nanoparticles was tested in the presence of an alternating magnetic field generated by an induction heating system (MSI Automation, Wichita, KS), and the corresponding specific absorption rates (SAR) were calculated according to previously reported procedures.^{13, 18}

3.3.2.3 ZnMn- IONCs preparation

Solvent evaporation method was used to prepare ZnMn-IONCs.^{13, 19, 20} Briefly, ZnMn-IONPs (8 mg/mL THF) and PEG–PCL (10 mg/mL THF) were mixed for 20 minutes. Then, 5% dextrose solution in water (6 mL) was added to the reaction mixture and mixed for 20 minutes. THF was then removed by rotovap. The ZnMn-IONCs were separated from the excess of empty PEG-PCL nanoparticles using a strong magnet (SuperMag Separator, Ocean NanoTech). The obtained ZnMn-IONCs were re-dispersed in 5% dextrose, filtered through a 0.2 µm filter to remove any possible aggregate, and analyzed in terms of loading, size, and charge, and were stored at 4 C°.

3.3.2.4 Chemical composition analysis

ZnMn-IONPs were dispersed in Hexane 50:1 by weight and sonicated for 15 minutes. 2 µL of the sample was then dispensed onto a plasma cleaned Holey Carbon grid, Ted Pella 01824. The grids were then dried in a 60 °C oven overnight and then analyzed in a G2 Titan at 200 keV in STEM mode. Probe current was 0.1nA, spot 6, CA 100. Drift controlled hypermaps were acquired with four Bruker SDD detectors located every 90 degrees to eliminate shadows in the maps. Hypermaps were post-processed using an interactive Cliff Lorimer method in Bruker Esprit 1.9 with Copper deconvolved.

3.3.2.5 Synthesis of SiNc-loaded ZnMn-IONCs

The SiNc-loaded ZnMn-IONCs were prepared by following our previously published protocol.^{13,}

^{19, 20} Briefly, ZnMn-IONPs (8 mg_{Fe}/mL THF) and PEG–PCL (10 mg/mL THF) were mixed for

10 minutes. Then, silicon naphthalocyanine (SiNc, 0.3 mg/mL THF) was added to the mixture, followed by stirring for 10 minutes. Then, 5% dextrose solution in water (6 mL) was added to the reaction mixture and mixed for 20 minutes. THF was evaporated under vacuum. The obtained SiNc-loaded ZnMn-IONCs were filtered through a 0.2 μm filter to remove any possible aggregate.

3.3.2.6 Nanoclusters characterization

The hydrodynamic diameter, zeta potential, and polydispersity index (PDI) of the prepared ZnMn-IONCs were determined by dynamic light scattering (DLS, ZetaSizer NanoSeries, Malvern, UK).^{13, 19, 20} Transmission electron microscopy (TEM) was used to determine the surface morphology and particle size of the nanoclusters. The iron content in the obtained nanoclusters was determined using a colorimetric ferrozine-based assay according to our previously reported procedure.^{13, 18} The heating efficiency of the obtained nanoclusters in the presence of AMF was measured as described above.

3.3.2.7 *In vitro* studies

DU145 human prostate carcinoma cell lines and human embryonic kidney cells (HEK-293) were purchased from Developmental Therapeutics Core (Northwestern University, IL) and ATCC (Manassas, VA) and cultured in RPMI 1640 medium supplemented with fetal bovine serum (10%) and penicillin-streptomycin (1%). Cytotoxicity was assessed on DU145 cells and HEK 293 in the presence of 50-200 $\mu\text{g}_{\text{Fe}}/\text{mL}$ concentrations of different nanoclusters. Cells were seeded in a 96-well plate at a density of 1×10^4 cells/well and incubated in RPMI for 24 h. The media was replaced with fresh media containing either IONCs or ZnMn-IONCs and incubated for 24 h. Afterward, the cells were rinsed with DPBS three times. Then, a modified Calcein AM assay was used to evaluate cell viability according to a previously published protocol.²¹

For cellular internalization, DU145 cancer cells (1×10^5 cells/ well) were plated in 6-well plates followed by 24 h incubation with SiNc-ZnMn-IONCs ($50 \mu\text{g}_{\text{Fe}}/\text{mL}$). Cells were washed with DPBS three times and imaged with an EVOS FL Cell Imaging System.

To evaluate the heating efficiency of nanoclusters *in vitro*, we followed our previously published protocol.^{13, 18} Briefly, cells incubated with $50 \mu\text{g}_{\text{Fe}}/\text{mL}$ non-toxic concentration of ZnMn-IONCs and IONCs for 24 h, cancer cells were washed three times with DPBS, detached with 0.25% trypsin/EDTA and resuspended in cell culture media prior to counting. 5×10^6 cells were suspended in a constant volume of 0.1 mL of cell culture media in a 0.5 mL microcentrifuge tube. The samples were then positioned in the center of a 6-turn copper coil (inner diameter: 40 mm) and exposed to AMF (420 kHz, 26.9 kA/m) for 30 min. The temperature changes were measured by placing a fiber optic probe (Neoptix Inc., QC, Canada) inside the cell pellets. The water jacket inside the coil was maintained at $\sim 37^\circ\text{C}$, and the samples were allowed to equilibrate to this temperature before exposure to AMF. Controls were carried out with non-treated cells exposed to AMF alone and with cells exposed to no field. Then, the cells were resuspended in media and seeded in 96-well plates at a density of 10×10^3 cells/well and cultured for an additional 48 h to evaluate the anticancer effect of nanocluster-mediated magnetic hyperthermia. Finally, cell viability was assessed using a Calcein AM assay.

3.3.2.8 *In vivo* studies:

All animal studies were conducted under a protocol approved by the Institutional Animal Care and Use Committee of Oregon State University and Oregon Health and Science University.

3.3.2.9 Development of a subcutaneous xenograft mouse model of human prostate cancer

3×10^6 DU145 cells suspended in Matrigel were injected subcutaneously into the right flank of 4-6 week-old female mice purchased from Charles River Laboratories (Wilmington, MA, USA).

The tumor was measured by a caliper every other day, and its volume was calculated. The tumors were treated when they reached 50 mm³. The tumor volume was recorded with a digital caliper (VWR Int.) and was calculated as width² × length × 0.5.

3.3.2.10 Evaluation of nanoclusters biodistribution

Five mice bearing subcutaneous xenografts of DU145 prostate cancer cells were injected *via* tail vein with ZnMn-IONCs at a dose of 10 mg_{Fe}/kg. The distribution of nanoclusters in the mouse body after injection was monitored using the Pearl® Impulse Small Animal Imaging System at various time points after injection to visualize tissue distribution of the nanoclusters. For this purpose, nanoclusters were loaded with the near-infrared (NIR) fluorescent dye SiNc. Afterward, the tumor and major organs of injected mice were harvested for *ex vivo* imaging after 18 h. White light and fluorescence images for each mouse were recorded and overlaid by the imaging system.

3.3.2.11 Evaluation of the therapeutic efficiency of nanoclusters-mediated hyperthermia

Experiments were performed on nude mice bearing subcutaneous DU145 xenografts as previously described.¹³ When tumor volume became ~50 mm³, Mice were randomly divided into six groups (five mice per group) : (1) No treatment (5% dextrose), (2) AMF (5% dextrose), (3) IONCs, (4) IONCs + AMF, (5) ZnMn-IONCs, and (6) ZnMn-IONCs + AMF. To evaluate the therapeutic efficacy of magnetic hyperthermia mediated by the developed nanoclusters, mice were injected intravenously (*i.v.*) with nanoclusters at a dose of 10 mg_{Fe}/kg. At 18 h post-injection, mice in group 2,4, and 6 were exposed to AMF (420 kHz, 26.9 kA/m) for 30 minutes. The intratumoral temperature was measured by a fiber optic temperature probe that was inserted into the center of the tumor following our previously reported procedure.²² Each group was

treated once per week for 4 weeks with appropriate formulations. The tumor size in each group was measured every seven days for 5 weeks.

3.3.2.12 Statistical analysis

The data were analyzed using descriptive statistics and presented as mean value \pm standard deviation (SD) from 3-5 separate measurements. Comparisons among groups were executed using independent samples Student's t-tests. Differences between groups were considered statistically significant at $p < 0.05$.

3.4 RESULTS AND DISCUSSION

The main problem currently associated with systemically delivered magnetic hyperthermia is that the amount of magnetic nanoparticles delivered to the tumor tissue after systemic administration is insufficient to reach an intratumoral temperature above 40 °C^{23, 24}. To overcome the limitation of conventional IONP, we synthesized oleic acid-coated iron oxide nanoparticles doped with zinc and manganese (ZnMn-IONPs, Figure 3.1). Magnetic soft materials (Fe, Mn, Zn) suitable for magnetic hyperthermia because of high saturation magnetization.^{5, 25} ZnMn-IONPs have good physical properties to work as magnetic hyperthermia agents such as suitable magnetocrystalline anisotropy, high saturation magnetization, and excellent chemical stability.^{26, 27} ZnMn-IONPs were prepared using a thermal decomposition method where Zn and Mn were combined to produce nanoparticles with uniformly distributed elements.^{13, 16, 28} ZnMn-IONPs were coated with hydrophobic surfactants, oleic acid and oleylamine, for stabilization and aggregation prevention. The average size of synthesized ZnMn-IONPs is 13.32 ± 4.11 nm confirmed by transmission electron microscopy (TEM) (Figure 3.2A). ZnMn-IONPs chemical composition was evaluated by energy dispersive

x-ray spectroscopy (EDX) mapping analysis. Figure 3.2B demonstrates that Zn, Mn and Fe elements distributed throughout the nanoparticle. The synthesized nanoparticles were composed of $92.63\% \pm 9.11$ of Fe, $4.07\% \pm 0.89$ of Mn, $3.3\% \pm 0.98$ of Zn, as revealed by EDX analysis (Figure 3.2B).

To determine the improvement in magnetic properties and heating efficiency of ZnMn-IONPs, oleic acid-coated IONP (without Zn and Mn) with an average diameter of 13.97 ± 3.63 nm were prepared under identical conditions and were used as a reference for comparison. IONPs were synthesized in our lab as previously reported.¹³ The saturation magnetization (M_s) of ZnMn-IONPs is $(60.33 \text{ Am}^2/\text{kg})(60.33 \text{ emu/g})$ and almost has zero coercivity, showed that the sample has superparamagnetic properties at the room temperature. ZnMn-IONPs showed higher M_s compared to IONPs reached up to $57 \text{ Am}^2/\text{kg}$ (57 emu/g) (Figure 3.2C). This result reveals the improvement in magnetism of ZnMn-IONPs which is an important factor in magnetic hyperthermia due to the fact that the heating ability of magnetic nanoparticles is dependent on saturation magnetization. Furthermore, ZnMn-IONPs have a significantly higher SAR value (1615.1 W/g) than IONP (586.2 W/g) at the same Fe concentration (1 mg/mL) (Figure 3.2D).

To provide surface protection and water solubility for intravenous delivery, we encapsulated hydrophobic ZnMn-IONPs into polyethylene glycol-block-poly (ϵ -caprolactone) (PEG-PCL) following the method previously reported by our group (Figure. 3.1).^{13, 19, 20} PEG-PCL possesses attractive features including high drug-loading efficiency, easy surface modification, biocompatibility, biodegradability, and low toxicity. The benefit of using PEG-PCL is that it does not interfere with the magnetic properties of our magnetic nanoparticles, while being able to load clusters of ZnMn-IONPs, stabilize them in biological fluids, and neutralize the negative surface charge to prolong blood circulation.^{13, 19, 20} The average hydrodynamic size of the

developed nanoclusters (ZnMn-IONCs) is 109.4 ± 0.65 nm and zeta potential is -1.96 ± 0.43 mV (Figure 3.3A). TEM imaging of ZnMn-IONCs confirms the formation of nanoclusters (Figure 3.3A, inset).

The effect on the SAR of transforming hydrophobic ZnMn-IONPs into the water-soluble platform was investigated (Figure 3.3B). The heating efficiency of ZnMn-IONP nanoclusters (ZnMn-IONCs) was significantly higher than IONP nanoclusters (IONCs) upon exposure to AMF ($f = 420$ kHz; $H = 26.9$ kA/m). As shown in Figure 3.3B, ZnMn-IONCs rapidly increased the solution temperature above 50 °C, while the solution temperature of IONCs was 10 degrees less at the same conditions. The calculated SAR of ZnMn-IONCs is 1010 W/g in aqueous solution and is ~2 times higher than the SAR of IONCs (493.83 W/g).

3.4.1 *In vitro* characterization of ZnMn-IONCs

The DU145 prostate cancer cells were incubated with a concentration range of 50-250 $\mu\text{g/mL}$ of nanoclusters. The *in vitro* results revealed that ZnMn-IONCs and IONCs are not toxic at concentrations up to 250 $\mu\text{g/mL}$ (Figure 3.4A). It was also validated that ZnMn-IONCs and IONCs are not toxic to non-malignant, human embryonic kidney cells (HEK-293) at iron concentrations up to 250 $\mu\text{g/mL}$ (Figure 3.4B).

To investigate the cellular internalization of nanoclusters in DU145 cells, the cells were incubated with SiNc-loaded ZnMn-IONCs for 24 h (Figure 3.4C,D,E). It was verified that the SiNc-loaded ZnMn-IONCs were located in the cytoplasm (red) with lower accumulation in the nucleus (blue).

To assess anticancer effect and heat generation of both ZnMn-IONCs and IONCs, DU145 cells were incubated with nanoclusters at concentration of 50 $\mu\text{g/mL}$ for 24 h. Next cell pellets (5 X

10^6 cells) in 100 μ L of cell culture media were exposed to AMF ($f = 420$ kHz, $H = 26.9$ kA/m) for 30 minutes. The temperature of ZnMn-IONCs reached 50 °C in 15 minutes and remained constant during the treatment (Figure 3.5A). In the case of IONCs, the intracellular temperature did not rise above 44 °C under identical experimental conditions (Figure 3.5A).

Then, the treated cells were seeded and incubated for 48 h. Cell viability measurements revealed that more than ~90% of cancer cell death was achieved with ZnMn-IONCs mediated magnetic hyperthermia, while treatment mediated by IONCs reduce the cell viability only by ~40% under the same experimental conditions (Figure 3.5B).

3.4.2 *In vivo* evaluation of ZnMn-IONCs

To investigate the feasibility of ZnMn-IONCs to accumulate into cancer tumors, the SiNc-loaded ZnMn-IONCs were injected intravenously into nude mice bearing subcutaneous xenografts of DU145 prostate cancer cells. At ~10 min post-injection, the accumulation of ZnMn-IONCs was detected in the tumor. The strongest fluorescence intensity was detected at ~10 h and gradually decreased over 24 h after injection (Figure 3.6A,C). The *ex vivo* images confirmed that the accumulation of ZnMn-IONCs was higher in tumor compared to major organs after 18 h of intravenous injection (Figure 3.6B). Owing to the enhanced permeability and retention (EPR) effect, the intravenously injected ZnMn-IONCs accumulated efficiently into the tumor due to long blood circulation time and leaky tumor vasculature.^{29, 30}

The heating effect of nanoclusters in mice bearing the subcutaneous xenograft of prostate cancer cells was further investigated. Mice were injected intravenously with nanoclusters at a dose of 10 mg_{Fe}/kg once per week for 4 weeks and were exposed to AMF ($f = 420$ kHz, $H = 26.9$ kA/m) at 18 h post-injection. The intratumoral temperature was monitored using a fiber optic probe inserted into the tumor. The *in vivo* results showed that the ZnMn-IONCs increased the

intratumoral temperature to 42 °C upon exposure to AMF (Figure 3.7A), while mice treated with IONCs reached only 38.5 °C at the same condition (Figure 3.7A). For untreated mice, the intratumoral temperature was slightly increased by 1.5 °C due to the generation of eddy currents.³¹

Based on the *in vivo* studies, the mice treated with ZnMn-IONCs-mediated magnetic hyperthermia demonstrated significant inhibition in tumor growth compared to the mice treated with IONCs-mediated hyperthermia (Figure 3.7B). The tumor volume of mice treated with MnZn-IONCs-mediated hyperthermia was ~2 times smaller in comparison to mice exposed to IONCs-mediated hyperthermia (Figure 3.7B). Of note, there was no effect on tumor growth for mice exposed to AMF only.

The mice were monitored for 2 weeks following treatment for toxicity evaluation. There were no signs of toxicity (*e.g.*, appearance, death) or weight loss in the mice treated with ZnMn-IONCs mediated hyperthermia (Figure 3.7C).

3.5 CONCLUSION

In summary, we have successfully synthesized zinc and manganese-doped iron oxide nanoparticles that have higher saturation magnetization and SAR compare to iron oxide nanoparticles synthesized under the same conditions with similar parameters. ZnMn-IONPs were loaded into PEG-PCL to obtain water soluble nanoclusters. ZnMn-IONCs showed good biocompatibility and no observed toxicity in mice when injected intravenously. After 18 h following intravenous injection, ZnMn-IONCs accumulated in the tumor via passive targeting and were capable of achieving the required intratumoral temperature to destroy cancer cells upon exposure to AMF. The low dosage of ZnMn-IONCs combined with applied AMF efficiently inhibited tumor growth during 4 cycles of treatment in comparison to IONCs under the same

experimental conditions. Further studies are planned to confirm long-time safety of ZnMn-IONCs and investigate the therapeutic outcome of magnetic hyperthermia in combination with other anti-cancer therapies.

3.6 ACKNOWLEDGMENTS

This research was supported by NIH/NBIB (1R15EB020351-01A1), the College of Pharmacy at Oregon State University (OSU), Najran University, and National Center for Advancing Translational Sciences of NIH (KL2 TR002370). The funding sources had no involvement in the collection, analysis, and interpretation of the data or in the decision to submit the article for publication.

3.7 REFERENCES

1. Deatsch, A. E.; Evans, B. A., Heating efficiency in magnetic nanoparticle hyperthermia. *Journal of Magnetism and Magnetic Materials* **2014**, 354, 163-172.
2. Kumar, C. S.; Mohammad, F., Magnetic nanomaterials for hyperthermia-based therapy and controlled drug delivery. *Advanced drug delivery reviews* **2011**, 63 (9), 789-808.
3. Luo, S.; Wang, L.; Ding, W.; Wang, H.; Zhou, J.; Jin, H.; Su, S.; Ouyang, W., Clinical trials of magnetic induction hyperthermia for treatment of tumours. *OA Cancer* **2014**, 2 (1), 2.
4. Torres-Lugo, M.; Rinaldi, C., Thermal potentiation of chemotherapy by magnetic nanoparticles. *Nanomedicine : nanotechnology, biology, and medicine* **2013**, 8 (10), 1689-1707.
5. Dönmez, C. E. D.; Çiğdem, E.; Manna, P. K., Comparative Heating Efficiency of Cobalt-, Manganese-, and Nickel-Ferrite Nanoparticles for a Hyperthermia Agent in Biomedicines. *ACS APPLIED MATERIALS & INTERFACES* **2019**, 11 (7), 6858-6866.
6. Hayashi, K.; Nakamura, M.; Sakamoto, W.; Yogo, T.; Miki, H.; Ozaki, S.; Abe, M.; Matsumoto, T.; Ishimura, K., Superparamagnetic nanoparticle clusters for cancer theranostics combining magnetic resonance imaging and hyperthermia treatment. *Theranostics* **2013**, 3 (6), 366.
7. Xie, J.; Yan, C.; Yan, Y.; Chen, L.; Song, L.; Zang, F.; An, Y.; Teng, G.; Gu, N.; Zhang, Y., Multi-modal Mn–Zn ferrite nanocrystals for magnetically-induced cancer targeted hyperthermia: a comparison of passive and active targeting effects. *Nanoscale* **2016**, 8 (38), 16902-16915.

8. Guardia, P.; Labarta, A.; Batlle, X., Tuning the size, the shape, and the magnetic properties of iron oxide nanoparticles. *The Journal of Physical Chemistry C* **2010**, *115* (2), 390-396.
9. Jang, J. t.; Nah, H.; Lee, J. H.; Moon, S. H.; Kim, M. G.; Cheon, J., Critical enhancements of MRI contrast and hyperthermic effects by dopant-controlled magnetic nanoparticles. *Angewandte Chemie* **2009**, *121* (7), 1260-1264.
10. Raland, R.; Borah, J., Efficacy of heat generation in CTAB coated Mn doped ZnFe₂O₄ nanoparticles for magnetic hyperthermia. *Journal of Physics D: Applied Physics* **2016**, *50* (3), 035001.
11. Bauer, L. M.; Situ, S. F.; Griswold, M. A.; Samia, A. C. S., High-performance iron oxide nanoparticles for magnetic particle imaging-guided hyperthermia (hMPI). *Nanoscale* **2016**, *8* (24), 12162-12169.
12. Jang, J. t.; Lee, J.; Seon, J.; Ju, E.; Kim, M.; Kim, Y. I.; Kim, M. G.; Takemura, Y.; Arbab, A. S.; Kang, K. W., Giant Magnetic Heat Induction of Magnesium-Doped γ -Fe₂O₃ Superparamagnetic Nanoparticles for Completely Killing Tumors. *Advanced Materials* **2018**, *30* (6), 1704362.
13. Albarqi, H. A.; Wong, L. H.; Schumann, C.; Sabei, F. Y.; Korzun, T.; Li, X.; Hansen, M. N.; Dhagat, P.; Moses, A. S.; Taratula, O., Biocompatible Nanoclusters with High Heating Efficiency for Systemically Delivered Magnetic Hyperthermia. *ACS nano* **2019**.
14. Tvermoes, B. E.; Unice, K. M.; Paustenbach, D. J.; Finley, B. L.; Otani, J. M.; Galbraith, D. A., Effects and blood concentrations of cobalt after ingestion of 1 mg/d by human volunteers for 90 d. *Am J Clin Nutr* **2014**, *99* (3), 632-46.

15. Jeun, M.; Moon, S. J.; Kobayashi, H.; Shin, H. Y.; Tomitaka, A.; Kim, Y. J.; Takemura, Y.; Paek, S. H.; Park, K. H.; Chung, K.-W., Effects of Mn concentration on the ac magnetically induced heating characteristics of superparamagnetic $\text{Mn}_x\text{Zn}_{1-x}\text{Fe}_2\text{O}_4$ nanoparticles for hyperthermia. *Applied physics letters* **2010**, 96 (20), 202511.
16. Sun, S.; Zeng, H.; Robinson, D. B.; Raoux, S.; Rice, P. M.; Wang, S. X.; Li, G., Monodisperse mFe_2O_4 (m= Fe, Co, Mn) nanoparticles. *Journal of the American Chemical Society* **2004**, 126 (1), 273-279.
17. Sun, S.; Zeng, H., Size-controlled synthesis of magnetite nanoparticles. *Journal of the American Chemical Society* **2002**, 124 (28), 8204-8205.
18. Taratula, O.; Dani, R. K.; Schumann, C.; Xu, H.; Wang, A.; Song, H.; Dhagat, P.; Taratula, O., Multifunctional nanomedicine platform for concurrent delivery of chemotherapeutic drugs and mild hyperthermia to ovarian cancer cells. *International journal of pharmaceutics* **2013**, 458 (1), 169-180.
19. Duong, T.; Li, X.; Yang, B.; Schumann, C.; Alabrqi, H. A.; Taratula, O.; Taratula, O., Phototheranostic Nanoplatfrom Based on a Single Cyanine Dye for Image-Guided Combinatorial Phototherapy *Nanomedicine : nanotechnology, biology, and medicine* **2016**, [Epub ahead of print]
20. Li, X.; Schumann, C.; Albarqi, H. A.; Lee, C. J.; Alani, A. W.; Bracha, S.; Milovancev, M.; Taratula, O.; Taratula, O., A tumor-activatable theranostic nanomedicine platform for NIR fluorescence-guided surgery and combinatorial phototherapy. *Theranostics* **2018**, 8 (3), 767.
21. Taratula, O.; Schumann, C.; Naleway, M. A.; Pang, A. J.; Chon, K. J.; Taratula, O., A multifunctional theranostic platform based on phthalocyanine-loaded dendrimer for image-

guided drug delivery and photodynamic therapy. *Molecular pharmaceutics* **2013**, *10* (10), 3946-3958.

22. Taratula, O.; Schumann, C.; Duong, T.; Taylor, K. L., Dendrimer-encapsulated naphthalocyanine as a single agent-based theranostic nanoplatform for near-infrared fluorescence imaging and combinatorial anticancer phototherapy. *Nanoscale* **2015**, *7* (9), 3888-902.

23. Huang, H. S.; Hainfeld, J. F., Intravenous magnetic nanoparticle cancer hyperthermia. *International journal of nanomedicine* **2013**, *8*, 2521-32.

24. Maier-Hauff, K.; Ulrich, F.; Nestler, D.; Niehoff, H.; Wust, P.; Thiesen, B.; Orawa, H.; Budach, V.; Jordan, A., Efficacy and safety of intratumoral thermotherapy using magnetic iron-oxide nanoparticles combined with external beam radiotherapy on patients with recurrent glioblastoma multiforme. *Journal of neuro-oncology* **2011**, *103* (2), 317-324.

25. Sharifi, I.; Shokrollahi, H.; Amiri, S., Ferrite-based magnetic nanofluids used in hyperthermia applications. *Journal of magnetism and magnetic materials* **2012**, *324* (6), 903-915.

26. Rao, K.; Choudary, G.; Rao, K.; Sujatha, C., Structural and magnetic properties of ultrafine CoFe₂O₄ nanoparticles. *Procedia Materials Science* **2015**, *10*, 19-27.

27. Yelenich, O.; Solopan, S.; Kolodiazhnyi, T.; Tykhonenko, Y.; Tovstolytkin, A.; Belous, A., Magnetic Properties and AC Losses in AFe₂O₄ (A= Mn, Co, Ni, Zn) Nanoparticles Synthesized from Nonaqueous Solution. *Journal of Chemistry* **2015**, *2015*.

28. Lee, J. H.; Jang, J. T.; Choi, J. S.; Moon, S. H.; Noh, S. H.; Kim, J. W.; Kim, J. G.; Kim, I. S.; Park, K. I.; Cheon, J., Exchange-coupled magnetic nanoparticles for efficient heat induction. *Nature nanotechnology* **2011**, *6* (7), 418-22.

29. Maruyama, K., Intracellular targeting delivery of liposomal drugs to solid tumors based on EPR effects. *Advanced drug delivery reviews* **2011**, 63 (3), 161-169.
30. Duan, X.; Li, Y., Physicochemical characteristics of nanoparticles affect circulation, biodistribution, cellular internalization, and trafficking. *Small (Weinheim an der Bergstrasse, Germany)* **2013**, 9 (9-10), 1521-1532.
31. Stigliano, R. V.; Shubitidze, F.; Petryk, J. D.; Shoshiashvili, L.; Petryk, A. A.; Hoopes, P. J., Mitigation of eddy current heating during magnetic nanoparticle hyperthermia therapy. *International Journal of Hyperthermia* **2016**, 32 (7), 735-748.

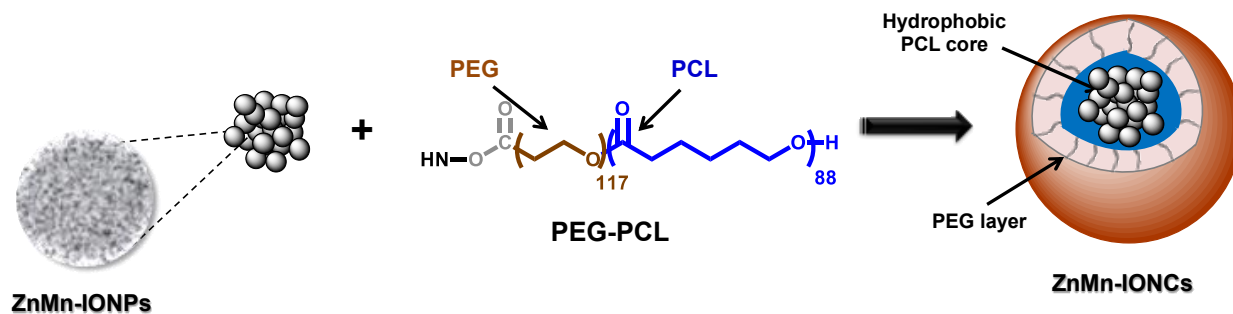


Figure 3.1: Schematic illustration of the nanoclusters for magnetic hyperthermia.

The nanoclusters are prepared by encapsulation of zinc and manganese-doped iron oxide nanoparticles (ZnMn-IONP) into the hydrophobic core of PEG-PCL-based nanocarriers.

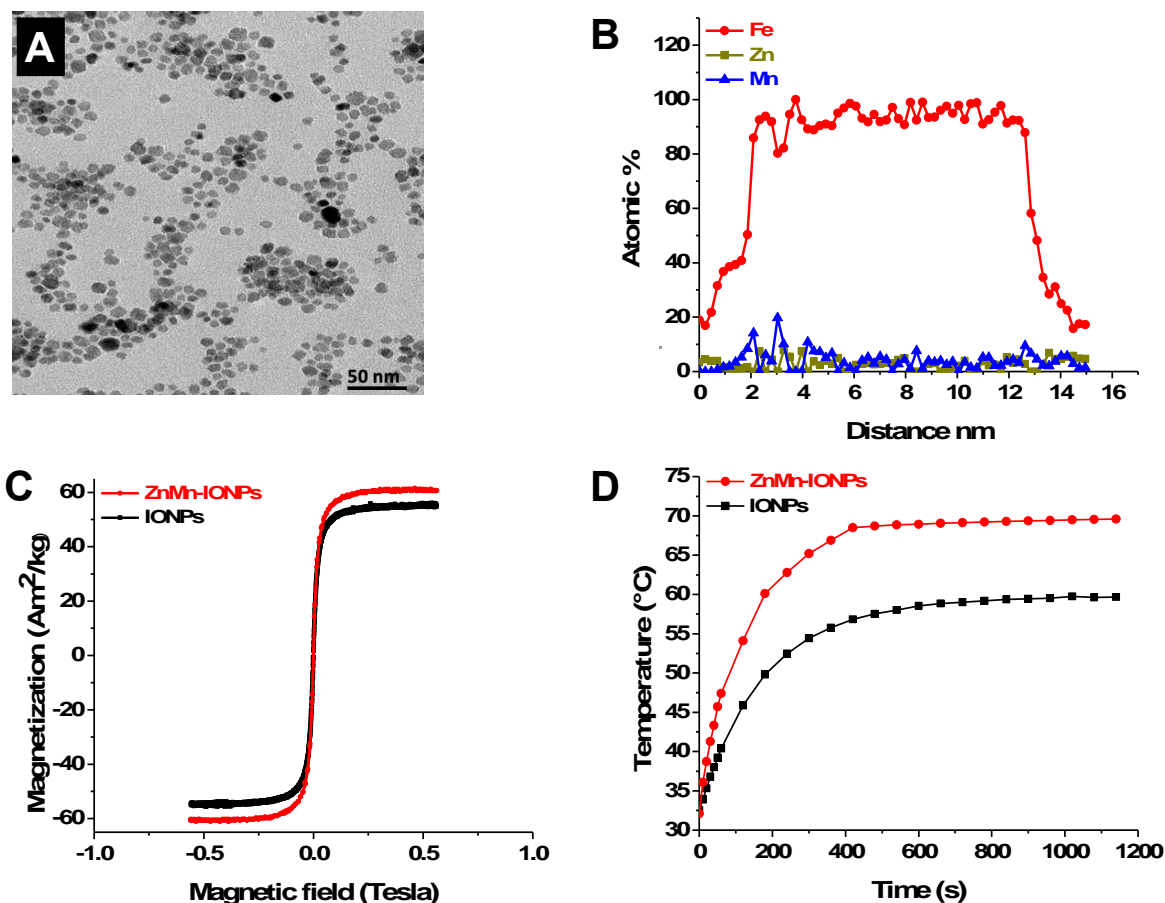


Figure 3.2: Characterization of ZnMn-IONP and IONP.

(A) Representative TEM image of zinc and manganese-doped iron oxide nanoparticles (ZnMn-IONP). (B) Zn, Fe, and Mn EDX line scanning profile of a single ZnMn-IONP confirms that Zn and Mn are distributed throughout the nanoparticle. (C) Magnetization curves of ZnMn-IONP (red) and IONP (black) at room temperature. The magnetization values were normalized by the total weight of nanoparticles. (D) Heating profiles of ZnMn-IONP and IONP dispersed in THF ($1 \text{ mg}_{\text{Fe}}/\text{mL}$) and subjected to AMF (420 kHz, 26.9 kA/m).

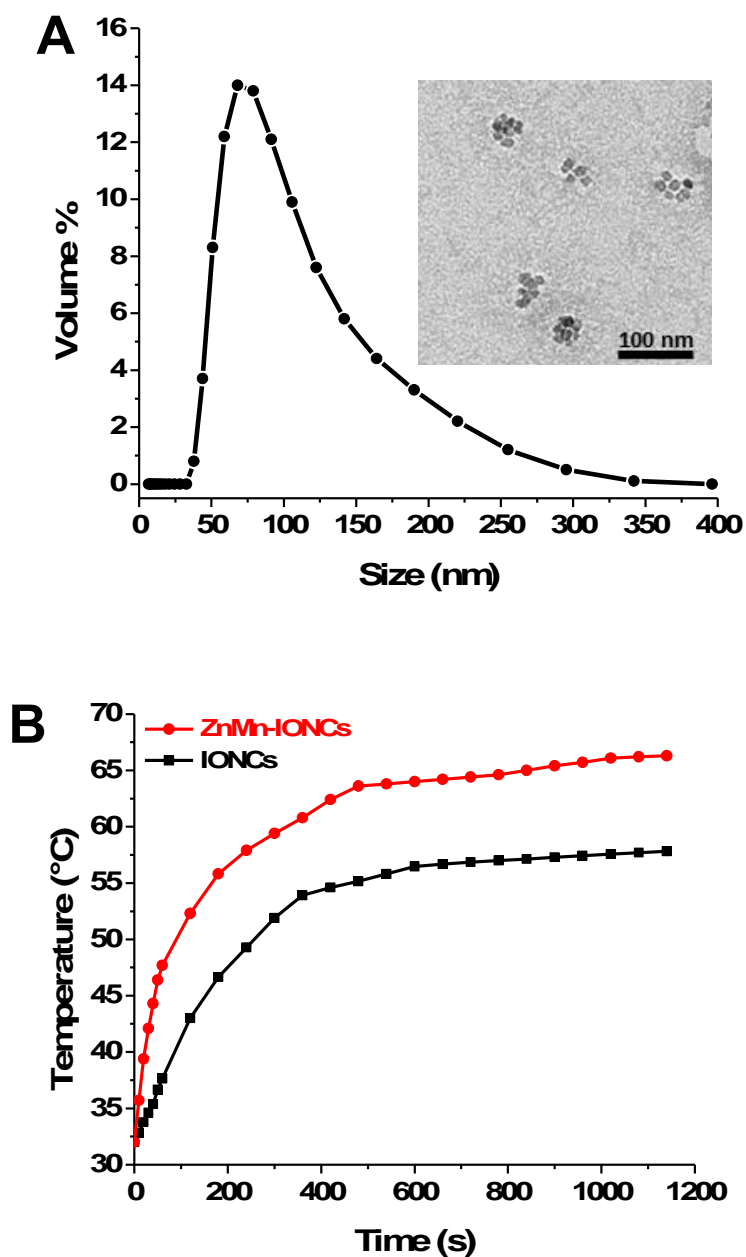


Figure 3.3: Characterization of ZnMn-IONCs and IONCs.

(A) Size distribution of ZnMn-IONCs tested by DLS at room temperature. Inset: TEM image of ZnMn-IONCs. (B) Heating profiles of ZnMn-IONCs and IONCs in water (1 mg Fe /mL) subjected to AMF (420 kHz, 26.9 kA/m).

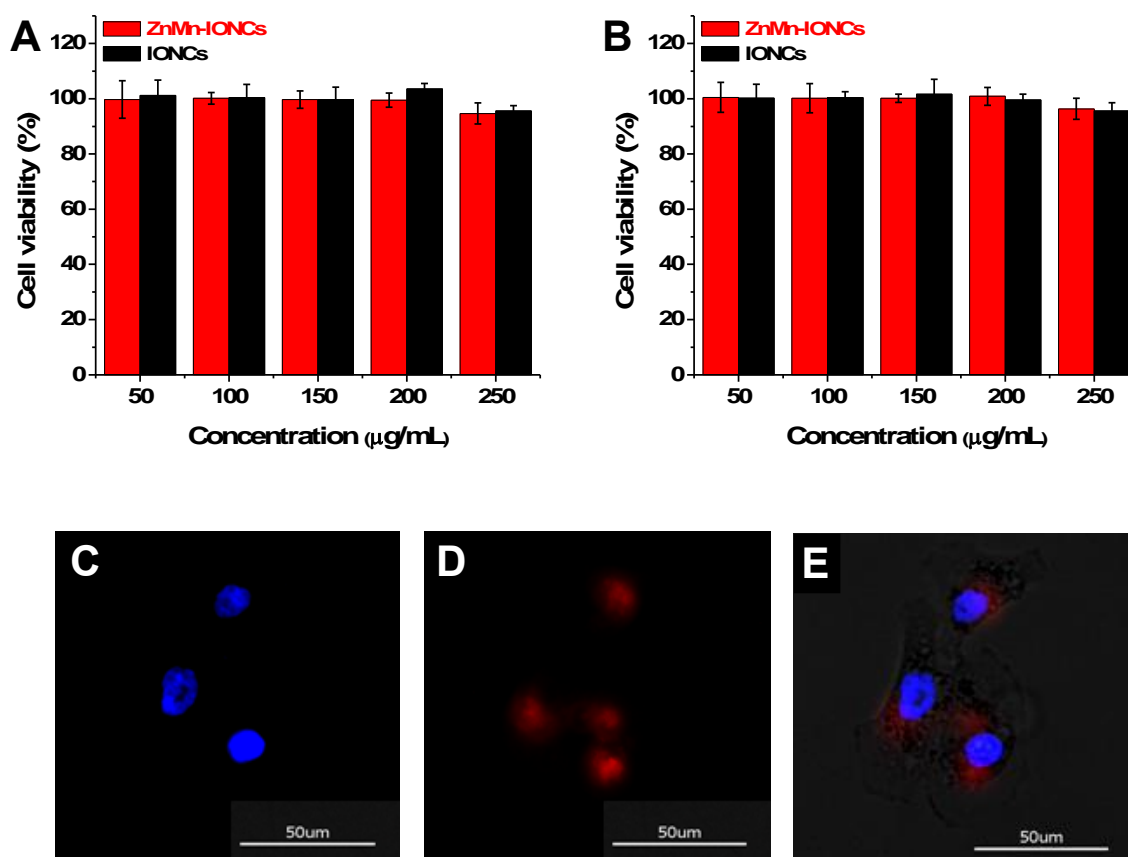


Figure 3.4: Cell viability and internalization of nanocluster.

(A) Viability of DU145 cells incubated for 24 h with different concentrations of ZnMn-IONCs and IONCs (50–250 $\mu\text{g Fe/mL}$). $*p < 0.05$ when compared with non-treated cells. (B) Viability of human embryonic kidney cells (HEK-293) incubated for 24 h with different concentrations of ZnMn-IONCs and IONCs (50–250 $\mu\text{g Fe/mL}$). Fluorescence microscopy images of DU145 cells demonstrating intracellular accumulation SiNc-ZnMn-IONCs (C) DAPI staining, (D) SiNC-ZnMn-IONCs, and (E) overlay.

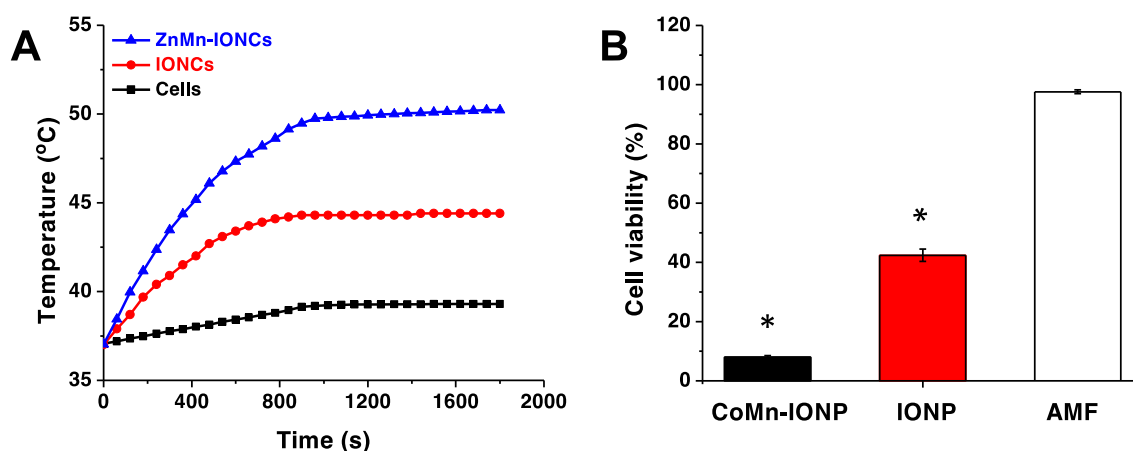


Figure 3.5: Heating profile and cell viability of ZnMn-IONCs and IONCs.

(A) Representative heating profiles of DU145 cells incubated with media only (cells only), ZnMn-IONCs and IONCs (50 $\mu\text{g Fe/mL}$) for 24 h, and subjected to AMF (420 kHz, 26.9 kA/m). **(B)** The viability of DU145 cells incubated with ZnMn-IONCs, IONCs (50 $\mu\text{g Fe/mL}$), and medium (AMF) for 24 h and exposed to AMF (420 kHz, 26.9 kA/m) for 30 min. * $p < 0.05$ when compared with untreated cells.

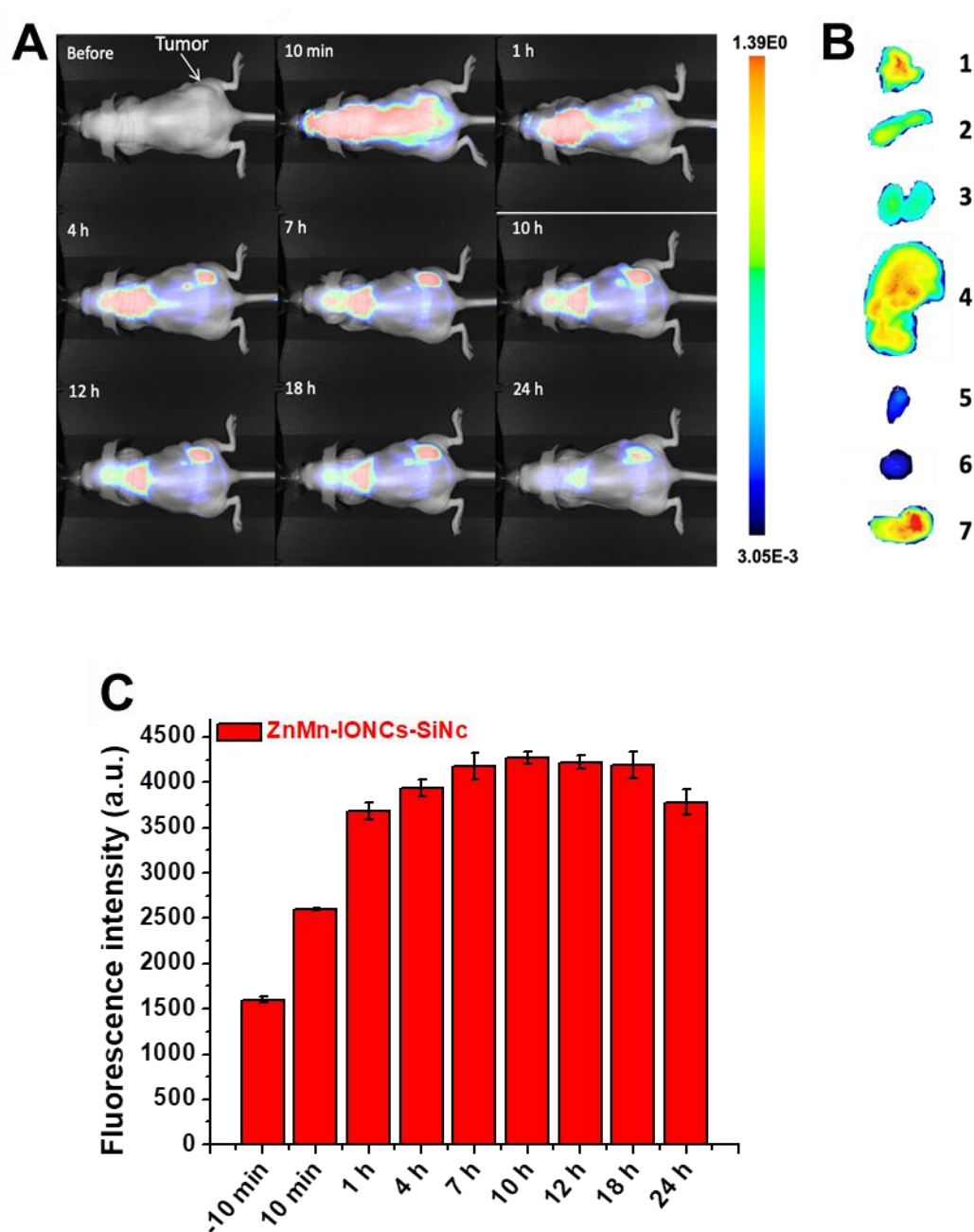


Figure 3.6: In vivo biodistribution of ZnMn-IONCs.

(A) Representative NIR fluorescence images of a live anesthetized mouse with DU145 subcutaneous tumor at various time points after *i.v.* injection of ZnMn-IONCs loaded with a hydrophobic NIR dye (silicon 2,3-naphthalocyanine bis(trihexylsilyloxy), SiNc). (B) ex vivo imaging of SiNc-ZnMn-IONCs in 1- lung, 2-spleen, 3-kidney, 4-liver, 5-heart, 6-brain, and 7-tumor. (C) The NIR fluorescence intensity measured in the tumor as a function of time after intravenous injection of SiNc-ZnMn-IONCs in a mouse bearing DU145 tumor.

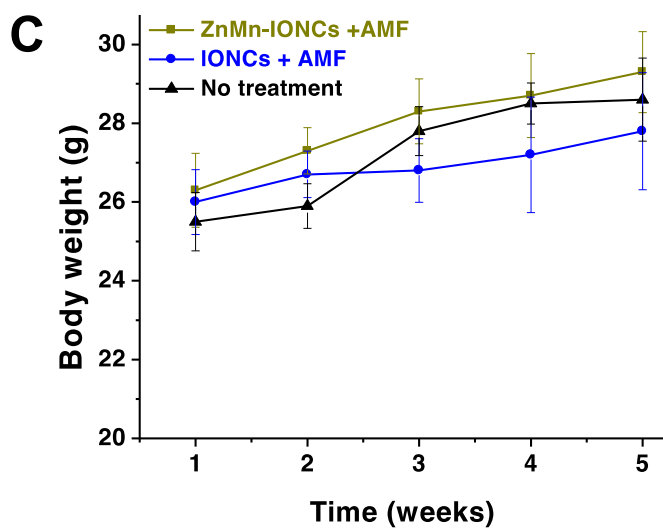
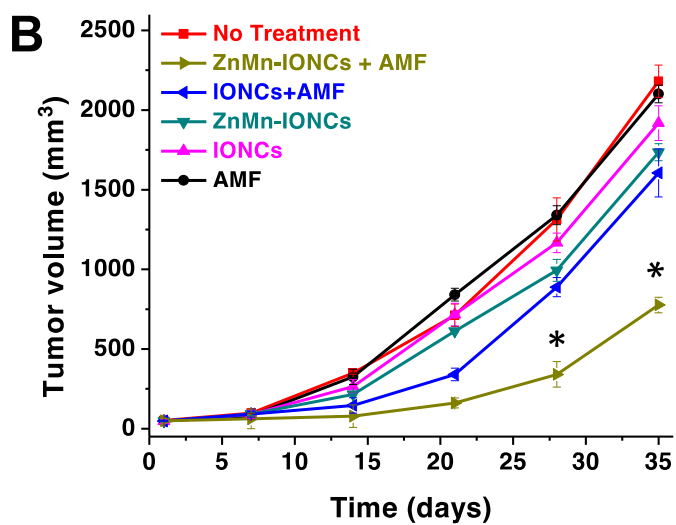
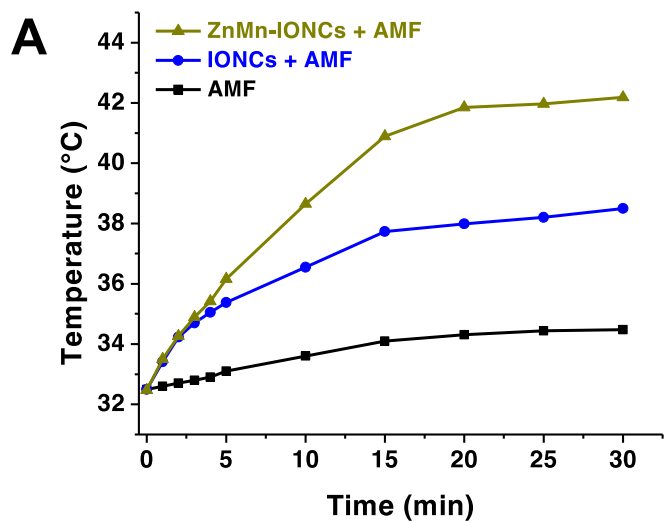


Figure 3.7: Intratumoral heating profile, tumor volume, and body weight.

(A) Representative intratumoral temperature profiles during AMF (420 kHz, 26.9 kA/m) exposure of mice injected with a single dose of 5% dextrose (AMF), ZnMn-IONCs (10 mg Fe/kg) and IONCs (10 mg Fe/kg). once a week for 4 weeks. (B) Tumor growth profiles of mice with DU145 xenografts after 4 cycles of the following treatments: (i) no treatment; (ii) ZnMn-IONCs + AMF, mice injected with ZnMn-IONCs (10 g Fe/kg) and exposed to AMF for 30 min; (iii) IONCs + AMF, mice injected i.v. with IONCs (10 g Fe/kg) and exposed to AMF for 30 min; (iv) ZnMn-IONCs, mice injected i.v. with ZnMn-IONCs (10 g Fe/kg); (v) IONCs, mice injected with IONCs (10 g Fe/kg); and (vi) AMF, mice injected with 5% dextrose and exposed to AMF. $*p < 0.05$ when compared with non-treated animals. (C) Changes in body weights of untreated mice and mice treated with 4 cycles of ZnMn-IONCs -mediated hyperthermia.

CHAPTER 4

GENERAL CONCLUSIONS

The use of iron oxide nanoparticles for cancer hyperthermia has tremendously increased in the last two decades due to their superparamagnetic properties, low toxicity, and biocompatibility . Their superparamagnetic properties have been favorable in biomedical application because IONPs do not retain magnetic properties when the alternating magnetic field is removed. However, their relatively low magnetic heating ability and limitation only to current intratumoral delivery are the main challenges in current clinical hyperthermia. Herein, we have successfully developed biocompatible magnetic nanoclusters that could potentially be delivered to small and heterogeneous cancer tumors. The IONPs were doped with different ratios of metals to tune their magnetic properties and enhance their heating efficacy. These optimized nanoclusters have desired magnetization properties, size, composition, and non-toxicity. The developed nanoclusters were stable in biological fluid and efficiently accumulated in the tumor via passive targeting. After remote activation with an AMF, the developed magnetic nanoclusters elevated the intratumoral temperature over 42°C after a single intravenous injection and inhibit the tumor growth when compared to IONPs

Studies in Chapter 2 demonstrated that we synthesized hexagon-shaped cobalt and manganese-doped iron oxide nanoparticles encapsulated within PEG-PCL polymeric nanocarriers that can inhibit the growth of ovarian cancer *in vitro* and *in vivo* upon exposure to AMF. Incorporating Co and Mn into IONPs maximized their magnetic properties and SAR. Moreover, previous studies reported that the non-spherical magnetic nanoparticles have better heating efficiency compared to spherical magnetic nanoparticles, and that was confirmed in our study. The SAR of CoMn-IONPs is ~ 3.2 times higher than conventional IONPS. CoMn-IONPs showed an increase in temperature up to 56 °C and resulted in ~ 99% cancer cell death *in vitro*. For *in vivo* results, CoMn-IONPs were able to suppress the tumor volume by five times in comparison with IONPs

prepared with the same technology. The tumor growth was inhibited in mice without observed toxicity.

Cobalt is considered to play an essential role to tune the magnetic anisotropy of CoMn-IONPs that has an influence on the magnetic heating efficiency. Despite its high magnetic properties and no observed toxicity *in vivo*, there is a concern about cobalt toxicity. Therefore, we also designed and synthesized a zinc and manganese-doped iron oxide nanoparticle (ZnMn-IONPs) that improves saturation magnetization and heating efficiency in comparison with IONPs. Zinc metal is safe and biocompatible, and Zn ferrite has higher saturation magnetization compared to other ferrites. ZnMn-IONPs were encapsulated efficiently into PEG-PCL to make biocompatible, water-soluble nanoclusters (ZnMn-IONCs). ZnMn-IONCs performed better as a magnetic hyperthermia agent, possess a higher saturation magnetization, and display a two-fold higher SAR value in comparison to IONPs. ZnMn-IONCs mediated hyperthermia *in vivo* resulted in inhibition of the growth of prostate cancer tumor.

Despite the fact that pre-clinical studies on nanoparticle-mediated magnetic hyperthermia present challenges in achieving the required intratumoral temperature after systemic administration, our results indicate the possibility to optimize the magnetic nanoparticle structure for effective systemic delivery with improved heating efficiency. Thus, the developed nanoclusters have a promising therapeutic potential in the treatment of cancer.